


Title	Characterization of GaN-based light-emitting diodes
Author(s)	Antuna-Presa, Silvino Jose
Publication date	2016
Original citation	Antuna-Presa, S. J. 2016. TitCharacterization of GaN-based light-emitting diodes. PhD Thesis, University College Cork.
Type of publication	Doctoral thesis
Rights	© 2016, Silvino Jose Antuna-Presa. http://creativecommons.org/licenses/by-nc-nd/3.0/ 
Embargo information	No embargo required
Item downloaded from	http://hdl.handle.net/10468/5418

Downloaded on 2018-08-23T19:20:35Z



UCC

University College Cork, Ireland
Coláiste na hOllscoile Corcaigh

Ollscoil na héireann

NATIONAL UNIVERSITY OF IRELAND



Characterization of GaN-based light-emitting diodes

A thesis presented to the

National University of Ireland, Cork

For the degree of

Doctor of Philosophy

By

Silvino José Antuña Presa

Supervised by Pleun P. Maaskant and Brian Corbett

Tyndall National Institute

University College Cork

August 2016

Table of Contents:

Declaration	iv
Abstract	v
Acknowledgements	vi
Publications	vii
Chapter 1 - Introduction	1
1.1 Light-emitting diodes	1
1.2 Brief history of LEDs.....	2
1.3 White sources using GaN LEDs.....	5
1.4 Summary of the thesis.....	6
Chapter 2 - Introduction to the Gallium Nitride system	8
2.1 Characteristics and advantages of GaN-based LEDs	8
2.2 Crystal structure of GaN.	10
2.3 Growth techniques of GaN thin films	15
2.4 Layer structure of the wafers used in this thesis.....	17
Chapter 3: Structure and fabrication of LED devices	19
3.1 Design of LED devices	19
3.2 Fabrication of LEDs.....	23
3.2.1 Optical lithography	23
3.2.2 Ohmic contacts on GaN	24
3.2.3 Etching techniques.....	29
3.3 Devices fabricated for this work.....	31
Chapter 4 - Electro-optical methods for the characterization of GaN-based LEDs.	33
4.1 Electrical excitation and current-voltage (I-V) characteristics.....	33
4.2 Ideality factors and estimation of current components	38
4.3 Capacitance-Voltage (C-V) measurements	41
4.3.1 Depletion capacitance	41
4.3.2 Diffusion capacitance and negative capacitance.....	44
4.4 Optical resonant photoluminescence.....	46
4.4.1 Fluorescence microscopy.....	46
4.4.2 Bias dependence photoluminescence	48
4.5 Photovoltaic effects on LEDs	50

Chapter 5 – Combined electrical and resonant optical excitation	
characterization of MQW GaN-based LEDs	56
5.1 Fluorescence microscopy: observation of spatial variations and the effect of metal contacts.....	58
5.2 Current density – voltage and piezoelectric fields.....	62
5.3 Analysis of ideality factors	72
5.4 Estimation of the doping profile from capacitance – voltage (C-V) measurements.....	85
5.5 – Estimation of the internal quantum efficiency of GaN LEDs using light-current-voltage measurements.	89
5.5.1 Theoretical background.....	89
5.5.2 Estimation of quantum efficiency and extraction efficiency	95
5.6 – Summary of all presented results	100
Chapter 6 - Conclusions and recommendations for future work.....	106
Bibliography	109
Appendix A: Python code for the estimation of internal quantum efficiencies.....	120

Declaration

I hereby declare that this is entirely my own work and it has not been submitted as an exercise for the award of a degree at this or any other University. I agree that the Library may lend or copy this dissertation on request

Silvino José Antuña Presa

August 2016

Abstract

Maximizing the performance of light-emitting diodes (LEDs) is essential for the widespread uptake of solid-state lighting. To contribute towards this goal, this thesis focuses on the electrical and optical characterization of InGaN/GaN-based multi quantum well LEDs.

In this work a wide range of characterization methodologies are introduced. A new development is the study of the emission spectra under resonant optical pumping and varying electrical bias. This has proven to be useful to obtain insights into the carrier dynamics and is used here to investigate LED samples containing different numbers of quantum wells (QWs) with different thicknesses for the barriers. Despite having only small structural differences, these samples have shown strong differences in their performance, which are attributed to a stronger piezoelectric field in the QWs in the sample with thinner barriers. Fluorescence microscopy with selective excitation of the QWs also allows the study of the spatially dependent luminescent properties of LEDs. In this case ohmic contacts create an equipotential surface and influence the collective emission. Strong carrier escape is observed in photovoltaic mode under both open and short circuit conditions. To help identify the underlying recombination mechanisms, different voltage ideality factors are extracted and compared with each other.

This thesis shows that the use of photovoltaic measurements together with bias-dependent spectrally resolved luminescence is a powerful tool to investigate GaN LEDs. The methodologies presented here provide experimental tools to better understand carrier recombination processes in different LED samples. These methods can be extended to samples grown on different crystallographic orientations or to study the effects of additional layers in novel LED structures.

Acknowledgements

I would like to express my gratitude to my supervisors Pleun P. Maaskant and Brian Corbett for giving me the opportunity to research for my PhD in Tyndall National Institute and also for their supervision, guidance and help during these years of research. I would like to thank as well my advisor Peter J. Parbrook for his suggestions and continuous advice during my research.

I cannot forget about all the excellent researchers that helped me since the moment I arrived at Tyndall National Institute. I express my warm thanks to Mahbub Akhter, Farzan Gity, Grzegorz Kozlowski, Duc V. Dinh, Donagh O'Mahony, James O'Callaghan, Carmel Murphy, Dan O'Connell, and all the members of the GaN team at Tyndall for their help and support during my PhD.

This dissertation would not have been possible without funding from the European Communities 7th Framework Programme and the Irish Photonics Integration Centre.

Finally, I would like to thank my wife Beatriz Ruiz Martín for her support all these years, also to my sister, my parents and the rest of my family along with all my friends for all the help and support they have provided since I moved to Cork.

Publications

Publications in peer-reviewed journals:

1. S. Presa, P. P. Maaskant, M. J. Kappers and B. Corbett, "*Fluorescence microscopy investigation of InGaN-based LEDs*". IET Optoelectronics, 10, 39 (2016)
2. S. Presa, P. P. Maaskant, M. J. Kappers, C. J. Humphreys, and B. Corbett, "*Combined electrical and resonant optical excitation characterization of multi-quantum well InGaN-based light-emitting diodes*". AIP Advances, 6, 075108 (2016)
3. D. V. Dinh, M. Akther, S. Presa, G. Kozlowski, D. O'Mahony, P. P. Maaskant, F. Brunner, M. Caliebe, M. Weyers, F. Scholz, B. Corbett and P. J. Parbrook, "*Semipolar (11-22) InGaN light-emitting diodes grown on chemically-mechanically polished GaN templates*" Phys. Stat. solidi (a), 212, 2196 (2015)
4. D. V. Dinh, S. Presa, P. P. Maaskant, B. Corbett, and P. J. Parbrook, "*Exciton localization in polar and semipolar (11-22) InGaN/GaN multiple quantum wells*" Semicond. Sci. Technol. 31, 085006 (2016)
5. Z. H. Quan, D. V. Dinh, S. Presa, B. Roycroft, A. Foley, M. Akhter, D. O'Mahoney, P. P. Maaskant, M. Caliebe, F. Scholz, P. J. Parbrook, and B. Corbett, "*High bandwidth freestanding semipolar (11-22) InGaN light emitting diodes*" IEEE Photonics (2016) –accepted.

Conference presentations:

1. Characterization of long wavelength semipolar InGaN light-emitting diodes. S. Presa, M. Akhter, D. V. Dinh, D. O'Mahony, P. P. Maaskant, P. J. Parbrook, and B. Corbett. Photonics Ireland 2015 (poster)
2. Study of recombination dynamics in InGaN/GaN light-emitting diodes using fluorescence microscopy. S. Presa, P. P. Maaskant, M. J. Kappers, C. J. Humphreys and B. Corbett. SIOE 2015 (oral)

3. Carrier recombination in InGaN/GaN light-emitting diodes. S. Presa, P. P. Maaskant and B. Corbett. IoP spring meeting 2015 (poster)
4. Fluorescence microscopy on SQW green light emitting diodes. S. Presa, P. P. Maaskant, M. J. Kappers, C. J. Humphreys and B. Corbett. UKNC winter meeting 2015 (poster)
5. Characterization of InGaN/GaN light-emitting diodes using fluorescence microscopy. S. Presa, G. Kozlowski, P. P. Maaskant, P. J. Parbrook, M. J. Kappers, C. J. Humphreys and B. Corbett. SIOE 2014 (oral)
6. Measurement of the quantum efficiency on InGaN-based LED material. S. Presa, G. Kozlowski, P. P. Maaskant, P. J. Parbrook, M. J. Kappers, C. J. Humphreys and B. Corbett. Photonics Ireland 2013 (poster)
7. Light emission from Blue LED structures at very low bias voltage. S. Presa, G. Kozlowski, P. P. Maaskant, M. J. Kappers, C. J. Humphreys and B. Corbett. UKNC summer meeting 2013 (poster)

Chapter 1 – Introduction

The focus of this thesis is the combined electrical and resonant optical characterization of multiple quantum well (MQW) gallium nitride (GaN) light-emitting diodes (LEDs). The main reason for this interest in GaN LEDs is the demand for visible emitters for applications such as automotive lighting, indoor lighting, traffic signals and many others. Currently there are only a few semiconductor material systems suitable for these applications due to the high bandgap required for blue (photon energy >2.5 eV) and UV emission (photon energy >3.25 eV). Furthermore, among the available semiconductors, only III-nitrides are a practical solution for highly efficient devices at these wavelengths.

In this introductory chapter there is a brief historical background of the development of the first electroluminescent devices which later became actual LEDs. The focus here is on the materials used for emission wavelengths in and close to the visible spectrum. This chapter also establishes briefly the most common problems and challenges faced today to achieve highly efficient LEDs. These challenges related to GaN LEDs will be discussed in more detail in the following chapters.

1.1 Light-emitting diodes

A light - emitting diode or LED is a semiconductor device capable of emitting light by recombination of carriers when an external bias current is applied. Recent achievements in LED efficiency (in terms of lumens per watt) have generated great interest because highly efficient LEDs have potential application not only in the general illumination market but also in optical communications, biomedicine and many other different fields. As a result of this vast range of applications, the optical and electrical characterization of LEDs is relevant.

LEDs consist typically of a semiconductor p - n junction with two electrical contacts: one is for the p -doped semiconductor which is the source of holes and the other for the n -doped semiconductor acting as an electron source. When a forward bias is applied

both types of carrier are driven to the p - n junction where they recombine emitting a photon with the same energy as the bandgap. To improve the efficiency, the p - n junction of LEDs usually consists of a series of quantum wells (QWs) designed to confine the carriers and force them to recombine. A QW is a thin layer of material that confines free carriers (electron and holes in this case) in a 2-dimensional sheet. When the thickness of this QW is very small – typically less than 10 nanometres-, carriers can only have discrete energy values (quantum confinement). In the case of LEDs, QWs are formed using a thin layer of semiconductor embedded between two layers of a wider bandgap semiconductor. Varying the composition of the QW semiconductor material allows a change of bandgap and a corresponding change in emission wavelength.

The generation of the light by recombination of carriers gives us the main advantage of LEDs: in contrast to traditional light sources such as incandescent lamps, LEDs do not use or require heat to generate light and all the electrical energy can theoretically be converted into light. Moreover, any process that generates heat inside these devices improves the non-radiative recombination reducing the overall efficiency of the LED. So not only do LEDs not rely on heat to produce light, heat is even detrimental for these devices in terms of device efficiency and reliability. A deeper analysis of mechanisms that reduce the efficiency of GaN LEDs is presented in chapter 4 of this thesis.

1.2 Brief history of LEDs

The effect of light emission in response to the passing of an electrical current or a strong electric field is called electroluminescence and is the fundamental physical working principle of LEDs. Electroluminescence was discovered by H. J. Round of Marconi Labs in 1907 when he reported yellow electroluminescence from a piece of silicon carbide (SiC, also known as carborundum) [1]. These devices were Schottky diodes, rather than p - n diodes. Under strong forward bias conditions in these Schottky diodes, minority carriers are injected by tunnelling from the metal and are able to recombine producing near-bandgap light emission. The mechanism is similar in a p - n junction diode, yet the reported

voltages required to turn on these Schottky devices ranged between 10 and 110V, much larger than those found in common LEDs [2].

Round's discovery was initially ignored and more than 20 years had to pass before the first report of an electroluminescent blue emitting device with accidental semiconductor *p-n* junctions. This work was published in 1928 by O.W. Lossew [3] who devoted the succeeding years to examining and describing this phenomenon in great detail. Following this work, G. Destriau came up with the term electroluminescence in 1936 when he discovered light emission from zinc sulfide [4].

The development of the transistor by J. Bardeen, W. Brattain and W. Shockley in 1947 provided a scientific step forward in semiconductor physics and revolutionized the field of electronics [5]. Shockley published "The theory of *p-n* junctions in semiconductors and *p-n* junction transistors" in 1949, providing an explanation for the light emission effect in *p-n* junctions and a background for the study of *p-n* junction devices.

New semiconductor growth techniques and consequent improvement of the quality of semiconductor films resulted in the first blue LED using SiC films with proper *p-n* junctions [6]. The drawback was the low electrical-to-optical power-conversion efficiency reported at this time of around 0.005% [7]. The reason for this low efficiency is that SiC has an indirect bandgap so carriers cannot recombine without exchanging momentum with the crystal lattice. This radiative recombination process involving two carriers and a lattice phonon is very inefficient. III-V materials were postulated by H. Welker in 1953 [8] in the dawn of semiconductor science and technology. Previous studies were done with SiC and II-VI materials because many of these semiconductors occur in nature. III-V materials on the other hand, are manmade and require the careful growth of the material which had only recently become possible. The possibility of bulk growth of GaAs crystal structures allowed for example the demonstration of infrared LEDs and lasers in 1962 by M.I. Nathan et al. [9]. Some years later red LEDs were also demonstrated using GaAs crystals alloyed with GaP [10]. These early devices quickly showed promising electrical and optical properties although the external

quantum efficiency of the alloy was limited to less than 0.03% at that time [11]. Nowadays these materials have been widely researched and the wide commercial availability of high quality GaAs bulk substrates allows for a relatively straightforward epitaxial growth of optoelectronic devices. Modern devices have reported external quantum efficiencies of 61% for red (650nm), 55% for orange-red (610nm) [12], while for the infrared case internal quantum efficiencies of at least 80% have been reported across the full 1.2 - 1.6 μm band [13].

GaN is a wide bandgap (3.41 eV) III-V semiconductor capable of emitting light in violet and blue colours by direct bandgap emission. This material has been known since the first half of the 20th century when a publication by R. Juza and H. Hahn [14] (1938) described how to prepare GaN powder by reacting ammonia with liquid gallium metal at high temperatures. These studies formed the basis for the work of H. P. Maruska and J. J. Tietjen on the growth of GaN single-crystal films three decades later (in 1969) using sapphire as a substrate [15].

During the next decade of the 1970's several groups took an interest in the development of GaN crystals with the strong belief that these crystals could yield the first efficient blue LED. The main problem faced at this time was how to achieve the required *p*-doping of the GaN to form a *p-n* junction. These originally reported GaN thin films were all *n*-type without intentional doping. Zinc was the first element used as an acceptor dopant for GaN but even under heavy Zn concentrations GaN only proved to be insulating [2]. Although not a LED device, these early efforts resulted in the first metal-insulator-semiconductor (MIS) diode demonstrated in 1971 by Pankove et. al. [16]. This device had an emission wavelength of 475nm which makes it the first GaN-based current-injected device capable of emitting light.

The unavailability of *p*-type GaN led to the momentary abandonment of the research in GaN as a material for blue LEDs until 1989 when I. Akasaki et al. demonstrated the first true *p*-type doping and *p*-type conductivity in GaN [17]. They used Mg following previous works from H. P. Maruska, although to achieve *p*-conductivity in this case Mg dopants were activated after the growth of the

material. The first way of activating these dopants was using electron-beam irradiation [17] and later it was demonstrated by Nakamura et al. [18] that the activation could be done by post-growth thermal annealing. Nowadays, thermal annealing is the standard procedure to activate *p*-dopants and achieve *p*-type GaN thin films. Once the possibility of creating a *p-n* homojunction with GaN had become a reality, the interest in the material started to grow again and in 1993 the first viable blue [19] and violet [20] InGaN double-heterostructure LEDs were demonstrated by Nakamura et al. reporting external quantum efficiencies of 0.22% and 0.15%, respectively. Their work also led to the development of the first green GaN LEDs a couple of years later [21]. I. Akasaki, H. Amano and S. Nakamura were awarded the Nobel prize in Physics in 2014 “*for the invention of efficient blue light-emitting diodes which has enabled bright and energy-saving white light sources*” [22].

1.3 White sources using GaN LEDs

Direct bandgap semiconductor materials such as GaN can provide a good alternative to fluorescent lamps and other traditional light sources that have several drawbacks as the amount of heat generated instead of light, or the use of harmful materials such as mercury. The quick rise in lm/W performance in LEDs since the invention of the efficient blue LED draws a lot of attention to this material as a suitable candidate to replace traditional light sources. Furthermore, this trend is expected to continue in the next years.

The main obstacle for GaN LEDs to become the main choice for illumination applications is the lack of highly efficient sources in the wavelength range of 530 to 630nm. This lack of efficient green and yellow emitters is known as the ‘green gap’ [23-25] and this prevents highly efficient white lighting based on separate red-green-blue (RGB) or red-green-blue-yellow (RGBY) emitters. Currently, to obtain white LED light a violet or blue light source is used in combination with yellow and/or red phosphors to convert part of its light output. Despite the fact that this conversion reduces the overall efficiency of the GaN devices, luminous efficiencies of >200 lm/W have been achieved [26]. High colour rendering

indices can be obtained using multi-phosphor systems, yet the desired solution of having three highly efficient sources for blue, green and red is not yet available.

Although the solution of the green gap is beyond the scope of this thesis, this work provides a comprehensive experimental study of the emission spectra and electrical characteristics of InGaN/GaN MQW LED structures that can be applied to the characterization of GaN LEDs of different wavelengths. The main goal of this work is to analyse the real causes of efficiency loss in GaN devices. The application of the techniques described in chapters 4 and 5 gives a better view of the underlying processes that affect the recombination of carriers and help with the identification of non-radiative processes that result in efficiency losses.

1.4 Summary of the thesis

This thesis is devoted to providing a comprehensive method for the electrical and optical characterization of GaN-based LEDs. In contrast to other devices through the history of electrical and electronic engineering, the main research of GaN devices has been carried out in industry laboratories and not in academic institutions. This has resulted in a lack of understanding of some of the properties and underlying mechanisms. The previously mentioned green gap is one example and also the sub-linear increase of the light output with the current density, usually known as 'droop', still remains controversial after a decade of debate and literally thousands of publications [27-29].

This thesis addresses processes that are dominant under low carrier densities when droop mechanisms can be avoided. This simplification is helpful for the analysis yet it still leaves an elephant in the room: Non-commercial (non-optimized) samples show a vast range of different effects difficult to describe with current p - n junction theories. The opposite is also true: modern commercial devices resemble closely an ideal diode, therefore the analysis is simplified and more easily explained. In other words, highly efficient commercial devices can be properly described with traditional theory but non-optimum samples require a careful analysis using a combination of electrical and optical excitations. Without

this careful study, the amount of processes that happen at the same time in these samples may lead to misguided conclusions.

Chapter 2 gives a brief introduction of GaN-based semiconductor materials. Advantages and characteristics of these materials are explained along with the crystal structure, growth techniques and the epitaxial layer structure of the wafers used here. In Chapter 3 there is a brief description of the micro-fabrication techniques used to fabricate optoelectronic devices and this chapter includes a description of the process steps that we used to fabricate the devices that are characterized in this thesis. The electro-optical characterization of GaN LEDs requires the understanding of a combination of electrical and optical excitation techniques that are discussed extensively in chapter 4. It begins with the study of the LEDs under electrical excitation through current-voltage characteristics and the analysis of the different contributions using the ideality factors. A method to extract the internal quantum efficiency of a device using only light output versus bias current data is also explained and finally capacitance-voltage measurements are explained as a method to study the doping profile inside the LEDs. Regarding optical excitation, optical resonant photoluminescence is introduced to study the photovoltaic effects of GaN LEDs and fluorescence microscopy is presented for imaging the spatial dependent luminescent properties.

In chapter 5 these techniques are applied to two structures with 1.5 nm thin quantum wells with the essential differences being the number of QWs in the MQW region (5 & 10) and the thickness of the barrier layers (6.6 & 4 nm). Electrical, optical and photovoltaic ideality factors are compared for the diodes and with a commercially sourced LED wafer as a reference. Chapter 5 also presents a method to estimate both the internal quantum efficiency (IQE) and the extraction efficiency (EE) using light – current – voltage (LIV) measurements. This work concludes with the final chapter 6 where some conclusions of the work done during the past 4 years are presented.

Chapter 2 – Introduction to the Gallium Nitride system

The previous chapter introduced GaN as a solution to fabricate efficient violet and blue light emitting diodes. In this chapter the characteristics and advantages of this material for visible LEDs are presented. An introduction to the crystal structure and growth techniques employed with GaN are given here. The last part of this chapter gives information about the layer structure of the wafers employed in the fabrication of the devices characterized in next chapters.

2.1 Characteristics and advantages of GaN-based LEDs

GaN has a bandgap energy at room temperature of about 3.41 eV corresponding to a wavelength of about 365nm which is in the UV range of the spectrum. To get longer wavelengths and therefore the high energy part of the visible spectrum it is then required to lower the band gap. With GaN, this can be achieved by adding small percentages of indium to the GaN crystal.

Figure 2.1 shows the bandgap energy of GaN, AlN (6.015 eV) and InN (0.7 eV) [1] and the lattice constant parameter a . In principle, it is possible to vary continuously the bandgap between the two extremes (UV to infrared), while maintaining direct recombination. This possibility is a major technological advantage for GaN because this allows for tuning the bandgap with accurate control. Unfortunately, high indium (aluminium) content InGaN (AlGaIn) layers are difficult to achieve and lead to a poor quality material due to the different optimum growth conditions for indium (aluminium) III-nitride alloys.

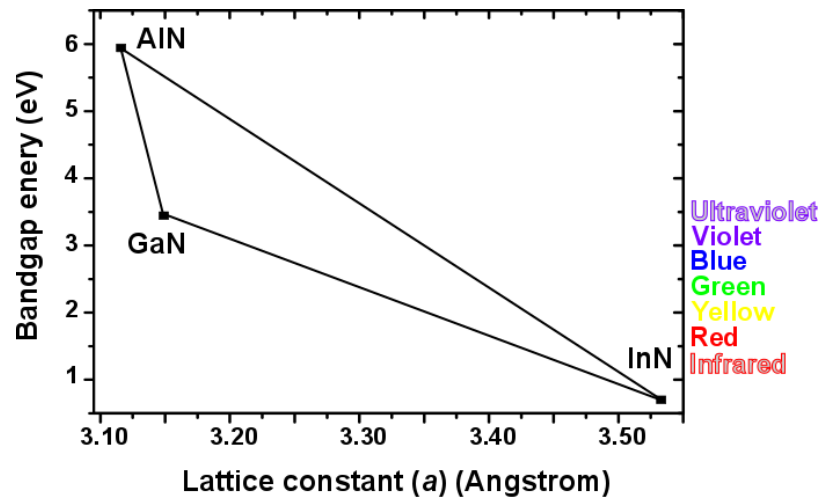


Figure 2.1: Bandgap energy vs lattice constant (a) for wurtzite III-Nitrides. Addition of Al to GaN increases the bandgap allowing UV emission and addition of indium decreases the bandgap for longer wavelength colours. In both cases direct recombination is maintained.

There are commercially available highly efficient blue GaN-based LEDs with external quantum efficiencies in excess of 80% [2]. However, this is not true for green GaN-based LEDs where the highest external quantum efficiency is presently about 30% [3]. If we move further towards yellow and orange, efficiencies are even lower and no gallium nitride based devices are commercially available yet in these colours. The main reason for this loss of efficiency is that, when the percentage of indium is increased, this element tends to form clusters [4]. These indium clusters are efficient non-radiative recombination centres which reduce the radiative efficiency of the devices. Research on different crystallographic orientations has shown that semi- and non-polar planes have enhanced indium incorporation in the QWs [5], which could be a solution to achieve longer wavelength GaN LEDs.

There are other advantages of using GaN for LEDs, some of them are now summarized:

- It has a good thermal conductivity ($\kappa = 1.3 \text{ W}\cdot\text{cm}^{-1}\cdot^\circ\text{C}^{-1}$), leading to simpler thermal management and packaging with a reduction in system volume and weight.

- It has a fast switching speed and reduced electrical noise. This allows for the use of LEDs in optical communication systems.
- The materials are environmentally friendly and no hazardous materials are required for the fabrication of devices.
- The material is very robust and LED devices have longer lifespans than traditional lamps.

As a disadvantage, GaN is a very complex material and some of the light generating mechanisms are still poorly understood. This lack of understanding has important consequences for the overall device, and thus research has been devoted to improve it.

2.2 Crystal structure of GaN.

GaN usually crystallizes in hexagonal wurtzite structure at ambient pressure. Zinc blende structure is metastable and is produced at low substrate temperatures (~ 600 °C) and high gallium fluxes. Rock salt GaN crystals are possible to obtain, yet it requires ultrahigh pressures (>37 GPa) and despite the interest in this crystallization due to its unique electrical and optical properties, which are different from the wurtzite form, it is not yet possible to grow the rock salt structure in thin film form. For optoelectronic devices and applications as LEDs the wurtzite structure is more commonly used because at room temperature and normal pressure, the wurtzite structure is thermodynamically more stable than the zinc blende structure. In this work only wurtzite GaN structures were used so further information about the zinc blende and/or rock salt is omitted. The wurtzite structure for GaN is sketched in figure 2.2-a where continuous lines indicate the hexagonal type of this structure and dotted lines indicate the covalent bonds between gallium and nitrogen atoms. In this structure each atom has four tetrahedral bonds, and due to the stronger electronegativity of nitrogen compared with gallium, indium and aluminium, these compounds have a strong ionic character which improves stability.

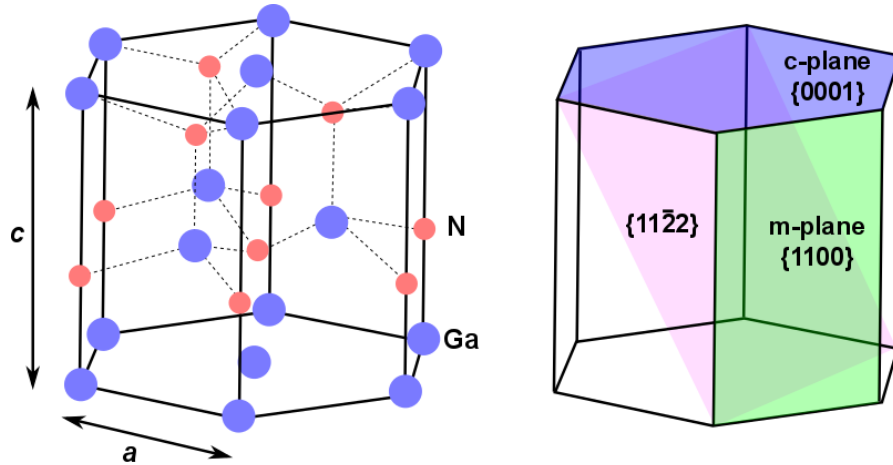


Figure 2.2: (a) Crystal structure of wurtzite GaN. Ga-N bonds are shown as dashed lines. (b) The orientation of the polar c-plane $\{0001\}$ (blue), the non-polar m-plane $\{1100\}$ (green) and the semi-polar $\{11\bar{2}2\}$ plane (purple) within the hexagonal structure.

Traditionally, InGaN-based LED structures are grown in the Ga-polar $[0001]$ direction. The $\{0001\}$ plane is highlighted in blue in figure 2.2-b. This is the orientation that yields the strongest internal electric field induced by spontaneous and piezoelectric polarization in wurtzite III-nitrides. The spontaneous polarization comes from the deviation of the GaN unit cell from the ideal wurtzite geometry and the strong ionic character of the covalent bond between gallium and nitrogen atoms. The crystal symmetry causes the polarization field to align with the $[0001]$ direction and spontaneous polarization coefficients are of the same order of magnitude as in ferroelectric materials [6]. The piezoelectric polarization comes from the deformation of the lattice parameters induced by strain, and this polarization along the $[0001]$ direction depends on two independent coefficients that are much larger and opposite in sign compared to other III-V materials [6].

The existence of these fields introduces a pronounced tilting of the energy band edges of InGaN QWs as depicted in figure 2.3. This causes a spatial separation between electron and hole wave-functions and hence reduces the internal quantum efficiency (IQE) of the device. Increased indium incorporation required to tune the emission wavelength from blue to green further increases this effect.

This is the foundation of the lack of highly efficient devices in the green band (~500 to 570nm). Furthermore, the tilting of the band edges also narrows the effective width of the QWs, thereby increasing the effective carrier density favouring Auger non-radiative recombination. Effective quantum barrier (QB) heights are reduced as well by the tilting of the bands and this leads to increased carrier leakage under applied bias. Auger recombination and carrier leakage have been proposed as the main mechanisms responsible for the efficiency droop phenomenon observed in GaN LEDs [7, 8], yet as mentioned in chapter 1 the origin of the droop remains controversial [9].

The polarization fields are not only present in the QWs but throughout the entire MQW structure. In chapter 5 differences in the piezoelectric fields across 2 samples are investigated. It will be shown that one of the samples has a larger piezoelectric field across the QWs and consequently a lower field across the barriers when compared to a second sample. This is a consequence of the increased thickness of the quantum barrier (QB) in the first sample, the samples being *p-i* (MQW)-*n* structures with piezo-electrically charged interfaces. Figure 2.3 shows this effect of barrier thickness for a simulated QW with 23% of indium. Black lines are for a sample with a 1.5 nm thick QW with a 6.6 nm thick QB and red lines are for a similar structure with a 4nm thick QB. The increased electric field in the thinner QB can be seen by the steeper slope of the red lines. Similarly, in the inset of figure 2.3 the higher slope corresponds to the black line, indicating a higher field strength in the QW for the sample with the thicker barrier. A more detailed analysis of the effects of piezoelectric fields and their impact on the performance of GaN LEDs will be presented in chapter 5.

Better indium incorporation and the reduction of the piezoelectric fields are some of the ways that people explore to get better device performance, by growth of III-Nitride materials with non-polar and semi-polar crystallographic orientations [10]. Semi-polar and non-polar planes have shown reduced or completely suppressed in-built electric fields, increased stability of colour emission [11] and higher maximum indium incorporation [5]. Figure 2.2-b shows in green the non-polar plane (1100) (m-plane) and in violet the semi-polar plane (11-22).

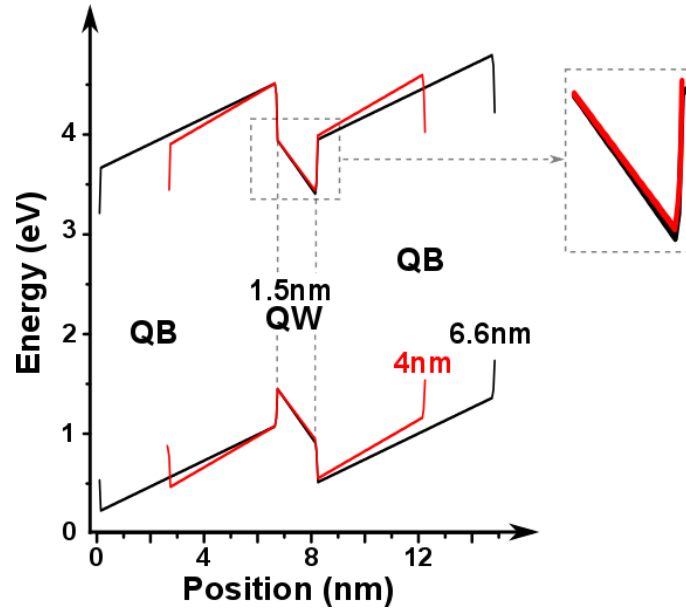


Figure 2.3: Simulated 1.5nm QW with 23% of indium content and different QB thicknesses of 4 and 6.6nm. The existence of polarization fields gives InGaN QWs their particular triangular shape. Piezoelectric fields in the QW are reduced for thinner barriers while the field in the barrier is increased which leads to differences in the performance. Inset: close-up of the conduction band profiles near the bottom of the QWs

The basic hexagonal wurtzite structure shown in figure 2.2-a corresponds to undoped GaN. Films of pure GaN usually show *n*-type conductivity (unintentional *n*-type doping). This conductivity is attributed to nitrogen vacancies [12] and/or residual impurities that replace nitrogen atoms [13]. As *p-n* junction devices, GaN LEDs are the result of the union of two GaN films with different intentional doping types. For the *n*-type doping, silicon is the most common dopant element and electron concentrations as high as $6 \times 10^{19} \text{ cm}^{-3}$ can be achieved [14]. Incorporation of silicon atoms into the crystalline structure increases the stress on the films which could result in degradation of the films [14]. For the *p*-type doping, magnesium is commonly used as the dopant. During the growth of GaN in a hydrogen ambient, magnesium dopants are passivated by hydrogen forming Mg-H complexes. These complexes increase the parasitic resistance of the *p*-layer resulting in a high turn-on voltage required to obtain light. It is then required to do an annealing step to activate magnesium dopants. The hole concentration in

p -GaN is lower than the electron concentration in n -GaN because the ionization energy for magnesium acceptor atoms in GaN is 170 meV, which is much larger than the thermal energy at room temperature (26 meV at 300 K). The result is a reduced p -layer conductivity and higher sheet resistance on the p -side compared with the n -side. In chapter 3 a discussion about the effect of doping level in semiconductor - metal interfaces will be discussed.

The main issue regarding GaN crystals is the limited availability of high quality pure GaN substrates. Unlike other III-V materials used for solid-state lighting as for example GaAs, GaN crystals are very difficult to grow in a bulk form so it is required to use non-native substrates with a similar lattice constant. There are different substrates that can be used to grow GaN crystals on, such as silicon or silicon carbide although the most common substrate used these days for GaN-based LEDs is sapphire due to its wide-gap transparency, robustness, low cost and ability to withstand high growth temperatures [15].

The main drawback of using these substrates is that they do not match perfectly the crystal structure of GaN. In addition, GaN layers are usually grown around 800-1000 °C so the thermal expansion coefficients play an important role when wafers cool down [16]. The result of the adoption of these non-native substrates for GaN growth is the appearance of high densities of threading dislocations (10^8 to 10^{10} cm⁻²) originating from the GaN/substrate interface [17]. These dislocations act as non-radiative recombination centres in III-V arsenides [18], phosphides [19], and ZnSe based II-VI semiconductors [20]. In general, there are two principal types of defects that any growth technique should avoid:

- Point defects: these are sites in the lattice where instead of the gallium or nitrogen atom we find an impurity, a vacancy or an interstitial. All of these induce states somewhere in the middle of the bandgap which act as non-radiative recombination centres, thus reducing the efficiency of the device. The density of these defects could be reduced by choosing optimum growth temperatures and III-V reactant ratios.

- Extended defects: these are mainly dislocations. In GaN there is no way to completely avoid the formation of dislocations, so the aim is only to minimize the density of them.

High densities of defects in GaN devices cause degradation of the device properties [21] and reduction of the efficiency of LEDs [22]. GaN is robust to threading dislocations yet depending on the type of the dislocation it could still act as non-radiative centre reducing the overall efficiency [23].

2.3 Growth techniques of GaN thin films

GaN is grown epitaxially to obtain high crystalline structure quality. There are several methods to achieve epitaxial growth of semiconductors: vapour-phase, liquid-phase and solid phase, although this latter one is mainly used for recrystallization and crystal-damage healing [24]. There are several works describing polar, semi- and non-polar GaN growth using liquid-phase epitaxy (LPE) yet there are several drawbacks: liquid gallium does not wet sapphire well, which limits the growth of thin-film layers. Also, GaN has to nucleate in the liquid/solid phase, which is not a trivial task. Finally, the development of each new layer or multilayer structure by LPE requires typically between 1-3 years of research effort, in contrast to vapour-phase epitaxy methods which require typically around 3 months [25].

This leaves vapour-phase epitaxial growth (VPE) as the main technique used nowadays. Currently, the best quality GaN crystals can be manufactured only by gas phase techniques. In addition to the faster development of new structures, VPE methods allow atomic level control of the thin-film layers, which is required to grow the epitaxial structure of highly efficient devices. Here is a brief description of three of the most common techniques used for the growth of GaN:

Hydride vapour phase epitaxy (HVPE): This technique is commonly used to achieve the difficult growth of free-standing GaN layers. It is a simple growth technique that uses chlorine to transport group III materials and is capable of high growth rates of around 100 $\mu\text{m}/\text{h}$ with a defect density of 10^5 cm^{-2} [26]. This

high growth rate however is not suitable to grow sharp interfaces so this technique is mainly used for substrate growth. HVPE uses gaseous HCl passed over metallic gallium in liquid form which results in GaCl₃ gas. This gas is then carried into the reaction chamber by N₂ gas to react with NH₃ to form solid GaN, HCl gas and H₂ gas. HVPE growth requires a hydrogen environment and GaN growth requires temperatures in the range of 1000 to 1500°C. Also, growing GaN LED structures requires the additional supply of precursors containing Al and/or Mg and the use of these precursors adds some complication due to exchange reactions with the hot quartz reactor walls which reduce the reactor lifetime.

Metal-organic chemical vapour deposition (MOCVD): This is the most common technique employed for GaN epitaxial growth and capable of achieving high quality films. It was pioneered by Manasevit et al. [27] and it relies on volatile metal-organic compounds to transport metallic atoms that are themselves relatively non-volatile at the convenient deposition temperatures around 900-1000 °C. GaN layers are usually grown on a sapphire substrate while trimethyl gallium (TMGa) and ammonia (NH₃) are used as sources for gallium and nitrogen respectively. The high temperature used for MOCVD is required to break the N-H bonds in ammonia effectively. Solids from the pre-cursors start to be deposited on the sapphire substrate by chemical reactions with a usual growth rate of 30 nm/min. Trimethyl indium (TMIn) and Trimethyl aluminium (TMAl) can be used as well to obtain AlGaN and InGaN alloys for the electro-blocking layer (EBL) or the QWs respectively. Additional AlN or GaN buffers may be inserted to prevent cracking and defects caused by thermal strain between GaN and sapphire [28, 29]. This step is called nucleation and these layers are usually grown at a lower temperature (500 to 750 °C) to form a few nanometres of GaN with high dislocation density. Lower temperatures are necessary so the energy of the atoms does not prevent them sticking on the surface to form the GaN layer. Afterwards, the sample is heated and thermally annealed at high temperature where some desorption and re-structuration of the atoms in the crystal happens. The rest of the LED structure will then be grown on top of this coalesced layer. To achieve silicon doped *n*-GaN, disilane (Si₂H₆) or silane (SiH₄) is used as the

pre-cursor. For magnesium doped *p*-GaN the pre-cursor is usually cyclopentadienylmagnesium (Cp₂Mg).

Molecular beam epitaxy (MBE): This is another technique that allows us to have atomically sharp interfaces and growth of very high quality films. Here nitrogen is usually supplied from a plasma source so the high temperature required to break ammonia N-H bonds can be avoided. The main drawbacks that keep MOCVD as the chosen technique are the need for ultra-high vacuum and the low growth rate of around 1.5µm/h. This low growth rate makes this technique very expensive.

GaN can be grown on gallium and nitrogen faces. The usual grown face is gallium since it gives a better surface morphology and this *Ga*-face is used in all the samples in this work. Growth of the nitrogen face is also possible using high Mg doping, yet the main drawbacks are the surface quality and stability of the film.

2.4 Layer structure of the wafers used in this thesis.

Three different wafers are used throughout this work: two wafers were grown by MOCVD on 2-side polished low defect density templates from the same batch. These templates consist of a (0001) sapphire substrate followed by 3µm of undoped GaN and 1µm of Si-doped *n*-GaN. Both wafers have an additional 1µm of Si-doped *n*-GaN deposited as the first layer. The first wafer consists of a 5QW structure with 5 x 1.5nm In_{0.23}Ga_{0.77}N QWs with 6.6nm thick QBs. The second wafer contains a 10QW structure of 10 x 1.5nm In_{0.23}Ga_{0.77}N QWs with 4 nm thick QBs. The QWs were grown using the quasi two-temperature (Q2T) method [30] where the InGaN QWs were grown at a temperature of 750°C and the first few nanometres of the GaN barriers were grown at the same temperature. The temperature was then ramped to 900°C to grow the remainder of the barrier. The 5QW (10QW) sample was capped with 110 nm (100 nm) of Mg-doped *p*-GaN. No electron blocking layer (EBL) or additional layers were grown. A summary of the structure of the samples is shown in figure 2.4. The actual thicknesses of these layers were confirmed using X-Ray diffraction and the measured thicknesses are

shown in table 2.1. Both the growth and the XRD measurements were done in the Department of material science and metallurgy of the University of Cambridge. The wafers were grown in sequential runs with similar growth conditions. The expected emission wavelength of 470 nm was confirmed by photoluminescence (PL) measurements with full width at half maximum (FWHM) of around 25nm. In addition to these samples, a commercially sourced wafer of unknown structure is included. This sample has a similar wavelength emission around 465 nm and serves as a reference. The structure could be expected to contain an EBL and the presence of an InGaN layer (or super-lattice) under the QWs was detected with photoexcitation experiments as shown in chapter 5. When optically excited, this layer shows emission around 420 nm which implies a percentage of indium around 15%.

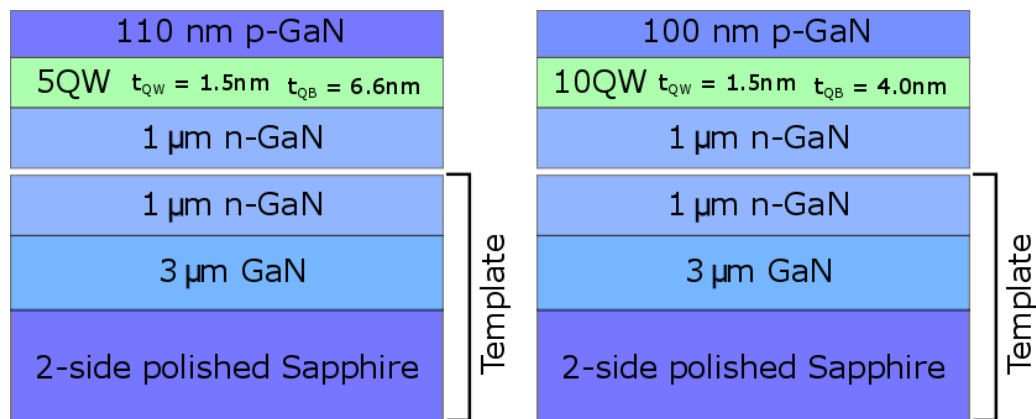


Figure 2.4: Layer structure of the 5QW and 10QW wafers.

Table 2.1: XRD results of the wafers with known structure.

Sample	Mean period thickness ($t_{QW} + t_{QB}$) (nm)	XRD results - thickness (nm)		
		InGaN wells (23% In)	GaN barriers	p-GaN
5QW	8.2	1.5	6.7	110
10QW	5.4	1.5	3.9	100

Chapter 3: Structure and fabrication of LED devices

LEDs can be designed with several configurations regarding the extraction of the light. Because each of these available configurations have their own positive and negative attributes, it has to be carefully evaluated which one fits better our requirements. In addition, the final electrical and optical characteristics will have a strong dependence in the fabrication steps, for example, the choice of the metal contacts will have an impact in the electrical characteristics and etching steps will shape the LED affecting the extraction efficiency. To explain the decisions taken for the LEDs characterized in following chapters, this chapter gives an introduction about the general structure of LED devices and the two types of fabrication runs employed in the LEDs of this thesis. Fabrication techniques involved in the process of making LED devices are briefly introduced here as well. The physics of semiconductor-metal interfaces are discussed in detail to explain the selection criteria of metals for GaN LEDs. This chapter ends with a description of the devices used in the rest of this work.

3.1 Design of LED devices

The most important characteristic of LED materials is the capability of emitting light from its active layer. To get the benefit of this light, it needs to be extracted from the semiconductor. There are two basic configurations used in LEDs depending on the direction of the light extracted:

- Surface extraction: light is extracted from the perpendicular direction to the plane of the p - n junction.
- Edge extraction: light is extracted parallel to the plane of the p - n junction.

In this work the focus is on surface extraction, because it opens the possibility to use larger contacts and collect emission from larger areas. To obtain high output power it is required to enhance the light extraction efficiency which can be increased by reducing the losses through elimination of total internal reflection. Some light-extraction methods reported in the literature are: roughening the p -

GaN surface [1], double-embedded photonic crystals [2], self-assembled micro-lens arrays [3], concave microstructures [4], embedded air-void photonic crystals in GaN layers [5] and patterned micro-hole arrays on a LED surface [6]. Research has been done on GaN nanorods that provide large sidewall-surface areas as pathways for photons to escape and also function as light guiding pillars for light extraction in the longitudinal direction [7]. Hybrid structures have been reported also to reduce internal reflection and increase photon emission at the same time [8]. In chapter 6, a method to estimate the quantum efficiencies and the extraction efficiency is reported. Yet, the detailed study of the different light extraction strategies is beyond the scope of this thesis.

Typically, commercial fully packaged LED devices consist of three main parts: the semiconductor die, the lead frame which houses and connects the die and the encapsulation which protects the assembly and usually works as an optical lens. Because the aim of this work is the characterization of the GaN material, the focus is just on the semiconductor die. The different parts of a LED die are schematically depicted in figure 3.1. In general, it includes the following:

- The p -metal provides an electrical connection to the p -doped semiconductor. For top surface emission LEDs the p -metal is selected to be as transparent as possible at the emission wavelength. Alloys such as Ni/Au or a transparent conductive oxide such as indium tin oxide (ITO) are often employed for this purpose. For substrate emission, a highly reflective metal is deposited to redirect the light to the substrate. Alloys containing silver or aluminium are suitable due to their high reflectance (>85% and >90% for visible wavelengths, respectively).
- The active area of the device is where carriers recombine and light is generated. To improve efficiency in modern LEDs it consists of a series of QWs that confine carriers to increase the radiative recombination rate.
- The n -metal provides the electrical connection to the n -doped semiconductor. In the traditional growing order, the n -GaN layer is embedded in the structure and not accessible without an additional step to remove the material covering the layer. Dry etch is the common solution for exposing the n -GaN. Due to the typically low sheet resistance of the n -GaN it is possible to achieve good

lateral spreading of the current. This allows us to place the n -contact on the side of the etched mesas as indicated in figure 3.1 without degrading the electrical performance and allowing for better light extraction. Yet LEDs could be fabricated with the n -metal deposited on the back side of the wafer. Such LEDs require the removal of the substrate and any nucleation layer to expose the n -layer.

- The substrate most commonly used in GaN LEDs is sapphire which is transparent across the visible spectrum. Yet, depending on the design and further packaging steps, it may be required to do additional processes as substrate removal, polishing/thinning or even depositing a reflective metal to redirect the light.
- Bond pad metals are usually deposited on top of the p - and n -metals for two main reasons: to provide an additional spreading layer that could increase the current injection and also, to improve the wiring of the device to a package for electrical connection. Bond pad metals are selected not to form a good electrical contact with the GaN but to get the best adhesion between the underlying metal contacts and the material used for wiring to the package.

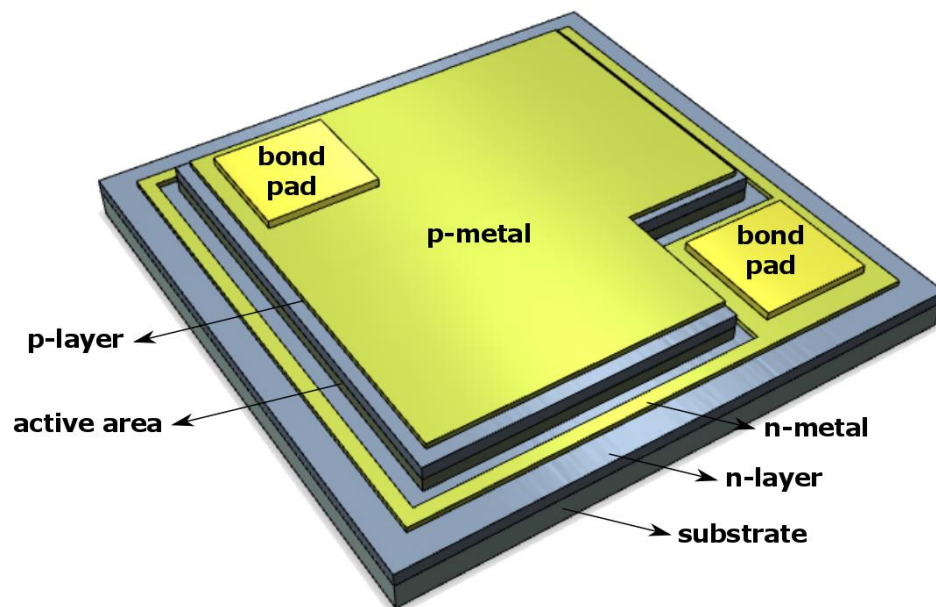


Figure 3.1: Basic parts of LED dies. The p - and n -layers are metallized to provide electrical contacts. Under forward bias holes and electrons are injected into the active area where they recombine.

For the experiments performed in this work two types of fabrication runs were carried out:

- Quick evaluation runs: This approach is used to quickly evaluate wafers minimizing processing steps. The p -metal is selected to form a good contact without annealing if possible. A mesa etch step is not required although it is recommended to reduce current spreading and also expose the n -side for future n -metal deposition. Regarding the n -contact, two different approaches have been used:
 1. Pseudo n -contact: This is applied when the aim is to further minimize the number of processing steps. When cleaving/dicing the sample a small scratch is made on the edge of the sample to expose a small portion of the n -type material. This area will be covered with the p -metal when deposited and can be used as a pseudo n -contact for electrical measurements. This technique does not require additional processing but the voltage drop in this pseudo- n -contact may be high when compared with a proper n -contact.
 2. Large area (blanket) n -contact: In this case a mesa etch is required to expose the n -layer and deposit a large area metal, covering some of the exposed areas, for example the border areas on the wafer piece. The difference with a traditional n -contact is that in this case patterning can be done without any lithography mask. This large contact works very well as an n -contact, introducing only a small additional voltage drop; on the downside, several devices are lost which may be an issue for small area samples.
- Fully processed run: It consists of p -metal deposition, mesa etch, n -metal deposition and bond pad deposition. Further steps as thinning and polishing the substrate and dicing into individual dies are usually required to prepare fully packaged devices.

When processing a semiconductor as in this case GaN, any dust particle can affect the processing in many ways: it could act as an opaque area on the pattern to transfer from a photomask or could cause a short circuit between isolated terminals. As a consequence, the fabrication of LEDs as other similar photonic devices requires to be performed in a clean processing room where the total number of dust particles per unit volume is tightly controlled.

3.2 Fabrication of LEDs

3.2.1 Optical lithography

The main purpose of lithography is to transfer a pattern from a photomask to a light sensitive material called photoresist. In optical lithography ultraviolet (UV) light with wavelengths ranging from 200 to 400nm is used for the transfer process. Photomasks for optical lithography generally consist of an opaque chrome layer on top of a transparent fused silica glass plate. This chrome film does not transmit the light at the working wavelength and it is patterned so as to expose the photoresist in selected locations.

The light can break chemical bonds in positive resist causing it to wash away from the exposed areas when immersed in a developer solution. Figure 3.2 shows as an example an annular resist pattern on a GaN sample. Here darker areas are covered by a positive photoresist that will prevent the deposition of the metal onto the semiconductor surface.

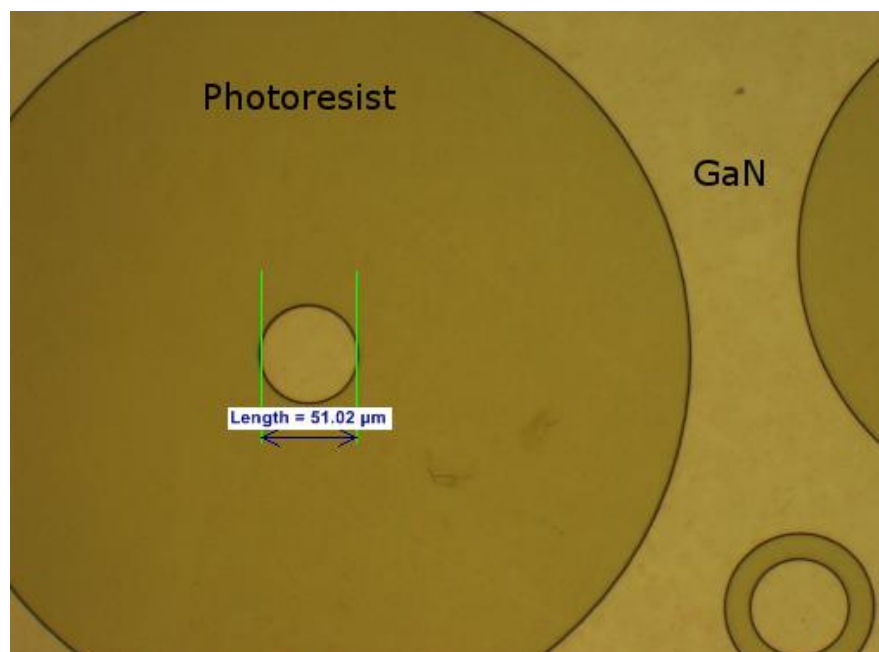


Figure 3.2: Example of a lithography performed to achieve circular metal contacts. Darker areas are covered by positive photoresist and lighter areas are uncovered for metal deposition.

3.2.2 Ohmic contacts on GaN

The selection of the metals to be deposited on each side of the p - n junction is a critical decision in the processing of LEDs. The metal/semiconductor interface must be inert, oxide and defect-free and the interface has to form a low resistance junction to obtain good conduction from the metal to the semiconductor. For LEDs the aim is to obtain an ohmic contact where the current can flow in both directions and the current increase/decrease is linear with the voltage. It is also required that the contact resistance is as low as possible so the voltage drop in the contacts is small compared to the voltage drop in the p - n junction.

The selection of the metal for GaN-based LEDs is not a trivial decision because it is difficult to find suitable candidates that meet all the requirements: when a metal and a semiconductor are in contact under thermal equilibrium, the Fermi level (E_F) which describes the maximum energy level available for electrons at absolute zero, must be equal across the interface. To meet that requirement the energy bands of the semiconductor close to the metal bend forming a barrier for the carriers to enter the semiconductor which is called a Schottky barrier (Φ_B). To obtain the desired ohmic contact, the critical parameter that has to be taken in account is the Schottky barrier height (Φ_B). The formation and the height of this barrier at the interface between the metal and an n -type semiconductor depends on the work function of the metal (Φ_m) and the semiconductor vacuum electron affinity (χ). For the metal p -type semiconductor interface, the bandgap of the semiconductor also has to be taken in account. If the resultant barrier height is negative or zero, carriers are able to flow in or out of the semiconductor with minimal resistance forming a true ohmic contact.

Figure 3.3-a shows the interface between a metal and an n -type semiconductor under thermal equilibrium. The E_F is constant through the interface and the semiconductor bands bend upwards to meet this requirement. To obtain an ohmic contact it is required to find a metal with a work function close or smaller than the vacuum electron affinity of 4.1 eV. Currently, there are several metals and alloys available that meet these requirements. A commonly used metallization for the n -side is Ti/Al/Ti/Au deposited by electron beam

evaporation followed by rapid thermal annealing (RTA) in nitrogen ambient at temperatures ranging 750 to 900 °C. Surface treatments as HCl dips and RIE etching can be applied to reduce the resistance of the contacts [9].

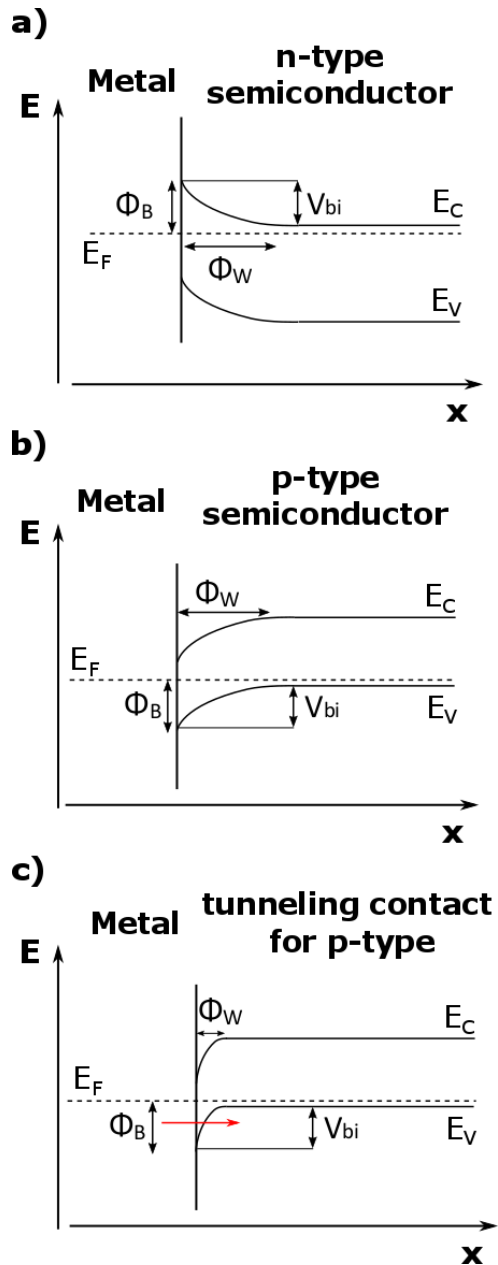


Figure 3.3: Metal/semiconductor interface energy diagrams under thermal equilibrium: a) metal n-type interface, b) metal p-type interface, c) metal high doped p-type interface: the high doping reduces the width of the Schottky barrier (Φ_W) and holes can tunnel into the semiconductor (red arrow).

Despite the fact that specific contact resistances lower than $10^{-6} - 10^{-8} \Omega \text{ cm}^2$ have been achieved using Ti/Al-based metallization schemes and various surface treatments [10], the development of n -contacts to GaN is not a trivial task because the success in decreasing the contact resistance by RTA annealing and various surface treatments heavily depends on the doping of the n -type GaN, the metallization and whether the deposition is on the Ga -face or the N -face of the crystal. As an example, J. Aguilar reported in [9] the improvement of n -contacts made by deposition of Cu/Ge/Au (40/97/40 nm) and Ti/Al/Au (20/60/300 nm) by a 1 minute immersion in HCl:DI (1:3) to remove native gallium oxides, prior to metal deposition. However; figure 3.4 shows the effect of performing a 4 minute dip before metal deposition in HCl:DI (1:2) on contacts made by Cr/Au (50/300 nm) deposited on N-face GaN. Figure 3.4-a shows that these contacts are ohmic as deposited without treatment, while figure 3.4-b shows that after treatment these contacts are not ohmic. This is an indication of how the same treatment could lead to opposite results depending on the face where the metals are deposited.

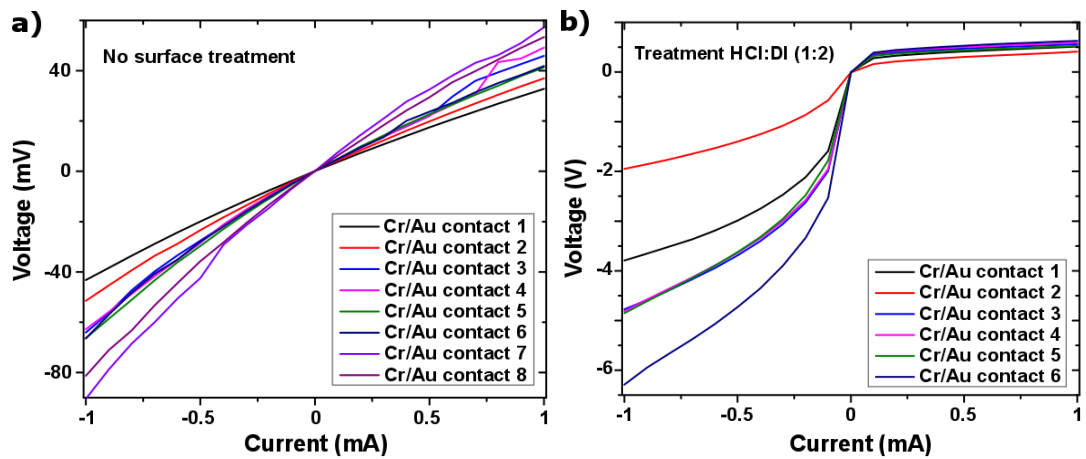


Figure 3.4: Current – voltage characteristics for contacts deposited on N-face n -doped GaN made by Cr/Au (50/300 nm) a) without pre-treatment and b) with an HCl:DI (1:2) dip before metal evaporation.

Figure 3.3-b shows the energy diagram of a metal p -type semiconductor interface where the semiconductor energy bands bend downwards forming the Schottky barrier. For p -contacts $\Phi_W = E_g - (\Phi_m - \chi)$ so the formation of ohmic contacts for the p -doped GaN requires a material with a metal work function to be close or larger than the sum of the vacuum electron affinity and the bandgap of GaN. This is problematic for GaN because the work function of most metals is around 5 eV [11] and the electron affinity of GaN is already 4.1 eV. Adding that the bandgap is 3.42 eV at room temperature the requirement for the metal is to have a work function of more than 7 eV which is currently not available. One solution to get good conductivity is to add a heavily doped layer on the surface of the LED which is usually called a p^{++} -layer. In this case the width of the Schottky barrier is reduced allowing carriers to easily tunnel through it. This tunnelling assisted injection is depicted in figure 3.3-c and can provide an ohmic contact for doping concentrations higher than 10^{18} cm^{-3} and is the most common type of contact used for p -doped GaN.

Despite these limitations, contact resistivity values as low as $10^{-6} \Omega \text{ cm}^2$ for contacts on p -type have been claimed using Zn-Mg solid solution/Au [10] although such claims have to be treated with caution as explained later. In table 3.1 published data for several metal contacts on p -type GaN are summarized. In contrast to n -GaN where lateral current spreading is possible due to its low sheet resistance, p -GaN is a highly resistive layer. It is then required for the p -contact to cover the whole area of emission while the n -contact is usually deposited on the side. Two possibilities arise: a (semi)transparent p -contact that allows light to pass through it or a reflective contact that reflects the light to be emitted through the substrate.

Obtaining an accurate value for the specific resistance (below $10^{-4} \Omega \text{ cm}^2$) of metal contacts to p -GaN is a difficult task. The general method to measure the specific resistance is called circular transmission line method (cTLM) [14] and employs a set of concentric metal contacts with different un-metallized gap separations, as seen in figure 3.2. For very low contact resistances, this analytical method has a severe limitation: Due to the high p -GaN resistivity the resistance contribution of the p -GaN material as the current crosses the unmetallized gap

swamps the contribution of the metal contact that you try to evaluate. All current is carried in a very thin contact region just along the perimeter of the contact, and therefore, very sensitive to the evenness of the contact outline.

Table 3.1: Overview of some published data for p-contacts on GaN [12]

Contact Material	Thickness (nm)	Specific resistivity ($\Omega \text{ cm}^2$)	RTA conditions
Ni/Au	10/5	$< 10^{-4}$	500 °C, 10 min in air
	5/5	4×10^{-6}	500 °C, 10 min in air
	5/20	1×10^{-4}	400 - 600 °C
	20/100	$< 4.8 \times 10^{-6}$	500 °C, 1 min in air
	20/100	4.5×10^{-6}	500 °C, 10 min in air
	5/5	8.9×10^{-5}	None
Cr/Au		2.6×10^{-3}	None
Pd/Ag/Au/Ti/Au	1/50/10/30/20	1×10^{-6}	800 °C, 1 min in air
Ni/Au/Ir/Au	50/80/50/80	2.3×10^{-4}	500 °C in N
Ni/Au/CrB ₂ /Ti/Au	50/80/50/20/8	2×10^{-4}	700 °C, 1 min in air
	0		
Ni/Au/ZrN/Ti/Au	50/80/50/20/8	2×10^{-4}	700 °C, 1 min in air
	0		
In _{0.19} Ga _{0.81} N/Pt/Au		1.1×10^{-6}	None
Pd/Au	20/500	4.3×10^{-4}	None
	12/500	4.3×10^{-4}	None
Pt	25	2×10^{-5}	None
	8	4.7×10^{-5}	None
Rh/Au	5/5	9.3×10^{-6}	None

Commercially available devices mainly use transparent *p*-contacts because reflective contacts require flip chip mounting which has different requirements than the common wire-bonding used for other semiconductor devices. Traditionally, thin-metal-based contacts as Ni/Au have been the choice for the *p*-contact, yet the main drawback when using these contacts is that the transparency is about 70 percent and the contact has significant absorption in the visible range between blue and green (450 – 550 nm). Nowadays, indium-tin-oxide (ITO) has replaced thin-metal-based electrodes due to its transparency of 90% and specific contact resistivity down to $10^{-4} \Omega \text{ cm}^2$ [15]. These contacts as well are facing a big drawback: indium is becoming a scarce material so production costs have been rising quickly during the last few years and other transparent conducting oxides such as ZnO and SnO₂ are being studied as alternatives to ITO [16].

Finally, one event that can be easily overlooked is the effect of fabrication steps of one contact on the performance of the contact already fabricated. Treatments with acids, high temperature annealing or exposition to different plasma gases employed in dry etching or oxide deposition can be detrimental to metal contacts so fabrication steps have to be planned carefully.

3.2.3 Etching techniques

Semiconductor microfabrication requires a high precision technique to remove semiconductor materials for reasons such as exposing the *n*-doped layer, mesa etching, removal of nucleation layers and improving light extraction. The high precision control required for these steps makes techniques such as wet chemical etching and/or mechanical grinding not suitable for this purpose. The selective removal of material using an acid or mordant is called etching. In semiconductor manufacturing there are two main approaches: wet etching which is done by dipping the sample in a liquid solution that attacks the semiconductor and slowly removes material from the exposed surfaces. The *c*-plane of GaN crystals is resistant to chemical attack which makes this technique invalid for patterning GaN. The second approach is dry etching that relies on the generation of plasma

which attacks the exposed parts of the semiconductor's surface. It allows very good control of the etching rate so the amount of material being removed can be controlled accurately. The anisotropic character of dry etching also allows high sidewall angle features and deep steps to be obtained without compromising the pattern dimensions in the semiconductor.

Dry etching is the only option when etching c-plane GaN and has been used throughout this work. As an example of this process, figure 3.5 shows a SEM image with the result of two dry etch processes performed in GaN material using inductively coupled plasma (ICP) etching with chlorine chemistry. The first process uses Cl_2 to achieve high sidewall angles, and a high etch rate (~ 730 nm/min). As indicated by the profile line, in this case the angle between the surface of the sample and the wall is 76° (bright wall on the left). The second process uses BCl_3 with a lower etch rate (~ 300 nm/min) and provides a smaller angle of the wall. In this case this angle is 45° as depicted on the right hand side of figure 3.5.

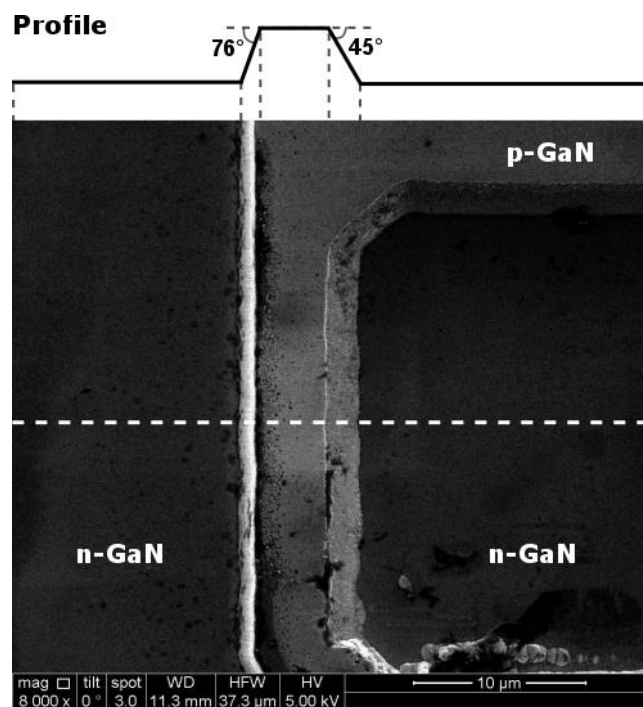


Figure 3.5: SEM image showing the results of two dry etch processes on GaN material. The brighter wall on the left hand side has a sidewall angle of 76° while the darker wall on the right hand side has a sidewall angle of 45° . The line across the top of the SEM picture represents the surface profile

3.3 Devices fabricated for this work

Substrate emitting LEDs used in this work were formed by depositing 40 nm thick palladium as the ohmic contact to the *p*-GaN in the form of disks, with a variety of disk-diameters: with 500, 100, 50 and 30 μm . Circular transmission length measurements (c-TLM) patterns were used to measure the contact properties [17]. The inner contact has a radius of 25 μm and the outer disks have different radii of 30, 40, 70, 110, 140 and 200 μm . Palladium forms an ohmic contact as-deposited so no annealing was required [18]. The measured contact resistivity for the three epitaxial structures that we analysed in chapter 5 was $\sim 10^{-3} \Omega\cdot\text{cm}^2$ for all samples, while the sheet resistance of the *p*-GaN layer was 370 k Ω /sq, 430 k Ω /sq and 200 k Ω /sq for the 5QW, 10QW and commercial reference sample, respectively. Mesas of 520, 120, 70 and 50 μm diameter were formed by ICP etching using Cl_2 based chemistry. The etch depth extended about 800 nm into the *n*-doped GaN for the case of the 5QW and 10QW samples. Ti/Al/Ti/Au (20/170/5/250 nm) was deposited on the exposed *n*-doped GaN as a common (ohmic) *n*-contact; it was left non-alloyed. A schematic top and cross-sectional view of the samples is shown in figure 3.6.

It was also required to fully process and mount individual LED chips for the photovoltaic measurements shown in chapter 4. Figure 3.7 shows a schematic view of the fully processed top surface emitter LED device made with the same commercial material used before. This sample was patterned by dry etching using Cl_2 chemistry to expose the *n*-GaN layer. An *n*-type ohmic contact using Ti/Al/Ti/Au (20/170/5/200 nm) was deposited and annealed in an N_2 ambient at 750 $^\circ\text{C}$ for 5 minutes to obtain a contact resistance lower than $10^{-3} \Omega\cdot\text{cm}^2$. On top of the *p*-GaN 5 μm wide tracks of Ni/Au (5/5 nm) were deposited and annealed in air ambient at 500 $^\circ\text{C}$ for 1 minute resulting in a semi-transparent *p*-type contact. This metallization has a contact resistance lower than $10^{-2} \Omega\cdot\text{cm}^2$. No additional current spreading layers were used although Ti/W/Au bond pads were deposited to facilitate wire bonding to the package. Prior to the mounting the sapphire substrate was thinned and polished. Individual devices of 500 x 500 μm were diced and flip-chip mounted using stud bump bonding to a substrate

with patterned Au/Sn solder. Finally, devices were then placed in a ceramic package and wire bonded for electrical connection.

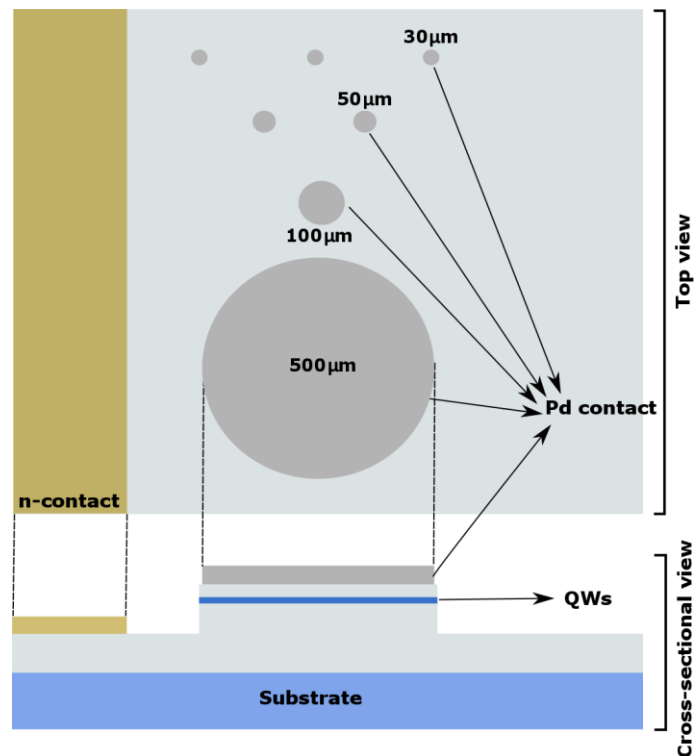


Figure 3.6: Schematic top and cross-sectional views of the contacts used in the quick evaluation run process. Contacts are made using 40nm of Pd without annealing and mesa etched to prevent current spreading.

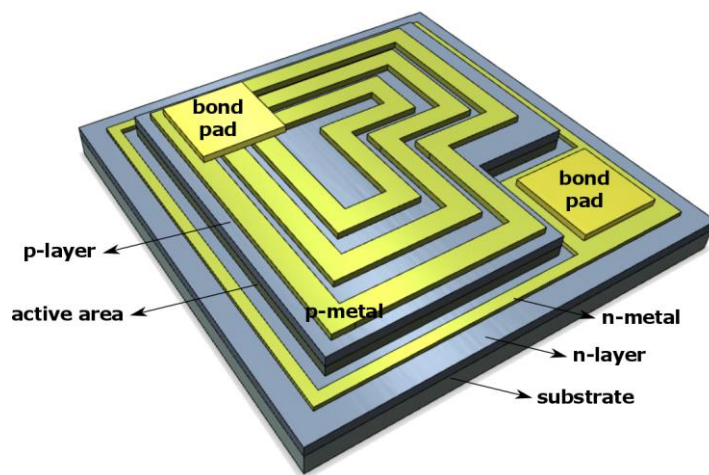


Figure 3.7: Schematic 3D view of the fully processed LED chip. The n-metal was formed using Ti/Al/Ti/Au and the p-metal tracks were formed using Ni/Au to obtain a semi-transparent contact. Bond pads were deposited to facilitate wire bonding

Chapter 4 – Electro-optical methods for the characterization of GaN-based LEDs.

Previous chapters serve as an introduction about GaN and LED devices and give an overview about the layer structure and fabrication of the LEDs characterized in this thesis. It is time now to take a closer look about the methodology that will be applied to perform the combined electrical and resonant optical characterization of the samples. This chapter starts with a discussion about the semiconductor physics under electrical excitation and the current-voltage characteristics of diodes. This is a fundamental part because it details the effect of the piezoelectric fields under electrical excitation that will be studied in the following chapter. The second section is about ideality factors and the information they can provide about recombination mechanisms in diodes. A brief section about the capacitance voltage characteristics of LEDs is given in the third part and includes a discussion about depletion capacitance, effects of the series resistance in the measurement of the capacitance and diffusion capacitance, which is traditionally neglected. The fourth part describes two methods that rely on optically resonant photoluminescence: the first one is fluorescence microscopy which is useful for spatial characterization and quick uniformity yield analysis. The second method is bias dependent photoluminescence that combines electrical and optical excitation and is helpful to study the role of photovoltaic effects in GaN LEDs. These effects provide important information about internal recombination processes in LEDs and are discussed in the final part of the chapter.

4.1 Electrical excitation and current-voltage (I-V) characteristics

The electrical characteristics of LEDs are investigated using the p - n junction theory developed by Shockley in 1949 [1]. When a p -doped and an n -doped semiconductor are joined together at thermal equilibrium and without external excitation the Fermi level must be constant through the entire p - n junction. When

the p - and n -doped semiconductors are brought into contact, initially carriers will diffuse across the interface: holes from the p -doped semiconductor diffuse into the n -doped semiconductor and electrons diffuse into the p -doped semiconductor. As holes leave the p -side, some of the negative acceptor ions are left uncompensated because they are fixed in the semiconductor lattice. A similar situation happens in the n -side where positive donor ions are uncompensated by the diffusion of electrons. A negative space charge region near the p -side and a positive charged region near the n -side is thus created. The total space charge region creates an electric field that is directed from the positive charge towards the negative charge. Figure 4.1 indicates on the top the direction of the electric field from the n -side to the p -side. In the space charge region carriers have diffused away, so this region is also called the depletion region. The total electrostatic potential difference between the depletion region in thermal equilibrium is called the built-in potential (V_{bi}). To illustrate all of this in the case of the studied LEDs, figure 4.1 shows simulated band diagrams for the 5QW sample without (black lines) and with applied bias (red lines). These and following band diagram simulations in this thesis were done with SiLENSE 5.8 Laser Edition software.

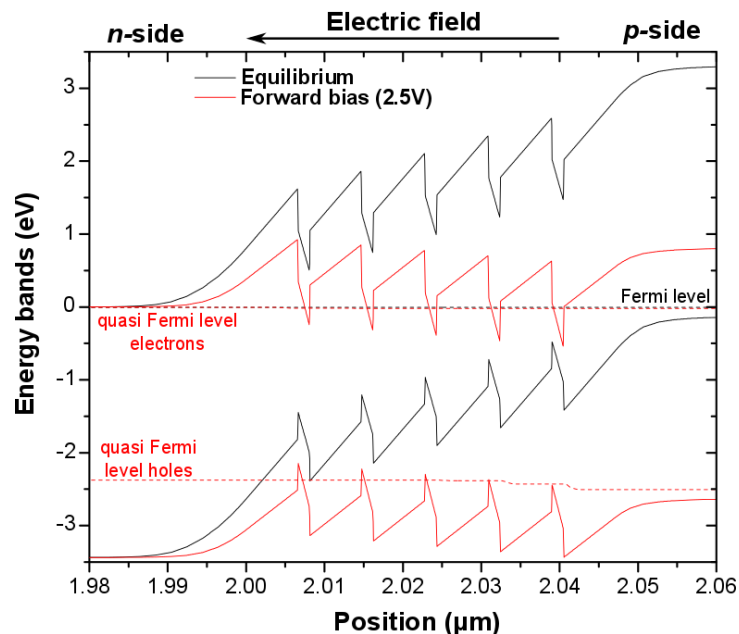


Figure 4.1: Simulated energy bands (continuous lines) and Fermi level (dotted black line) for the 5QW under thermal equilibrium without external excitation (black lines) and with an external forward bias of 2.5 V (red lines).

The triangular shape of the QWs is the result of the piezoelectric fields in GaN and has strong consequences in GaN LEDs: QWs from figure 4.1 show that the minimum and maximum for electron and holes are not in the same location. This leads to a spatial separation of electrons and holes resulting in a reduction in the wavefunction overlap. The result is an increase in the lifetime of the radiative recombination which reduces the overall efficiency of the device. Polarization fields also lead to a reduction in the available states at the bottom of the QWs for electrons or top of the QWs for holes because the quantum confinement forces the available levels upwards. This has an impact on the emission wavelength because electrons and holes are forced to be located on higher energy states in the QWs. On the other hand, the polarization field in the QWs points in the same direction as the external field, so under the influence of it carriers at the bottom of the QW will shift to lower energies (longer wavelengths) and this will further decrease the overlap between the wave-functions, this is called the quantum confined Stark effect [2]. Finally, there is also a screening of the internal field that happens under increments in the carrier density: carriers will progressively fill upper states and the recombination of these carriers leads to more energetic photons, which shifts the emission to shorter wavelengths.

The depletion region in a diode is highly resistive because it is depleted of free carriers. When an external bias voltage is applied to the p - n junction the voltage drop occurs mainly there. Under forward bias conditions, the applied voltage is opposite to the V_{bi} , so the barrier for the carriers to flow to the opposite side is reduced. Once the applied bias is of the order of V_{bi} carriers can flow freely through the junction to the opposite side to recombine. Now the E_F is not meaningful because the equilibrium situation is distorted so quasi-Fermi levels (QFL) E_{Fn} and E_{Fp} are defined to calculate the electron and hole concentrations in non-equilibrium states, respectively. These quasi Fermi levels help to visualize the majority and minority carrier concentrations under different applied bias levels. In figure 4.1 red lines are the simulated band diagrams for the 5QW sample under a forward bias of 2.5 V. Dotted red lines are the simulated QFL for both types of carriers.

In the electrical characterization, the current-voltage (IV) characteristics of the LED device is examined. This relationship is provided by the Shockley equation, which for small voltages [3] can be written as:

$$I = I_s e^{\left(\frac{qV}{n_{ideal}kT}\right)} \quad (4.1) [3]$$

where I_s is the saturation current, q is the electron charge, k is Boltzmann's constant, n_{ideal} is the ideality factor and T is the absolute temperature. The ideality factor of the diode relates to the recombination process that dominates the LED and will be discussed extensively in the next section of this chapter. An important deviation from the ideal IV characteristics to keep in mind is the existence of parasitic resistances in the diode. Figure 4.2-a shows the equivalent circuit of an LED with series and parallel resistances. A series resistance (R_s) adds a voltage drop to the measurements which makes the biased measured deviate from the bias across the p - n junction. Contribution to the series resistance may come from the contact resistance or the resistivity of the semiconductor layers. The parallel resistance (R_p) describes a path for the carriers to reach the opposite side without going through the junction; this could be due to any defects in the material or leakage paths along the semiconductor surface. If the parallel resistance is very low due to damaged regions the LED will not emit any light because the contact is shunted. The effects of both parasitic resistances are shown in figure 4.2-b alongside with the ideal IV characteristic. Parallel resistances increase the flow of current at low bias and the series resistance increases voltage drop at high bias. It should be noted that here these resistances are illustrated as linear resistances which may not be true in the case of a real diode where these resistance depend on several factors and may vary with applied bias.

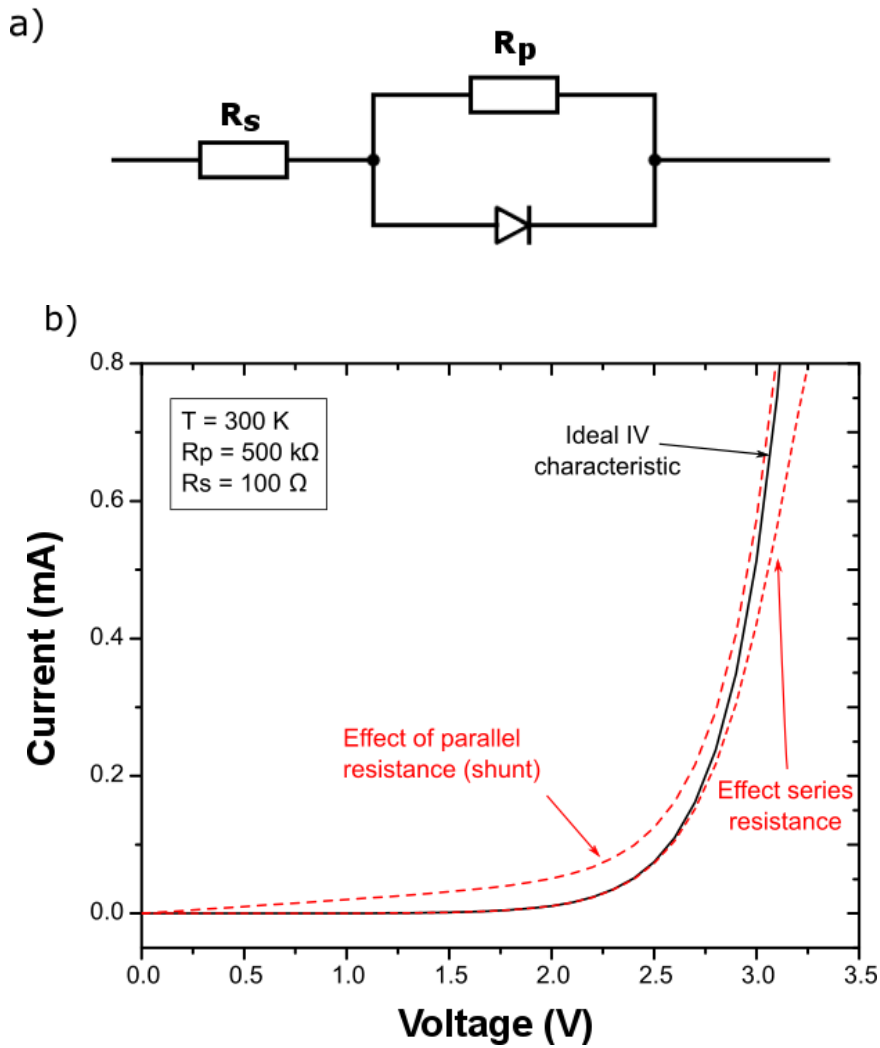


Figure 4.2: a) Equivalent circuit for a LED with parasitic resistances. b) Simulated I-V characteristics of an ideal diode (black line) and the effect of parallel and series resistance (red dotted lines). Resistance values used are $R_s = 100 \Omega$ and $R_p = 500 \text{ k}\Omega$.

The electrical characteristics in this work were measured on a system consisting of a probe station equipped with an electrical source and a photodetector to capture at the same time relative luminescence, current and voltage (LIV measurement). A diagram of this set up is shown in figure 4.3. The electrical source here is a Keithley 2400 source-meter and below the sample there is a Newport 818-UV photodetector connected to a Keithley 2625 source-meter with a resolution in the pico-amps range. Both devices are controlled by a custom LabVIEW code developed at Tyndall.

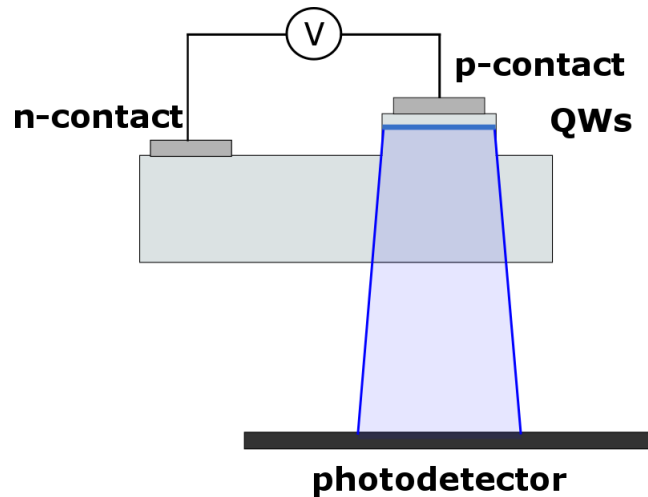


Figure 4.3: Set up for electrical characterization of samples. The electrical source biases the selected device and the photodetector below the sample collects a portion of the light emitted from the probed contact.

4.2 Ideality factors and estimation of current components

Identification of all underlying processes in GaN LEDs is a very difficult task to perform because at each step there are several mechanisms competing with each other. Special care is required especially when measuring non-commercial and non-optimized samples due to the large fluctuation in the properties between samples and non-uniformity across the wafers. For state-of-the-art samples with high efficiency this identification becomes easier because these LEDs resemble more closely an ideal diode so the mathematical model for p - n junctions gives more accurate results.

Insights in the different internal processes are given through their different ideality factors and allow the possibility of building an equivalent circuit of the diode using each current component identified by its ideality factor as in (4.1). The sum of all these current components should be the total current going through the device. Kang and Kim [4] developed an equivalent circuit that illustrates this and is shown in figure 4.4.

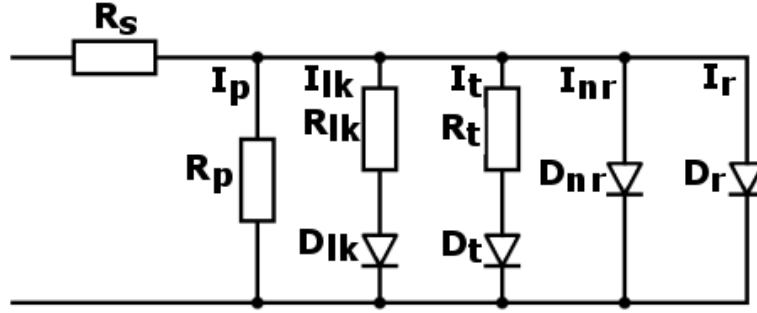


Figure 4.4: Equivalent circuit with several diodes identified by the ideality factor of the recombination. Model includes resistive leakage I_p , non-linear leakage I_{lk} , tunnelling current I_t , non-radiative recombination current I_{nr} and radiative recombination current I_r . A series resistance R_s is also included [4].

The total current (J_T) here is given by: $J_T = J_r + J_{nr} + J_t + J_{lk} + J_p$ and each current component is represented by a diode with its own ideality factor. Starting from the right hand side, the current component from the radiative recombination (I_r) is represented by a diode D_r with an ideality factor n_{light} that can be calculated from the slope of the luminescence versus voltage (L-V) characteristics of the diode. This comes from the fact that under equilibrium, in a semiconductor the concentration of holes (p) and electrons (n) are related by:

$$np = n_i^2 \quad (4.2) [5]$$

Where n_i is the intrinsic carrier concentration. The non-equilibrium version under an applied bias V of previous equation (4.2) can be found in [5] and is:

$$np = n_i^2 e^{(qV/kT)} \quad (4.3) [5]$$

On the other hand, the light output (L) from the LED can be approximated by:

$$L = Bnp \quad (4.4) [3]$$

where B is the radiative recombination coefficient. Combining both equations (4.3) and (4.4) the relationship between L and V can be written as:

$$L = Bnp = Bn_i^2 e^{(qV/kT)} \quad (4.5)$$

Equation (4.5) relates L and V for an ideal diode and for the case where all the applied voltage is dropped across the junction. Adding the effect of a series resistance and using the ideality factor n_{light} that represents the diode D_r equation (4.5) yields:

$$L = Bnp = Bn_t^2 e^{\left(\frac{q(V-IR_s)}{n_{\text{light}}kT}\right)} \quad (4.6)$$

The second diode D_{nr} corresponds to the Shockley-Read-Hall (SRH) non-radiative current I_{nr} which is due to defects in the layer stack. R_p represents a resistive current leakage term that could be the result of effects as charge-limited bulk current [6] or leakage along the LED chip surface [7]. In some cases a current dependent series resistance needs to be taken into account. This is done here by the non-linear term represented by the resistor-diode series connection R_{lk} and D_{lk} which assures that the leakage will saturate. A current component due to tunnelling is represented here by a resistor-diode series connection R_t and D_t . Although not shown here, more than one tunnelling component may have to be considered in the analysis. At a given temperature, each carrier entity (electrons, light holes, heavy holes) has associated a characteristic energy (E_T) that represents the tunnelling transparency of the energy barrier at the junction interface [8]. Using E_T , the tunnelling current (I_t) can be expressed by:

$$I_t = I_s e^{\frac{qV}{E_T}} \quad (4.7) [8]$$

Comparing equations (4.7) and (4.1) results in $n_t kT = E_T$ and the ideality factor that represents the tunnelling current can be now calculated. Because E_T is different at a given temperature for each carrier entity, several contributions due to tunnelling can be determined. This will result in an expansion of the circuit from figure 4.4 with more resistor-diode connections to take in account the contribution of tunnelling for each kind of carrier.

In practice, building the full equivalent circuit for our samples is a complex task because the unambiguous identification of each process is rather difficult. In chapter 5 there is a study of ideality factors calculated by different experiments and the information that can be extracted from them about carrier dynamics.

4.3 Capacitance-Voltage (C-V) measurements

Alternate current (AC) characteristics of the depletion region of LEDs have been studied as a convenient non-destructive method to determine the doping profile of the device. In general, any variation of the charge within the p - n junction with applied bias leads to a capacitance. The total junction capacitance (C_j) includes capacitance due to opposite charges of dopants (depletion capacitance, C_{depl}) and capacitance due to thermal diffusion of minority carriers (diffusion capacitance, C_{diff}). C-V measurements are commonly done only at reverse bias when there is no diffusion of carriers, so C_j equals C_{depl} [3]. In this case C_{depl} can be used to calculate the doping profile of the junction. The AC characteristics of LEDs under forward bias are seldom investigated because in this case C_j is the sum of C_{depl} and C_{diff} which is difficult to interpret because, as will be explained in the second part of this section, traditional Shockley's semiconductor theory is in conflict with the results and a revision of the theory is required.

4.3.1 Depletion capacitance

A LED structure consists of an intrinsic (semi-insulating) junction region sandwiched between a p -doped and n -doped region. This is a similar situation to a capacitor with charges of opposite sign on the plates and an insulator material between them. This allows use of the same definition for the capacitance in both cases, the depletion capacitance (C_{depl}) for LEDs is then defined as:

$$C_{depl} = \frac{dQ}{dV} = \frac{\epsilon_s A}{W} \quad (4.8) [9]$$

Where Q is the charge, ϵ_s is the semiconductor permittivity, A is the area of the measured contact and W is the width of the depletion region. The difference with the capacitor is that W and C_{depl} are dependent on the applied voltage. The similarities with the parallel plate case holds because for this situation charge is only added at the edge of the depletion region. C-V measurements can then be used to calculate the relationship between W and the doping profile (N) using the following expression:

$$N = \left(\frac{-2}{\epsilon_s A^2 q} \right) \left(\frac{dV}{d \left(\frac{1}{C_{depl}^2} \right)} \right) \quad (4.9) [9]$$

There are however several parameters that affect strongly the capacity to obtain accurate doping profiles and can lead to misleading results:

- The dependence of the doping profile on the area squared in (4.9) requires to know this parameter precisely. The squared dependence makes small errors in the measurement of this parameter have a strong impact on the result.
- The Debye Length (L_D) given by (4.10)[3] is the distance over which a charge imbalance is neutralized by majority carriers under equilibrium conditions. In other words, L_D gives an idea of the limit of the potential change in response to an abrupt change in the doping profile. As a result, if the doping profile changes abruptly on a scale less than L_D , this variation has no effect and cannot be resolved. For measuring purposes, this implies that for LEDs where the thickness of QBs between QWs is of the same order as L_D , it is not possible to resolve individual QWs. For doping concentrations of $\sim 10^{18} \text{ cm}^{-3}$, L_D is in the order of 5-6 nm.

$$L_D \equiv \sqrt{\frac{\epsilon_s kT}{q^2 N}} \quad (4.10) [3]$$

- Large series resistance [9] in devices being characterized has to be taken in account. C-V measurements are performed by applying a small AC voltage on top of the main continuous bias and monitoring the imaginary component of the resulting AC current. In the absence of series resistance in the equivalent circuit of the diode this component is directly proportional to the depletion-layer capacitance. Yet, in the presence of series resistance the measured capacitance obtained from the experiment can be expressed as:

$$C_{depl}' = \frac{C_{depl}}{1 + \omega^2 R_s^2 C_{depl}^2} \quad (4.11) [9]$$

Where ω is the angular frequency used for the measurement and R_s is again the series resistance of the diode. It is clear that in the ideal case when R_s is 0 then $C_{depl}' = C_{depl}$.

It is possible to get an accurate measurement of the area of the emission with careful measurements of the contact area. On the other hand, the L_D gives a physical limit that cannot be avoided. For the series resistance, the easiest solution to implement is to measure the phase angle φ between the applied AC voltage and the resulting AC current through the diode. In terms of φ the relationship between the actual capacitance and the measured capacitance is:

$$C_{depl}' = C_{depl} \sin^2 \varphi \quad (4.12) [9]$$

Applying now this definition of the real capacitance to get the corrected values of the depletion width, the equation using only measured values will now be:

$$W = \frac{\varepsilon_s A}{C_{depl}'} \sin^2 \varphi \quad (4.13) [9]$$

The concentration charge can be calculated now remembering that both C_{depl}' and φ are functions of the voltage, so to get the actual charge concentration the expression to use is:

$$N_D = -(q\varepsilon_s A^2)^{-1} C_{depl}'^3 \left[\sin^4 \varphi \left(\frac{dC_{depl}'}{dV} - 2C_{depl}' \cot \varphi \frac{d\varphi}{dV} \right) \right]^{-1} \quad (4.14) [9]$$

Finally, additional information that can be collected from CV measurements in reverse bias is related to the existence of additional interlayers in the LED structure: when two semiconductors with different bandgaps are joined, the conduction and valence bands cannot be joined together without an abrupt change so the electrical technique based on CV measurements can easily determine band offsets on $n-n$ or $p-p$ isotype heterojunctions where one of the semiconductors has a narrower bandgap, or a different doping concentration. C-V measurements of these heterostructures will yield an apparent or effective carrier concentration different from the expected, or in other words; additional peaks in the N_D-V or N_D-W plots will appear in positions belonging to interfaces between layers.

4.3.2 Diffusion capacitance and negative capacitance

As introduced before, C_j has two components, one is the already discussed capacitance C_{depl} and the second one is the diffusion capacitance. C_{diff} is the result of minority carrier transport through the junction under forward bias. This change of the charge in transit divided by the voltage gives us the diffusion capacitance. Using Shockley's $p-n$ junction theory this diffusion capacitance is given by:

$$C_{diff} = \frac{dQ}{dV} = \frac{Aq^2 L_p p_{n0}}{kT} e^{qV/kT} \quad (4.15) [3]$$

Where L_p and p_{n0} are the diffusion length of holes and the concentration of holes on the n-side in equilibrium. Equation (4.15) implies that at forward bias the total capacitance will only increase with the applied forward bias. However; as the measurement of the C-V characteristics of a high efficiency commercial packaged device shows in figure 4.5, in a real device there is a maximum point around the threshold voltage (here around 2.45 V) and then the capacitance decreases reaching negative values. This negative capacitance was predicted as a result of the recombination in a LED in a publication by Laux and Hess [10] where the authors published a revision of the analytic theory of $p-n$ junction impedance including all the contributions to the diode current described by a rather complex equivalent circuit.

All C-V characteristics shown in this work were measured using a Cascade Microtech SourceOne probe station. This probe station allows us to make electrical connections with small probes connected to two micropositioners. Both AC and DC signals were provided by an Agilent C1500a semiconductor device analyser with proprietary software which outputs directly the variables chosen by the user. For the C-V measurements, the parameters measured were capacitance and parallel resistance. In addition, impedance and phase angle were also measured to make series resistance corrections when needed.

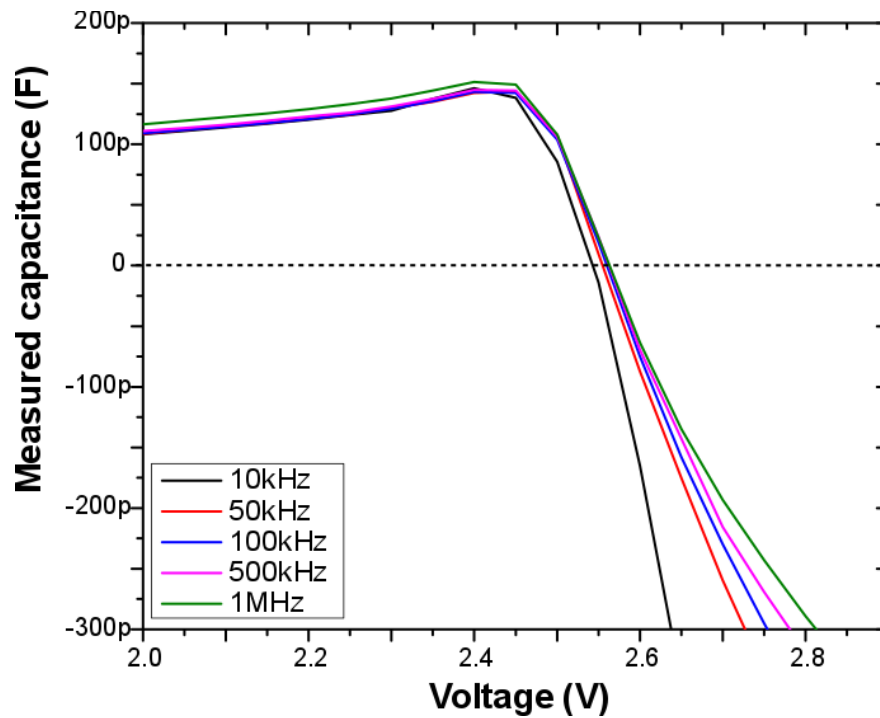


Figure 4.5: Example of a CV measurement in a packaged blue GaN LED commercial device. After threshold (~ 2.45 V) the capacitance decreases to negative values. The decrease in measured capacitance is more abrupt at lower measurement frequencies.

A quick analysis of how carriers can be reclaimed helps to understand the origin of the negative capacitance. Under forward bias the superimposed AC signal will drive carriers into the junction in the part of the cycle when the signal has the same direction as the DC bias. When the applied AC signal is in the opposite direction some of the injected carriers can be reclaimed. If these reclaimed carriers are in phase with the AC signal the sample behaves as a linear resistor. If these carriers arrive 90 degrees out of phase with the signal, this is the measure of the capacitive behaviour of the sample. Finally, if the injected carriers recombine, they cannot be reclaimed and as shown in [11], this recombination current displays an inductance effect, which is what causes the negative capacitance when measuring LEDs.

4.4 Optical resonant photoluminescence

Optical resonant photoluminescence (ORPL) relies on the same principle as traditional PL where light is used as an excitation source. When a semiconductor is illuminated using light with a wavelength higher than the bandgap a portion of the light is absorbed and electron-hole pairs are generated. After this excitation, several relaxation processes may occur that result in the emission of photons. The study of luminescence properties in GaN is a powerful method to study the quality of the material [12-14].

ORPL is slightly different from traditional PL because it requires selecting the excitation wavelength to be only absorbed in the QWs. For the samples in this work, the addition of 23% of indium to GaN reduces the bandgap of the QWs from 3.41 eV (364 nm) to around 2.63 eV (470 nm) at room temperature. To achieve ORPL then it is required to select a wavelength higher than the bandgap of the QWs and at the same time lower than the bandgap of GaN.

4.4.1 Fluorescence microscopy

In fluorescence microscopy (FM) a high intensity white lamp is used as the excitation source. Here, the emission from a mercury arc lamp is filtered using a 390nm-420nm bandpass filter and incident on the LED material through the transparent sapphire substrate. Light emitted from the sample is filtered with a short wavelength cut-off of 450nm and received light is imaged onto a CCD camera. A schematic view of the fluorescence microscope used in this work, a Zeiss Axioskop 2, is shown in figure 4.6.

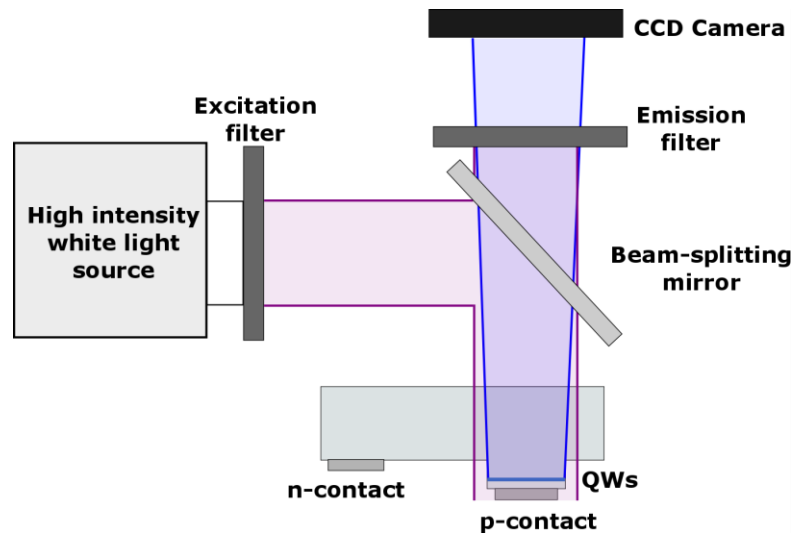


Figure 4.6: Schematic diagram of a fluorescence microscope.

Fluorescence microscopy is a handy technique to check for spatial variations in samples before and after processing. Figure 4.7 illustrates this point using a commercial green wafer with emission peak around 530 nm. The unprocessed sample (Figure 4.7-a) shows a characteristic pattern consisting of bright and dark areas in wave-like patterns. Such general structuring of the emission is quite common for wafers from many different suppliers though the details are different. Analysis of the spatial variation of the samples is important because strong lateral variations in the emission due to the materials or the processing suggests that the traditional 1 dimensional analyses of carrier transport need to be treated with caution [14]. Figure 4.7 -b shows an optical image of the sample after patterning using a dry etch with BCl_3 chemistry. In this case the mask had arrays of squared and circular mesas of different dimensions. Figure 4.7-c shows the same area as in 4.7-b under fluorescence microscopy. In the larger square contacts the same spatial variation as in 4.7-a can be seen with brighter and darker areas. The increased emission on the edges of the mesas is due to light refraction from the mesa side walls. On the right hand side of the figure 4.7-c there is an array of circular mesas with 15 μm diameter. The brighter contacts on the top 2 rows are due the light coming from the squared mesas above them. On the other hand, there is a difference on the emission of the contacts at the bottom edge of the picture that is the result of the spatial variation of the sample. Figure

4.7-d shows a close-up of these contacts where differences in the emission can be seen clearly. This has a strong impact on the yield of the fabrication process. As will be shown in chapter 5, differences in the emission between contacts are related with different electrical performance of each device. In summary, the lack of uniformity in the wafer leads to differences in the optical and electrical performance of the final devices.

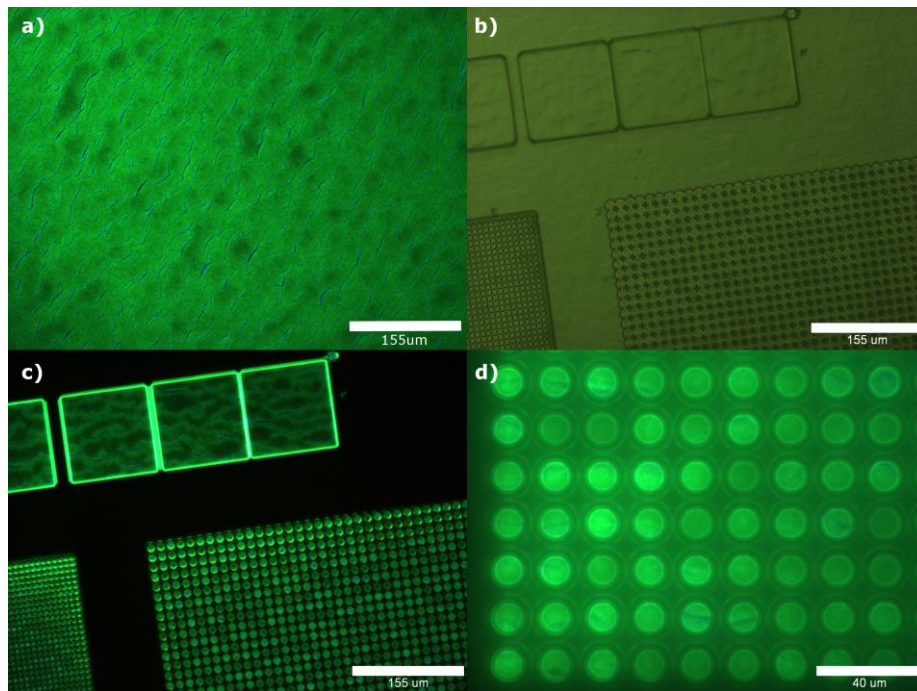


Figure 4.7: a) Fluorescence image of the spatial variation in a commercial green sample (~530nm) before processing. b) Optical image of the same sample after patterning with small squared and circular contacts. c) Fluorescence image of the same areas as in b). d) Close-up of the circular contacts on the right hand side of c). Selected wavelength for excitation cut-off was 400nm.

4.4.2 Bias dependence photoluminescence

The current set up for fluorescence microscopy does not allow electrical bias connections except in the case of fully packaged samples. Combining electrical and optical resonant excitation is interesting for GaN LEDs because it allows the

study of the photovoltaic characteristics. The use of photovoltaic measurements on LEDs together with bias-dependent spectrally resolved luminescence is a powerful method to provide useful insights into the carrier dynamics inside GaN LEDs, as will be shown in chapter 5. Therefore, a new set up, shown schematically in figure 4.8 was required for our non-packaged samples.

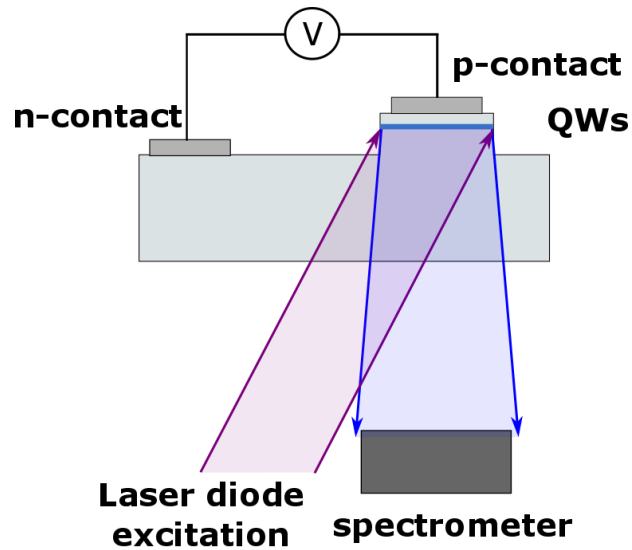


Figure 4.8: Schematic view of the optical resonant excitation set up for bias-dependent PL. The laser is directed at approximately 30° to the surface normal through the polished substrate and excites only the QWs. A spectrometer collects light emitted perpendicular to the device.

The sample under study is placed on a stage which allows the excitation light to come from the bottom requiring the sample to be back-polished. In this particular case the excitation source selected is a laser diode emitting at 405 nm (nominal) with a maximum power of 20 mW. This laser is directed at approximately 30° to the surface normal through the polished substrate. Collection of the emission spectra is achieved by placing an OceanOptics 220 spectrometer under the sample. Alternatively, a CCD camera can be used to image the emission and capture the near field emission. The electrical excitation is provided by a Keithley 2400 source meter controlled through the computer by a custom LabView program developed at Tyndall. In this case there is no filtering between the

sample and the spectrometer so some of the excitation light reflected from the sample will be collected in this experiment. This should not be a problem here because the laser diode shows a very narrow peak at a wavelength of 405 nm, therefore identification of the excitation wavelength is straightforward.

4.5 Photovoltaic effects on LEDs

In traditional PL measurements it is often incorrectly assumed that carrier transport can be neglected due to the strong confinement potential of the wells. In the case of InGaN-based QWs, the existence of a large inbuilt piezoelectric field separates the electron and hole wave-functions lengthening the radiative recombination time which allows for significant carrier escape to occur. In electrically biased p - n LED structures this carrier escape can be measured as in a photovoltaic cell [14]. As a result, when a MQW LED structure is excited in an open-circuit (OC) condition, the electrons and holes re-distribute across the QWs, escape out of the QW region and are driven to the n - and p - sides of the junction, respectively, by the built-in voltage where they accumulate creating a forward bias across the LED junction as a photovoltage, V_P . This photovoltage is dependent on the incident light level, the number and bandgap of the QWs, radiative and non-radiative recombination and on leakage paths. This V_P opposes V_{bi} , forward biasing the p - n junction as in the case of electrical excitation.

Figure 4.9 shows the calculated band diagram of a representative $\text{In}_{0.23}\text{Ga}_{0.77}\text{N}$ QW LED, with 3 QWs, each 1.8 nm thick, with polar crystal orientation under short circuit (SC) and at 2.5 V forward bias conditions [15]. Under the short circuit conditions depicted in figure 4.9-a, the p - and n -metal pads are connected so electrons and holes that escape from the QWs and result in a flow of carriers that can be measured as an external photocurrent. Due to the reduced number of carriers in the QW region the light emission will be lower than in the biased condition. In OC conditions and with high excitation levels V_P will approach V_{bi} creating flat band conditions as shown in figure 4.9-b. The driving force responsible for setting up V_P is then compensated by carrier injection back into the QWs and a dynamic equilibrium is established.

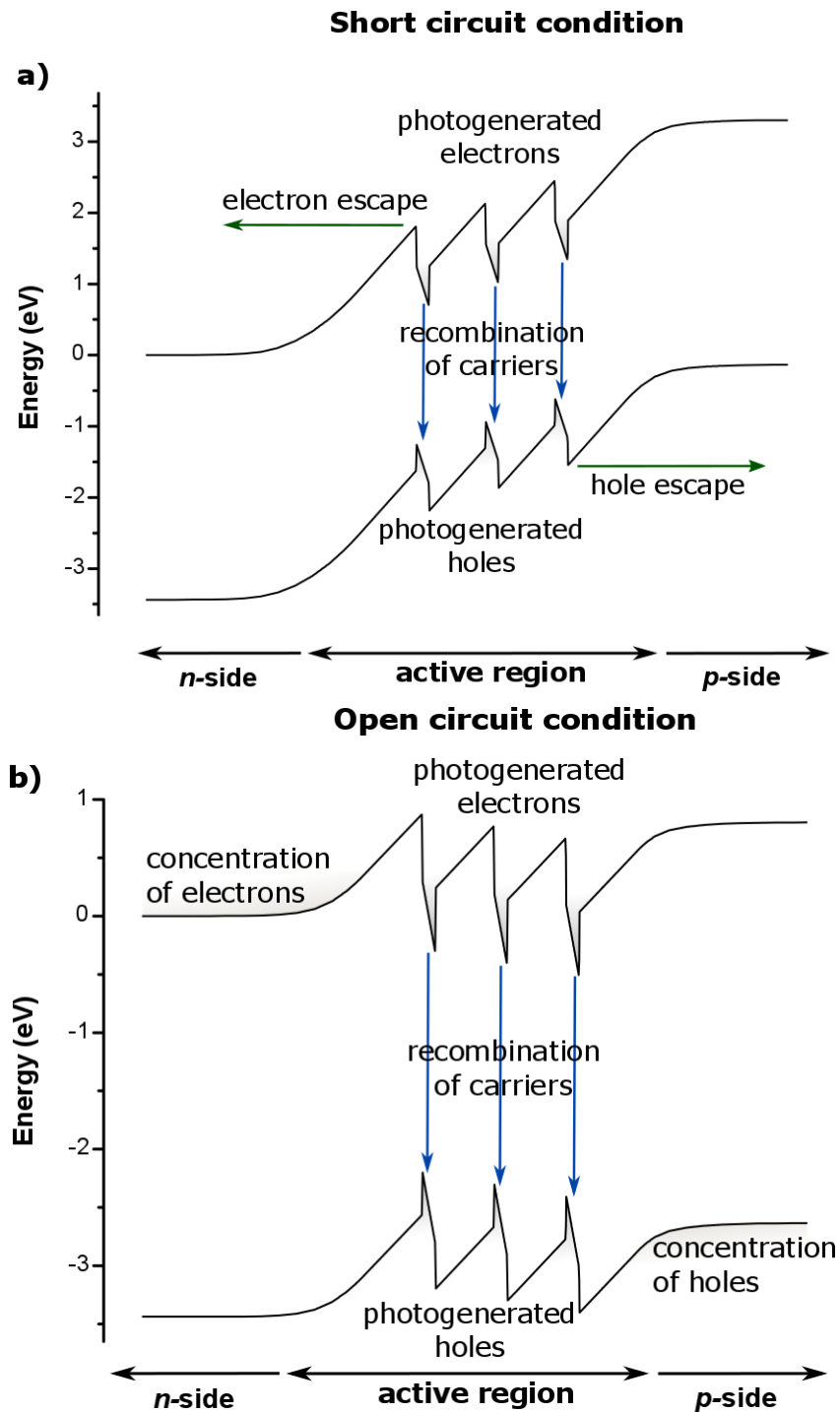


Figure 4.9: Calculated energy band diagram for a 3QW $\text{In}_{0.23}\text{Ga}_{0.77}\text{N}/\text{GaN}$ structure under (a) SC conditions: A significant amount of the photogenerated carriers escape and are collected as a negative photocurrent resulting in weak radiative recombination. (b) OC conditions: the escaped carriers accumulate on each side of the junction and generate a forward voltage. Carrier escape is then reduced resulting in enhanced recombination, due to a higher carrier density in the QWs.

To illustrate the differences in the light emission characteristics under OC and SC conditions under ORPL, the fully processed LED from the commercial wafer, mounted in a ceramic package as described in chapter 3, is now used. This device is connected to a Keithley 2400 for the electrical source and the optical excitation is provided by the fluorescence microscope. The selected wavelength cut off for the excitation is 400 nm and the incident power is around 2 mW/cm². Resultant images are shown in figure 4.10: under OC conditions, (figure 4.10-a) carrier escape is reduced by V_P forward biasing the junction and the number of carriers available for radiative recombination inside the QWs is increased, therefore more light is emitted. The high open circuit voltage (V_{oc}) of 2.4 V measured is due to the high incident light intensity and minimal non-radiative recombination paths. Under SC conditions (figure 4.10-b) only a small fraction of carriers recombines and contributes to the light emission. These escaping carriers were measured as a short circuit photocurrent of 160 μ A or 100 mA/cm² when normalized to the diode area.

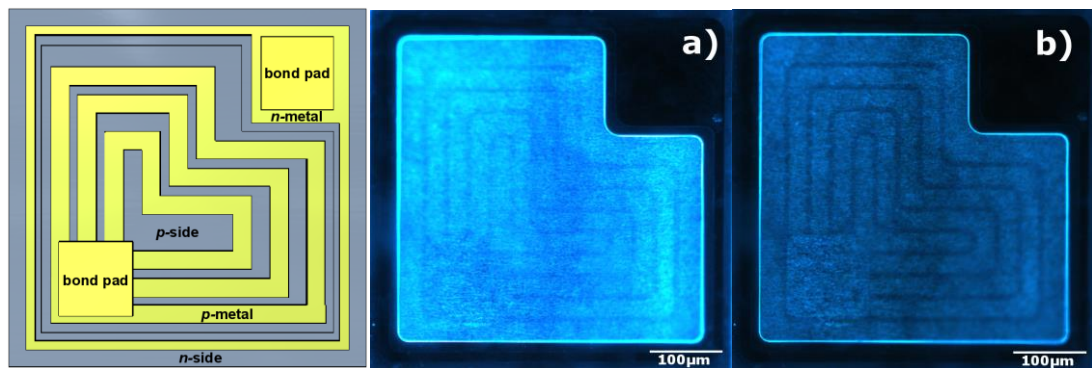


Figure 4.10: Fluorescence microscopy images of a mounted LED taken through the transparent sapphire substrate under (a) OC conditions and (b) SC conditions under optical excitation of ~ 2 W/cm².

Both images in 4.10-a and -b show a lower luminescent intensity from under the Ni/Au contact tracks as compared to the un-contacted areas. Under SC condition, the holes escaping from the QWs are more efficiently collected from under the Ni/Au contact because the vertical resistance is low whereas in the un-contacted

areas, due to the high lateral resistance of the p -side, some holes accumulate and generate a small photovoltage to forward bias the p - n junction, reducing carrier escape and enhancing light emission locally. Under SC conditions the bond pad region (barely visible at the bottom left part of the images in Fig 4.10-b) is slightly brighter than the Ni/Au metal tracks. The reason is that the Ti/W/Au bond pad is slightly more reflective than the GaN-air interface. This results in the increased absorption and consequently stronger re-emission due to the double pass of the light through the QWs.

The reduced intensity under the Ni/Au contact tracks under OC conditions is due to the voltage under the Ni/Au being slightly reduced compared with the unmetallized region. To confirm that, fluorescence images from the LED under joint optical and electrical excitation were measured. The Ni/Au contact areas are set at supply voltages of 2.4 V, 2.5 V and 2.6 V respectively. Figure 4.11-a was taken with the voltage set at 2.4 V, which was the same value as the previously measured V_{oc} . The resultant image is very similar to figure 4.10-a under optical excitation alone. With the forward bias set at 2.5 V figure 4.11-b is taken and there is no contrast between areas with or without metal which suggests that the whole surface is at the same potential, one of them generated by electrical excitation and the other one generated by optical excitation. Thus under optical excitation alone there is a difference of 100 mV between the photo-induced voltage off and on the Ni/Au tracks. Possible reasons may be that the voltage is shared across the metallized region or that the annealed Ni/Au contact has a lower reflection than the surrounding material with lower local absorption or that the annealing process induces some small damage in the p -doped surface region. Figure 4.11-c shows the image when the device is forward biased with 2.6 V. In this case, the emission is brighter under the metal tracks because now the voltage of the contacted areas is larger than in the un-contacted area in contrast to figure 4.11-a. It is evident that the voltage is not constant across the surface and there is low lateral current spreading due to the large lateral resistance as the sheet resistance of the p -layer is higher than 50 k Ω per square. The second row of figure 4.11 shows a detail of the grid at higher magnification under the same conditions as in the top row.

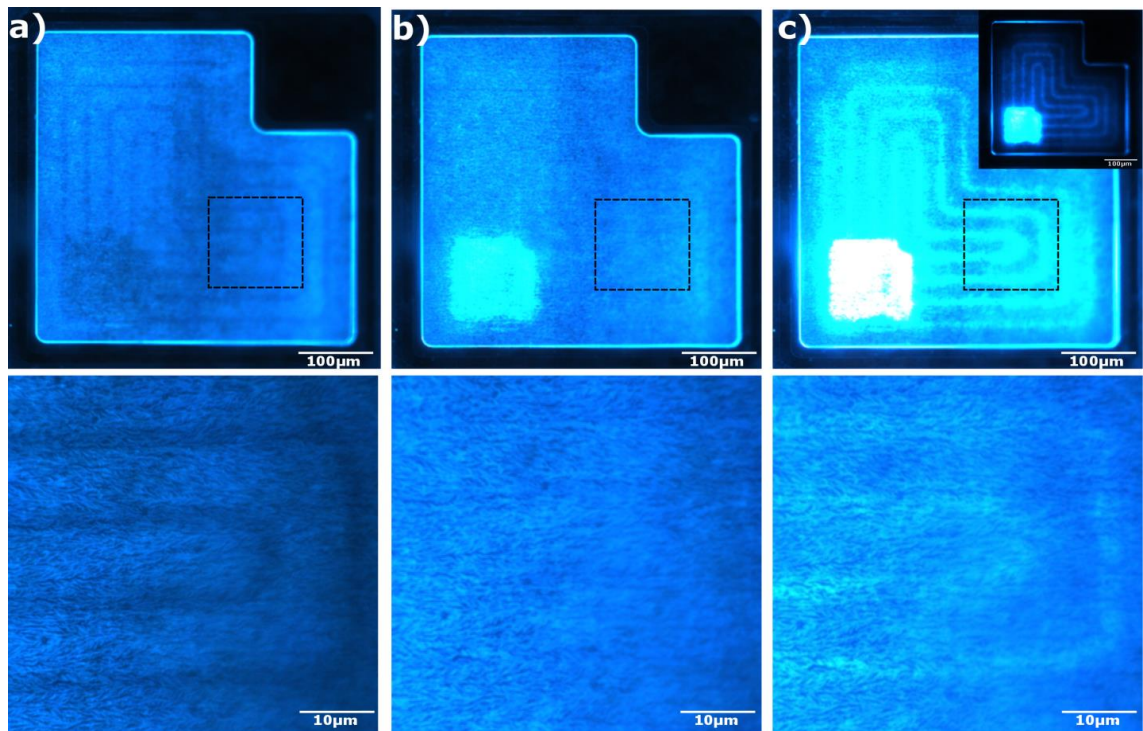


Figure 4.11: (Top) FM image under optical excitation combined with electrical excitation with a) 2.4V; b) 2.5V; and c) 2.6V. The inset on c) shows the same device under electrical excitation alone with a bias of 2.5V. (Bottom) Detail of the grid at higher magnification.

I-V characteristics with and without optical excitation are shown in figure 4.12-a. The current increases with reverse bias due to collection of the remaining carriers causing the reduced luminescence in Fig 4.10-b. At -3 V the FM image becomes dark as shown in figure 4.12-b suggesting that all carriers generated in the QWs are being collected as photocurrent.

There is also an increasing absorption in the QWs associated with the flattening of the bands under reverse bias. Nevertheless, the majority of the carriers generated are escaping from the wells under SC conditions (160 μA from a total of 210 μA) and that amount is limited primarily by the lateral resistance of the *p*-type layer. When considering the device as a photovoltaic cell the fill factor is low due to the large sheet resistance and small contact area. This could be increased by the use of an Ag based planar contact which would also improve V_{oc} further through increased absorption by the reflection.

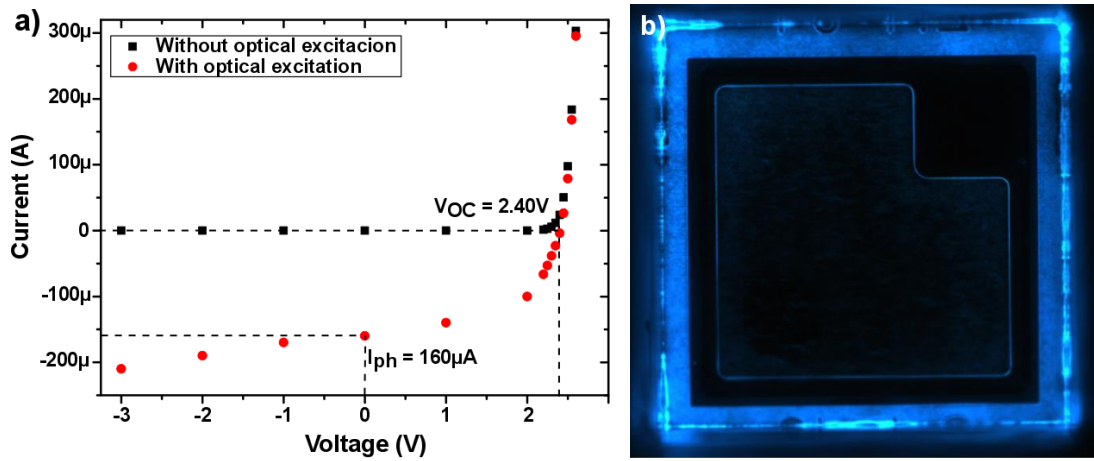


Figure 4.12: a) IV curve from the mounted LED under electrical excitation (black points) and under combined optical and electrical excitations (red points). The measured short circuit photocurrent (I_{ph}) was $160 \mu A$ and the open circuit voltage (V_{oc}) was $2.40 V$. b) Fluorescence image under $-3 V$, the sample turns black suggesting almost complete removal of carriers.

Chapter 5 – Combined electrical and resonant optical excitation characterization of MQW GaN-based LEDs

In this chapter a comprehensive experimental study of the emission spectra and electrical characteristics of the three samples described in chapter 3 under resonant optical pumping and varying electrical bias is presented. This methodology is the result of the search for an explanation of two different observations on the 5QW and 10QW samples:

- Low turn on voltage: initial LIV measurements on these samples showed a turn-on voltage of around 2.2 V, which is around 400 mV lower than the bandgap for an emission wavelength of 470 nm (~ 2.6 eV).
- Yellow band emission: these two samples show yellow emission, under electrical excitation and also under resonant optical excitation (fluorescence microscopy in this case)

Because at that time it was not possible to find a satisfactory explanation, several experiments were performed to gain insight in the performance of these samples: to fully understand carrier dynamics under optical resonant excitation, fluorescence microscopy was applied to a fully packaged device from the reference commercial wafer connected to an electrical source. This study allowed us to understand the effect of carrier escape, to study the spatial variation and the role of metal contacts in fluorescence microscopy. This is shown in the first section of this chapter and also provides a way to perform a quick evaluation of the electrical performance of contacts using fluorescence microscopy: as it will be shown, dimmer contacts show increased leakage current at low bias.

Resonant optical excitation was showing interesting results yet the current fluorescence set up cannot be used to apply electrical bias to samples that are not packaged. A new experimental set up was required to do a similar study on the 5QW and 10QW samples, which could not be packaged, because these devices did not have individual n -contacts. Once the experimental set up for the bias dependent PL was in place it was possible to study the photoresponse of these

samples. The first result of using resonant optical excitation in combination with variable electrical bias applied showed strong differences in the extracted photocurrent between 0 and 2 V for the 5QW and the 10QW samples: while the former shows better carrier confinement, the latter resembles more closely a photovoltaic cell with poor fill factor.

This information led us to study the differences in the piezoelectric fields between the two samples due to the differences in the number of QWs and QBs thickness, and the effect of these on the carrier dynamics under both electrical and resonant optical excitation. The conclusion was that an LED with a thin well and a thick barrier shows strong bias-dependent properties in the emission spectra, poor photovoltaic carrier escape under forward bias and an increase in the effective resistance when compared to the other sample with thinner barriers. The reason behind these differences is the relative increase in the piezoelectric field in the well and associated reduced field in the thicker barrier. This is shown in the second part of this chapter and is first main novel aspect of this thesis.

The second main novel aspect is the analysis of the voltage ideality factors calculated using bias current vs. voltage, EL intensity vs. voltage, photovoltaic short-circuit current vs. open circuit voltage, and PL intensity vs. open circuit voltages. These results are presented and discussed in the third part of this chapter and provide clear insights into the carrier dynamics in these samples because the last two methods avoid effects from outside the QW region.

Finally, some work was done related to the doping profiling of these samples using C-V measurements at different frequencies and the study of the diffusion capacitance was began and is summarized in the fourth part of this chapter. The fifth part of this chapter contains a methodology to estimate the IQE using measured EQE curves by electrical characterization and the chapter finishes with a summary of all the results.

5.1 Fluorescence microscopy: observation of spatial variations and the effect of metal contacts

The spatial distributions of the emission from the LED structures were characterized using uniform excitation with the fluorescence microscope set up described in chapter 4. The excitation source is filtered using a 390nm-420nm bandpass filter and incident on the LED material through the transparent, polished sapphire substrate. This selected wavelength band generates carriers only inside the 475 nm emitting QWs as the bandgap of GaN corresponds to a wavelength of 360 nm. The luminescence from the sample is filtered with a short wavelength cut-off filter with a cut-off wavelength of 450 nm and imaged onto a CCD camera. Figures 5.1-a, -b and -c show the fluorescence images from the 5QW, 10QW and commercial samples respectively. A strong spatial variation in the emission is observed with a characteristic wave-like pattern at tens of microns scale for the 5QW/10QW samples. This emission pattern of bright spots and patches from QWs grown by the quasi-two-temperature (Q2T) method has also been reported previously and studied by cathodo-luminescence mapping on similar material [1], where it was established that this profile originates from the growth of the template.

The emission wavelength from the samples also seems to be different; although the peak wavelength of the emission under electrical excitation (EL) does not vary by more than 12 nm across all the samples as it will be shown later (see figure 5.7 for example). The 10QW (Figure 5.1-b) sample appears to emit at longer wavelengths (green) than the 5QW due to a yellow band emission that is detected under electrical and optical excitations and will be discussed later. The combination of both blue and yellow wavelengths is detected as green through the CCD Camera under low optical excitation densities ($\sim 20 \text{ mW/cm}^2$) when the amount of light from both emissions is comparable. Differences in the emission with the commercial sample are due to the higher intensity of the emission from this sample which is converted to a lighter blue colour by the CCD camera.

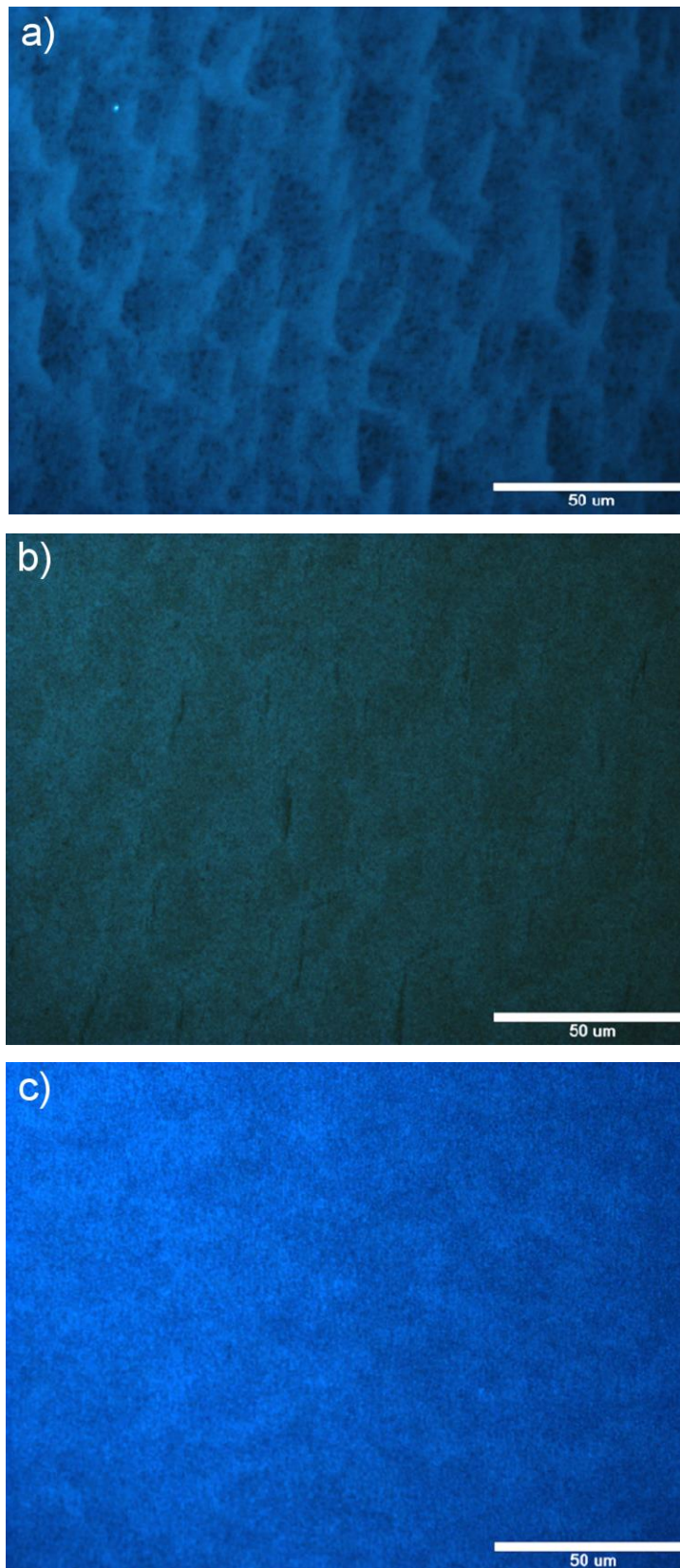


Figure 5.1: Fluorescence microscopy images of a) 5QW sample, b) 10QW sample and c) commercial sample. All images were taken through the polished substrate under the same illumination conditions.

In the last section of chapter 4 it was shown that the optical excitation induces a photo-voltage across the junction. This potential is local to the illuminated region as the lateral resistance of the *p*-type GaN is very high. In the presence of a metal providing an ohmic contact with high conductivity, the voltage will be shared across the metal surface and thus the light emission under the metal will be as appropriate to that voltage. Thus, it is expected that in the presence of defects or shunting paths the photo-generated potential on the metal will be reduced and consequently the emission under FM will be reduced under the entire contact rather than just locally where the shunting is dominant.

To study this effect, the 5QW piece processed with the quick evaluation method (see chapter 3) is excited and imaged under open circuit conditions. The partially (about 60% across the wavelength range of interest, i.e. 390-420nm) reflective Pd produces a double pass of the incident light thereby increasing absorption and the photovoltage under the metal. For a given optical intensity it was found that the luminescence under some Pd contacts was lower than in the un-metallized region (Fig 5.2 a and c). Under higher illumination intensity the metallized region produced higher luminescence intensity than the un-contacted region. Figure 5.2 shows images of such a poor contact (top-left) and a regular contact (bottom-left) from the 5QW sample. To understand the reason for this observation the I-V and electrical light-current (L-I) characteristics of the particular contacts were measured and shown in figure 5.2-e and -f, respectively. The slope of the poorer contact is less steep than the slope of the good contact. This is indicative of a higher diode ideality factor in the electrical characteristic for voltages of ~2V. In this voltage range, the minimum value of the ideality is 1 which corresponds to radiative recombination. Higher values are indicative of the dominance of non-radiative recombination. Under higher excitation levels the non-radiative current paths become saturated and the photovoltage can rise. This is also a confirmation that in the presence of an ohmic contact metallization the photovoltage is shared across the whole contact [2].

The analysis of the electrical and optical performance of the contacts from the fluorescence pictures depicted in figure 5.2 also suggests a quick way for yield analysis. Under open circuit conditions the photo-voltage, and therefore the

emission from the sample will depend on the electrical qualities of the full area under contact. So fluorescence imaging of the processed LEDs can quickly locate the devices that will have the best performance. This and the analysis of the spatial variation of the wafer also under fluorescence microscopy could identify defects and problems in the fabrication of devices.

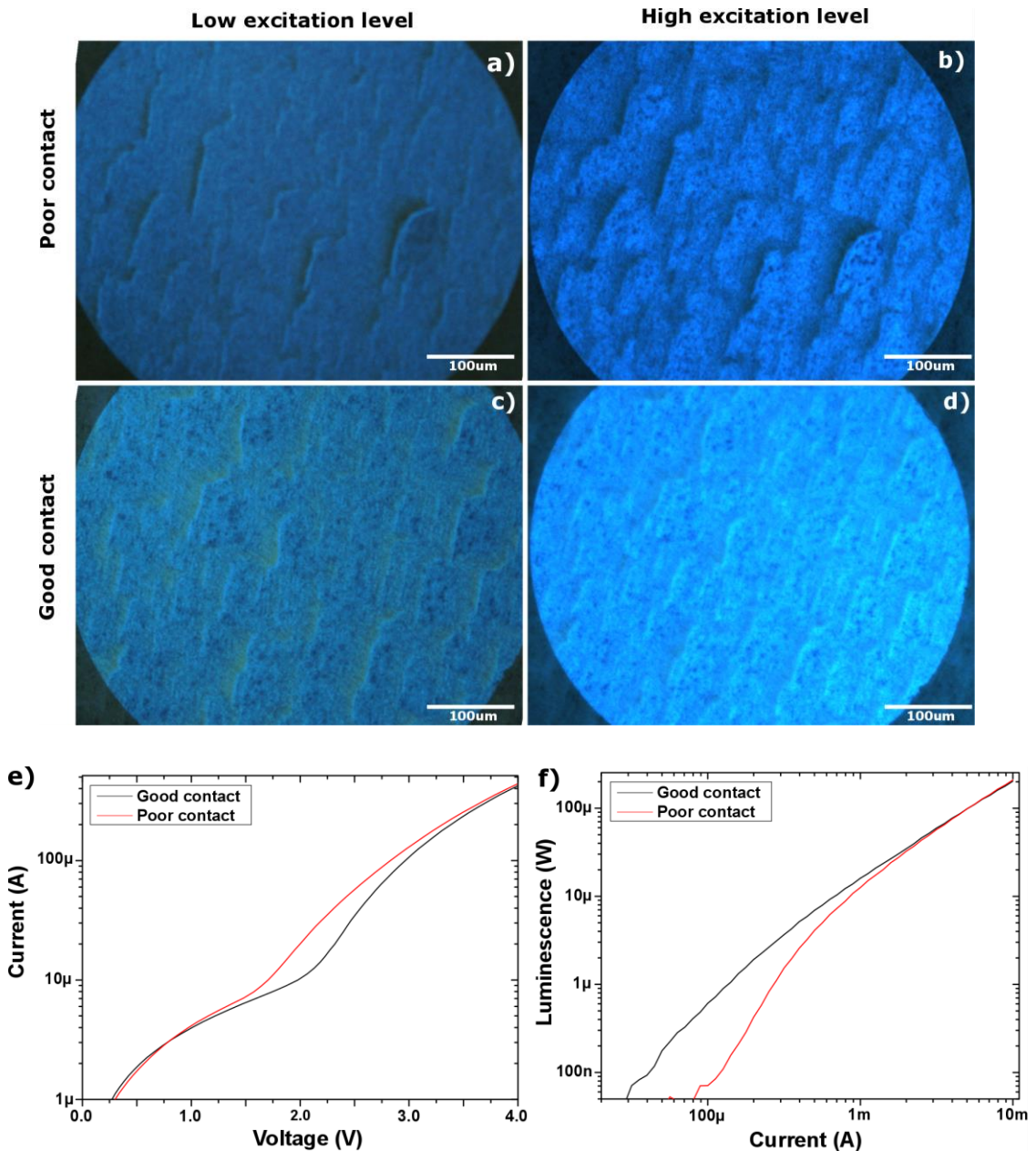


Figure 5.2: a) Fluorescence microscope images of the 5QW sample at low excitation levels a), c), and at high excitation levels b), d) of two partially reflective 250 μm diameter Pd contacts. The reduced intensity for a) and c) has corresponding poorer electrical and optical characteristics. e) IV characteristics of the contacts, f) LI characteristics from the same contacts.

5.2 Current density – voltage and piezoelectric fields

Figure 5.3-a shows the forward current density versus voltage (J-V) characteristics of diodes from each sample on a semi-logarithmic scale. All show an underlying diode characteristic given by the Shockley equation discussed in the previous chapter 4, section 2:

$$J = J_0 \exp(q(V - IR_s) / (n_{elec} kT)) \quad (5.1)$$

Here n_{ideal} is replaced by n_{elec} to indicate the ideality factor given by the slope of the IV characteristics under electrical excitation. Current (I) is also replaced by current density (J) so the area of the device is taken in account. For $V < 2.5$ V there is an exponential rise in the current before significant additional voltage is dropped across the resistive parts in the diode. The 5QW draws a factor of 10 less current for the same voltage when compared with the 10QW during the exponential rise (2.0 V to 2.5 V) despite having a thinner active region. The commercial sample draws the least current below 2.5 V and more current above 2.8 V with a larger slope of the log J - V curve indicating a lower n_{elec} . The 5QW sample has a distinct decrease in the slope of the log J-V curve at around 2.6 V which is not present in devices from the other two samples. The dynamic resistance (R_{dyn}) of the devices is plotted in figure 5.3-b as a function of J at 300 K and 400 K. There is a distinct shape of R_{dyn} for the 5QW sample at 300 K (black continuous line in the plot) with a change in the rate of decrease at around 2 A/cm². This distinct resistance change does not show when the sample is heated to 400 K (dotted black line).

The 5QW sample has a larger piezoelectric field across the QW and consequently a lower field across the barrier when compared to the 10QW sample. This results from the increased thickness of the QB in the 5QW sample as in a *p-i* (MQW)-*n* structure with piezoelectrically charged interfaces we can write the resultant field [3-5] in the QW (E_w) and QB (E_b) as a function of the applied voltage V (assuming it equals the junction voltage at low currents) and the built-in voltage V_{bi} of the diode as:

$$NE_w L_w + (N + 1)E_b L_b = V - V_{bi} \quad (5.2) [3]$$

or

$$E_w = (V - V_{bi}) / (NL_w) - (N + 1)E_b L_b / (NL_w) \quad (5.3) [3]$$

where L_w is the thickness of each QW, L_b the thickness of the QB, and N the number of QWs.

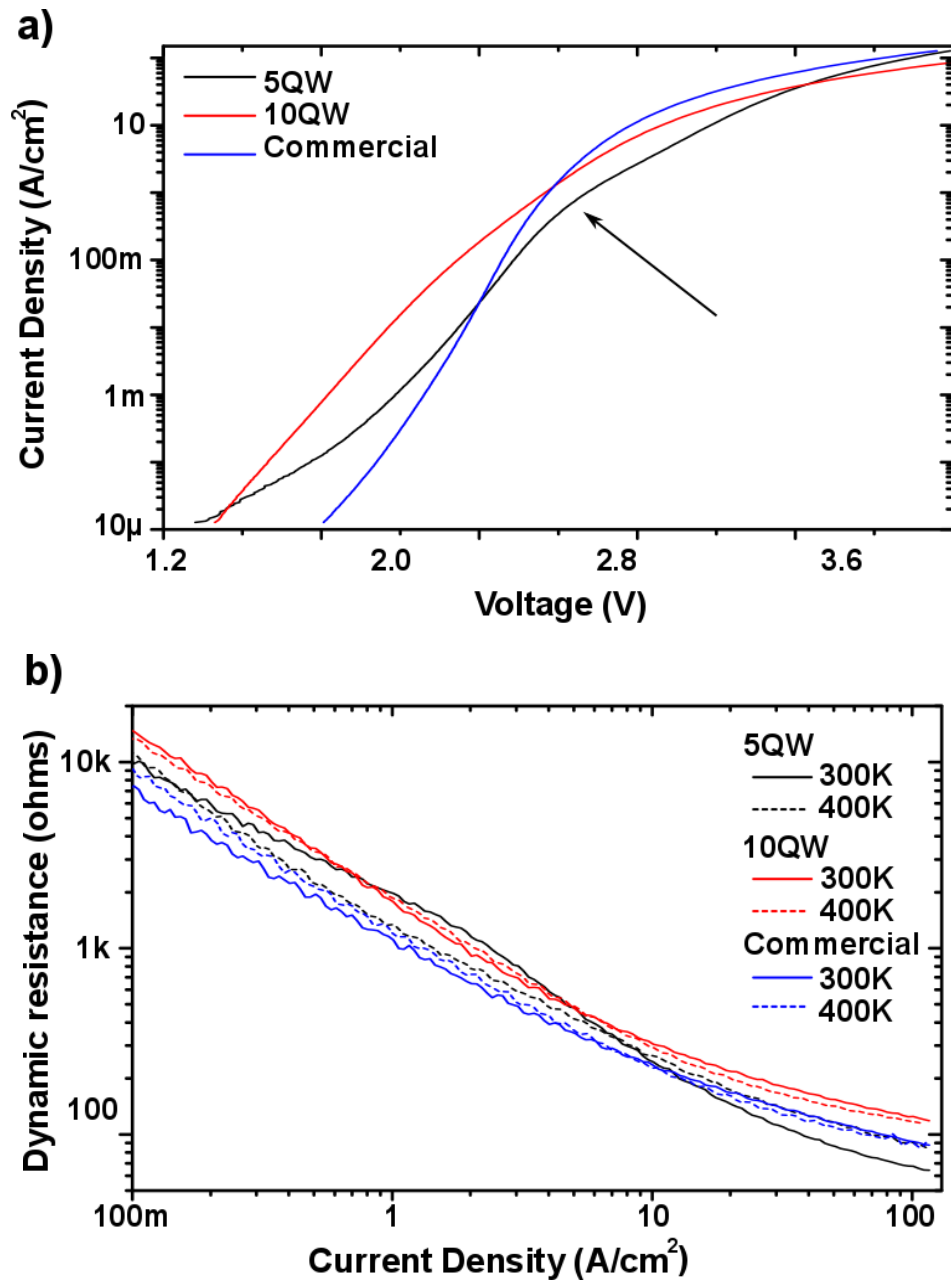


Figure 5.3: a) Semi-log scale current density - voltage (J - V) curve at 300 K illustrating the different exponential rise of current for each sample. The arrow highlights a change in character for the 5QW sample. b) Semi-log scale dynamic resistance versus current at 300 K (continuous lines) and at 400 K (dotted lines).

The field in the QW is opposite to that in the QB and is 12% greater for the 5QW sample compared with the 10QW sample. The weaker field in the QB of the 5QW together with the greater L_b results in a combined confinement potential of both the well and the barrier (figure 5.4-a) which can lead to a greater confinement of carriers, especially holes. As V is increased towards V_{bi} the field across the barrier reduces further while additional carriers are injected. Figure 5.4-b shows the field profile for the 5QW at 2.6 V where up to four electron states are calculated which can lead to carrier trapping. Similar effects are calculated for the hole states. At higher temperatures the thermal energy allows carriers to escape this potential.

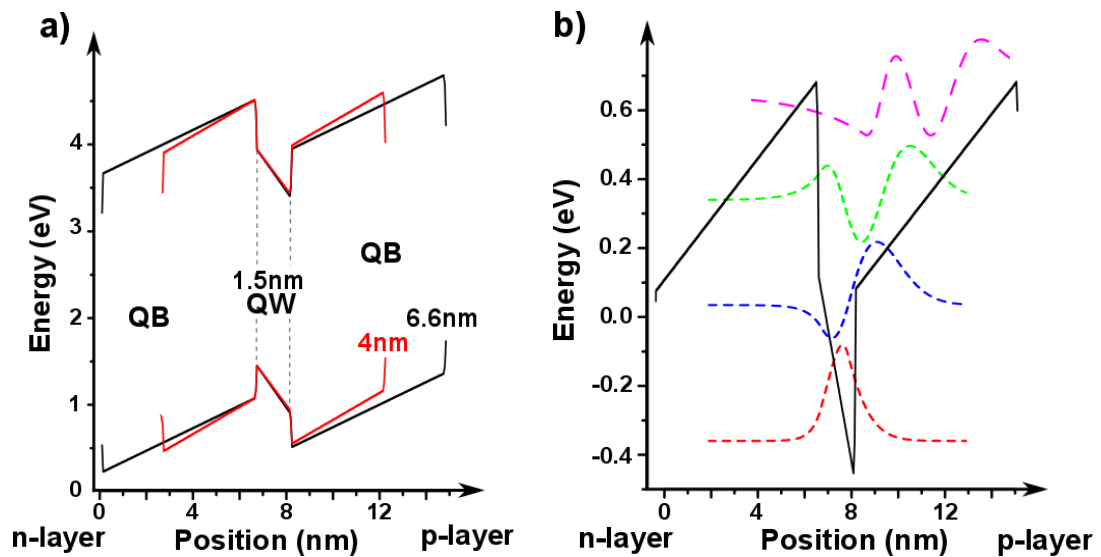


Figure 5.4: a) Unbiased conduction and valence bands of the 5QW and 10QW structures with 6.6 nm thick (black) and 4 nm thick QBs (red). b) Simulated conduction band diagram and confined electron wavefunctions at a forward bias of 2.6 V for the 5QW structure.

To gain further insight in the role of the piezoelectric fields in these samples, the emission spectra under electrical excitation and under combined electrical and resonant optical pumping are measured using the set up for bias dependent luminescence described at the end of chapter 4. Figure 5.5 shows the spectral emission under pure electrical and under combined optical and electrical

excitation. The normalized spectra under electrical excitation from 2.6 V to 3.0 V with a step of 0.1 V are shown in the left column with the plots belonging to the 5QW, 10QW and commercial sample from top to bottom respectively. The spectra are modulated by the Fabry-Perot resonances due to the reflection from the GaN to sapphire interface. The right column in figure 5.5 shows the spectra with combined optical excitation. Here the LEDs were illuminated through the polished substrate using a 405 nm laser diode with a maximum light power output of 20 mW as the excitation source. As in previous fluorescence images, there is a double pass of the light from the partially reflective palladium contact. The use of 405 nm assures that absorption is only in the QWs leading to uniform pumping of the QWs. These spectra were measured under an optical excitation of 200 W/cm² with an applied bias from -1.5 V to +1.5 V and a step of 0.5 V.

At low currents the polarization field in the QWs is enhanced because, under forward bias, the electric field points in the same direction as the field in the QWs which results in a red shift of the emission wavelength (equation (5.2)). At higher currents, the effect of the field can be screened by the increase in the carrier density in the QWs. This screening translates into a blue shift in the emission spectra. Figure 5.5-a shows little variation in the spectra from the 5QW sample under increased electrical bias for the selected voltage range. This indicates an equilibrium between change of the polarization fields and the increase in the carrier density. This is in contrast to the 10QW and commercial samples which both show a relative increase in the intensity within the Fabry-Perot resonances at shorter wavelengths with increasing voltage (figure 5.5-c and -e). Thus, the increase in carrier density for both these samples is dominant over an increase of the field in the wells.

Under combined electrical and optical excitation the 5QW sample is distinguished by a strong suppression of the emission at longer wavelengths with reducing electrical bias (figure 5.5-b). In addition, there is a reduction in intensity and FWHM. Emission at longer wavelengths originates from the electrons at the bottom of the QWs and the well is deepened (reduced in energy) under forward bias as the bias field is in the same direction as the piezoelectric field in the well. Therefore, a reduction in the external field in forward bias will affect mainly the

emission at longer wavelengths. Under reverse bias the external field helps carriers to escape from the QWs reducing the carrier density, which results in reduced recombination (including radiative recombination), and therefore a reduced emission intensity for all wavelengths.

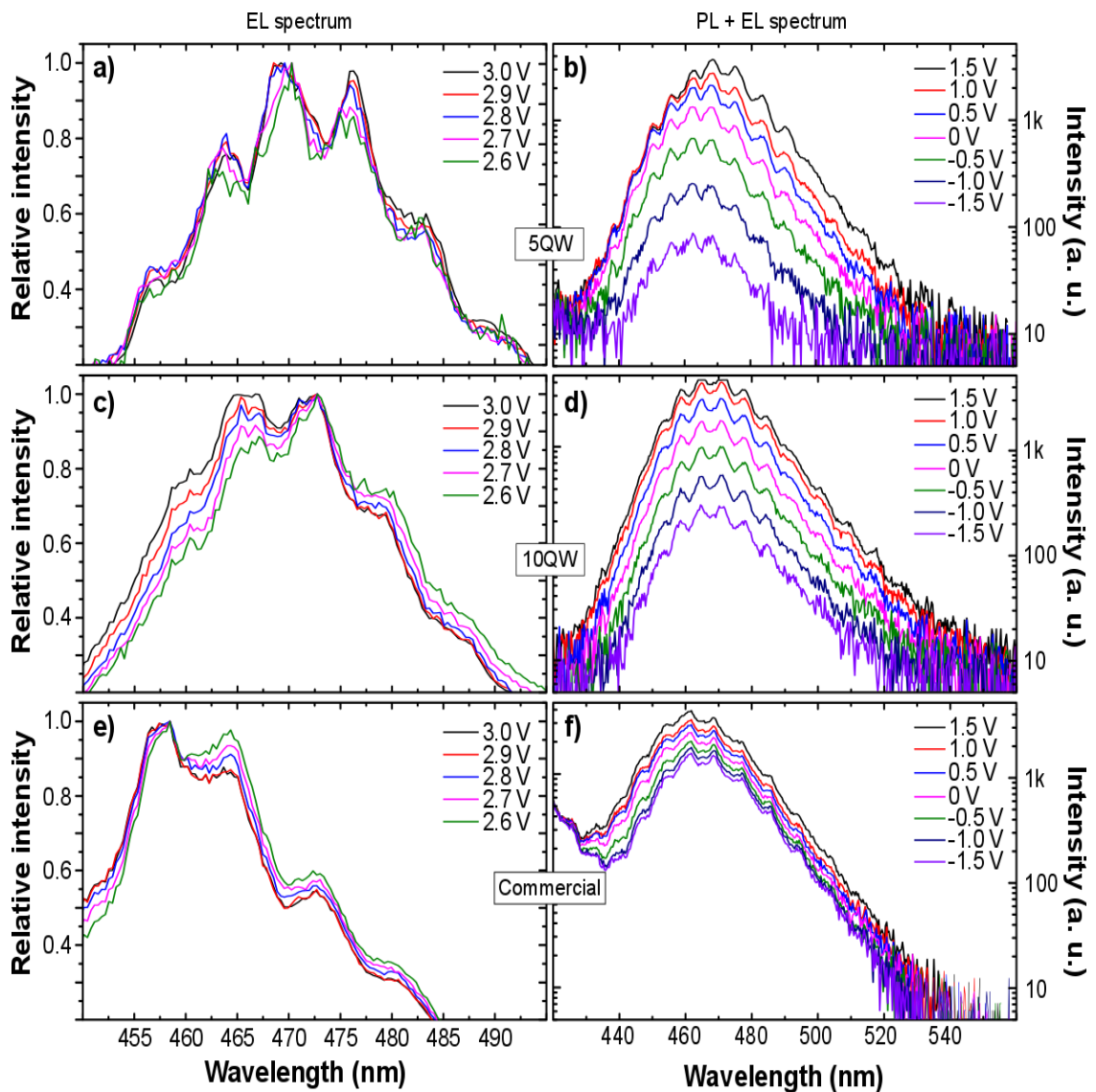


Figure 5.5: Left column: Electroluminescence spectra for the a) 5QW, c) 10QW and e) commercial samples with applied voltages ranging from 2.6 V to 3.0 V. Right column: Emission spectra with combined resonance excitation (200 W/cm^2) and applied bias ranging from -1.5V to +1.5 V for the b) 5QW, d) 10QW and f) commercial sample.

The spectra from the 10QW sample under the same conditions (Figure 5.5-d) do not show any significant difference between the longer and shorter wavelength parts of the spectra and the decrease of the intensity is a result of the reduction of the carrier density. Under optical excitation the commercial sample shows an additional emission peak at 420 nm (Figure 5.5-f) which is not affected by changes in the applied bias. A better view of this additional peak in the emission is shown in figure 5.6. This could be due to an *n*-doped InGaN layer (or superlattice) below the QW structure which is used in many commercial LEDs to improve the overall efficiency [6]. The absorption of the pump light by the InGaN underlayer provides an additional source of carriers (minority carrier holes) for the QWs which explains why, as the electrical bias is reduced, the reduction in the MQW emission intensity is much less than for the 5QW and 10QW samples. It should be remarked that there is a significant amount of light emission for all samples, and especially the commercial one, at short circuit ($V = 0$ V). This indicates that not all the photogenerated carriers escape at this condition.

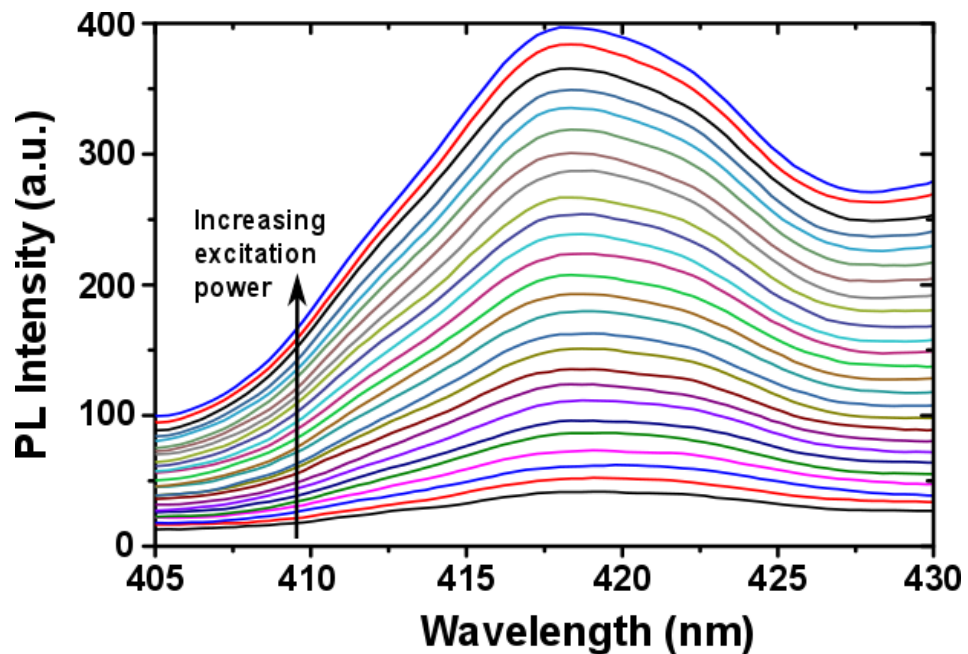


Figure 5.6: Additional emission at 420 nm from the commercial samples at different optical power excitation levels

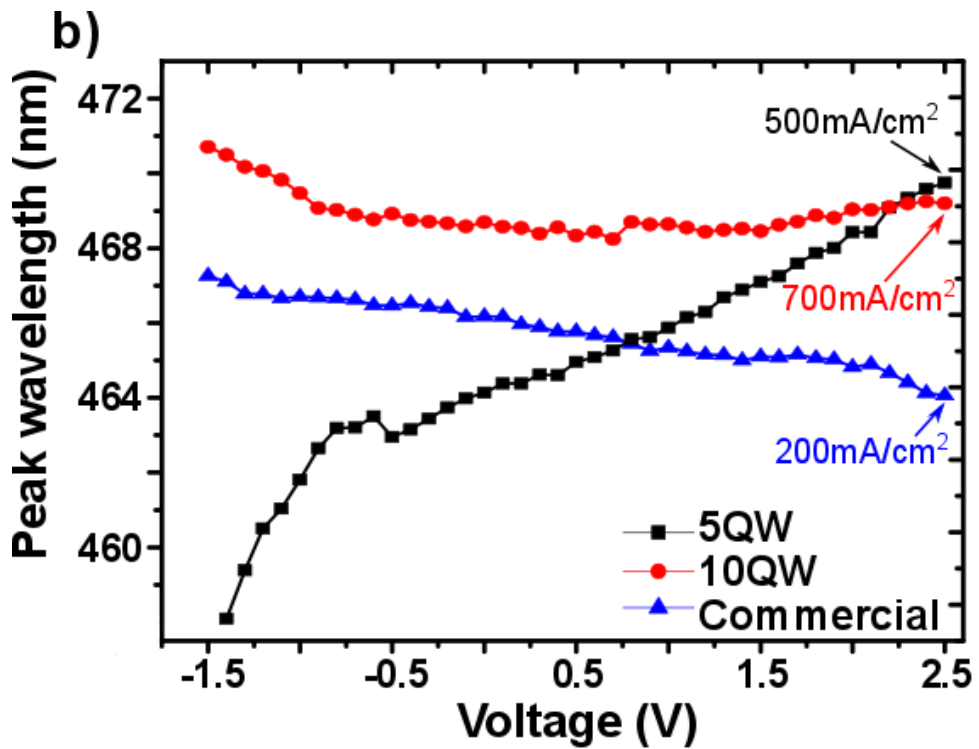
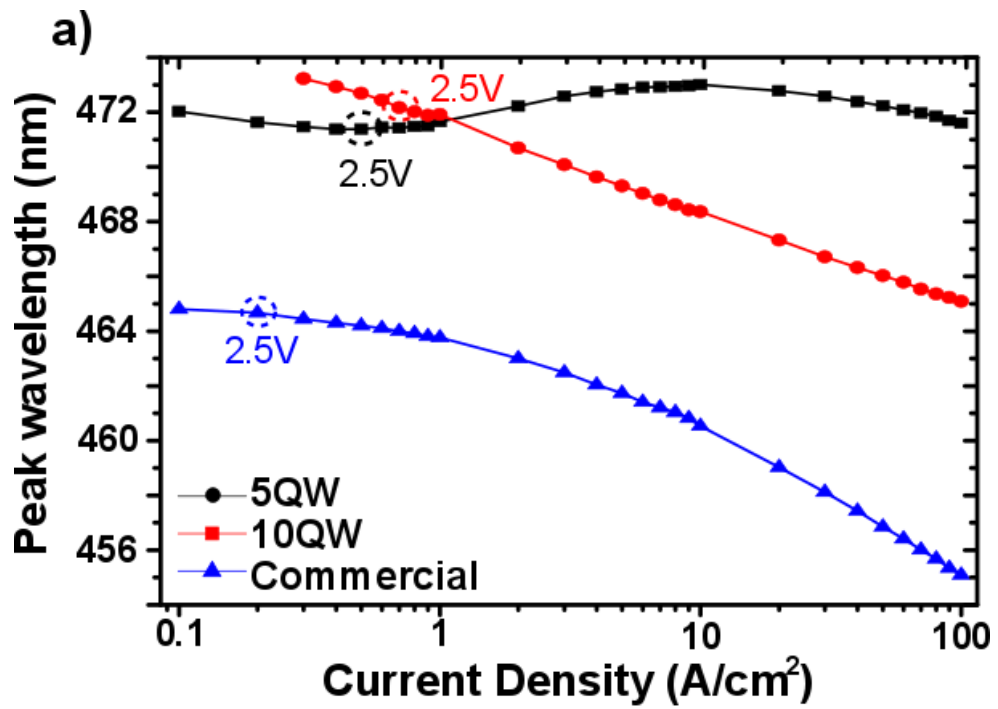


Figure 5.7: a) Peak wavelength versus current under electrical excitation, b) peak wavelength versus voltage under optical ($200 W/cm^2$) and electrical excitation.

The peak emission wavelength from these measurements is obtained by fitting a Gaussian function to the spectra. Figure 5.7-a shows the variation of peak wavelength with current under electrical excitation alone while figure 5.7-b shows the variation of peak wavelength with applied bias under an optical excitation of 200 W/cm^2 . These plots highlight the distinctive properties of the 5QW sample; at very low current there is a slight blue shift due to the band-tail states of the QWs being filled with carriers before a red shift is measured. At high currents the effect of the piezoelectric field is screened and there is a blue shift again. This is in line with the larger polarization field in the QW of the 5QW sample. The 10QW and commercial samples show only a blue shift of the peak wavelength with increasing current indicating that the emission is dominated by the screening of the piezoelectric field by filling of the states in the QW.

Figure 5.7-b shows that the change in the direction of the electric field (voltage bias) from opposite to the same direction as the piezoelectric field in the QWs causes a large red-shift in peak wavelength for the 5QW sample. This is also in agreement with the piezoelectric field being larger in this 5QW sample. The emission peak of the 10QW and commercial samples show a slight red-shift (with increasing bias) at a reverse bias of 1.5V where only a small amount of light is detected. This is due to the bottom of the QW starting to slope in the direction of the applied negative bias field. To help compare the plots from figure 5.5 and figure 5.7 the current density when 2.5 V is applied is indicated. The addition of the optical excitation shifts the emission peak to shorter wavelengths for all the devices which is explained by the increase in the carrier density in the wells under optical excitation.

Measurements under electrical and resonant optical excitation were done also on large area contacts for the 5QW and 10QW samples. These experiments allow us to use lower current densities and show us a broad yellow band (YB) emission (500 nm – 600 nm) under both low forward bias electrical injection and under optical pumping. Figure 5.8-a shows the electroluminescence from 5QW and 10QW devices under forward biased electrical injection, respectively. The YB part of the spectrum is stronger for the 10QW sample (red lines) and is comparable with the QW emission under forward bias at bias levels below 3 V.

This is the reason why figure 5.1-b has a different colour to the eye than the other two samples. The photo-voltage created by the fluorescence microscope is only around 2.2 V, so the camera collects both emissions (yellow and blue) and combines in what seems to be green emission. Figures 5.8-b and -c show the spectrum of the emission at -2 V and -3 V with optical excitation powers of 66 W/cm², 133 W/cm² and 200 W/cm² for the 5QW and 10QW samples, respectively. It is clear that when the devices are reverse biased and optically pumped the emission from the QW is extinguished at -3 V while the YB emission remains constant but proportional to the pump power. This is an indication that the yellow emission may be a result of optical absorption in this case. The YB is not present if the MQW region is etched away and illuminated by 405 nm light. This removes the possibility of the *n*-side as a source of the YB; on the other hand, although yellow emission from Mg-doped GaN has been reported when the layer remains *n*-type or semi-insulating [7], such reports are scarce and circumstances do not seem to relate to the case studied here. All of this suggests that the YB origin is in the MQW region associated with traps in the QB particularly in the low-temperature grown region. Carbon - oxygen complexes with defect levels 0.75 eV above the valence band maximum have been recently shown to be the source of yellow emission in undoped GaN [8]. Under illumination with 405 nm light there is absorption in these complexes that can result in yellow emission that only depends on the optical power as in figure 5.8 -b and -c. In this case there is a wide YB because absorption happens for defects across a wide range of energies and because some of them exist deep in the bandgap, they are barely affected by changes in the bias. Under electrical excitation carriers can demote/promote to some of these defects that are close to the valence/conduction band, which results in emission closer to the emission from the QWs. In addition, such defects on the upper side of each quantum well would promote hole tunnelling and thus could explain the higher ideality factors measured on these samples as shown later. This explanation also agrees with the stronger YB emission from the 10QW due to the increased number of QWs.

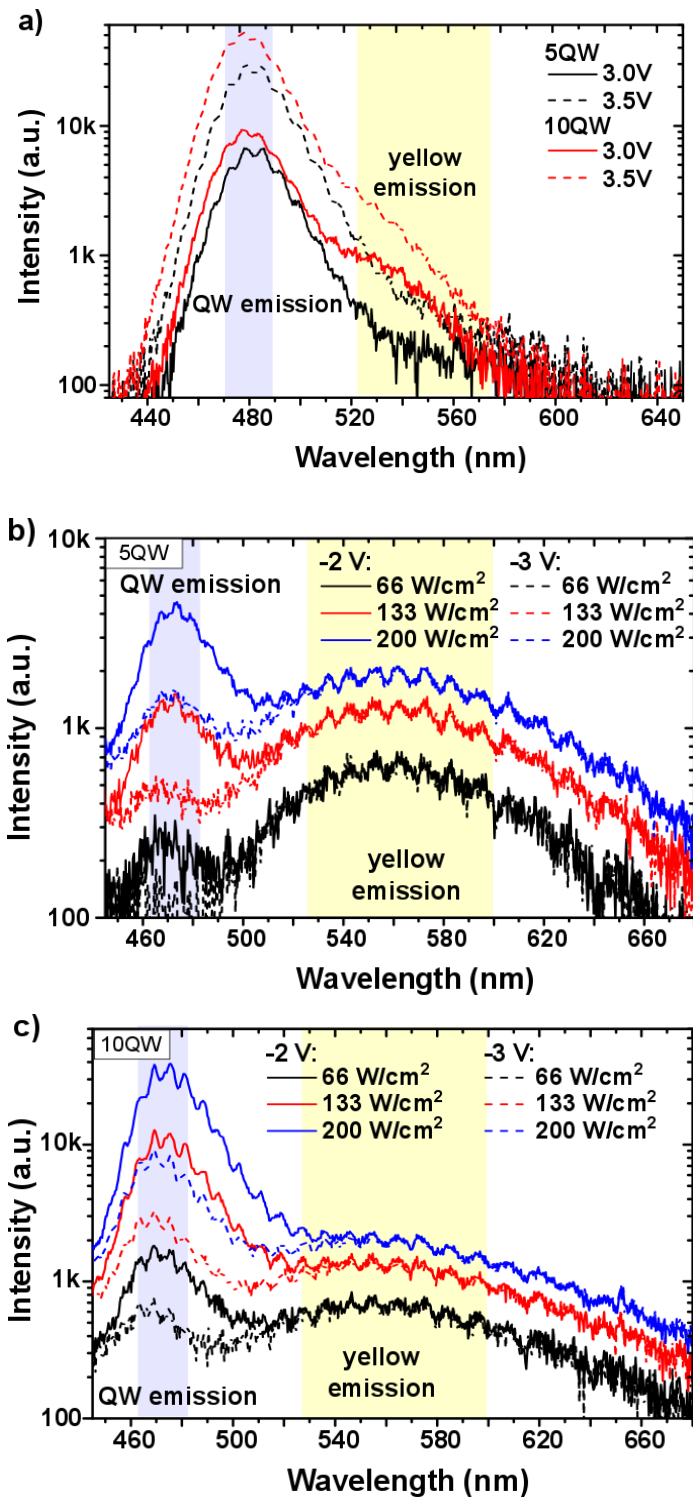


Figure 5.8: a) 5QW (black lines) and 10QW (red lines) under forward bias of 3 V (continuous lines) and 3.5 V (dotted lines): Both samples show yellow emission band between 500 and 600 nm. b) Emission at -2 V (continuous lines) and -3 V (dotted lines) for three different optical power levels for the 5QW and c) for the 10QW samples: QW emission is reduced while yellow emission does not depend on applied bias.

All the information from this section shows the importance of using resonant optical excitation in combination with electrical excitation: the effect of QB thickness on the piezoelectric field within the QW means that a change in QB thickness can result in a significant change in device performance. Future possible work can benefit from these experiments because they give a methodology to help study other interesting effects such as the role of doping the QBs and its effect on piezoelectric fields. Investigation of the effect of changing the width of the QW/QB thickness in semi-polar and non-polar samples, where the effect of piezoelectric fields should be small, can also be studied using these experiments.

5.3 Analysis of ideality factors

The electromotive force (qV) which causes the separation of QFLs for electrons and holes in the active region of an LED drives current transport and light emission. In section 4.2 there is a discussion of ideality factors where it was shown that current (density) and voltage have – to a first approximation - a Boltzmann dependence of

$$J, L \sim \exp(q(V - IR_s)/n_{ideal}kT) \quad (5.4)$$

It was also introduced that the light emission L depends on the product of the hole and electron density, resulting in:

$$L \sim Bnp \cdot \exp(q(V - IR_s)/kT) \quad (5.7)$$

Because light is generated when an electron and hole diffuse to the pn-junction and recombine, the ideality factor n_{light} for this type of recombination will be 1. Considering now other possible recombination mechanisms, in a similar way, Shockley-Read-Hall (SRH) trap related recombination at the junction is characterised by an ideality factor of 2, because only one type of the carriers is involved. This brief introduction shows how by measuring the voltage dependent ideality $n_{ideal}(V)$ one can obtain information about the dominant recombination process at a given voltage. However, these correlations are only true when the

voltage measured is the QFL separation which fails in the presence of non-ohmic contacts or if significant resistance effects are present, that is, significant voltage is dropped outside the p - n junction region, as in the case of our 5QW and 10QW samples. For an LED the QFL separation must be less than the bandgap voltage (2.64 V here) as a higher QFL would correspond to gain as in a laser.

Several factors can also influence the ideality factor: in [9] authors have shown that the electrical ideality is reduced if the QBs are intentionally doped. Transport of carriers by tunnelling can have a strong influence on the ideality factor [10, 11] and has been reported to lead to idealities which range from 3.5 up to 7 [12]. An important note about tunnelling is the distinction between tunnel currents which result from carrier being transported directly across the junction, that is, from one side to the opposite one, as against tunnel currents which result in carriers entering the quantum wells. Nevertheless, a GaN homojunction p - n diode with near unity ideality has been recently demonstrated [13] while, with improving device quality, an InGaN LED with an electrical ideality factor of 1.1 has been shown [14]. This low ideality was realized by minimizing the device resistance and was correlated with better internal quantum efficiency in the LED [14].

To remove some of the ambiguity related with ideality factors, here four different measurements of the ideality factor using electrical and combined electro-optic techniques are presented. The first one, the electrical ideality factor n_{elect} , is extracted from the minimum in the slope of the log J-V curves at 300 K (continuous lines) and 400 K (dotted lines) as shown in figure 5.9. At 300 K the ideality factors for the 5QW and 10QW samples are close to 3.5 in the 1.6 – 2.4 V range. Above 2.4 V the resistance associated with the small device area (100 μm diameter) obscures the true ideality factor. These relatively high values suggest that a tunnelling mechanism is involved in the current transport at 300 K. This also corresponds with the defect emission measured and the higher current drawn at these voltages compared with the commercial sample. For the commercial sample, n_{elect} is close to 2 which could be associated with the current transport or SRH recombination in the intrinsic region.

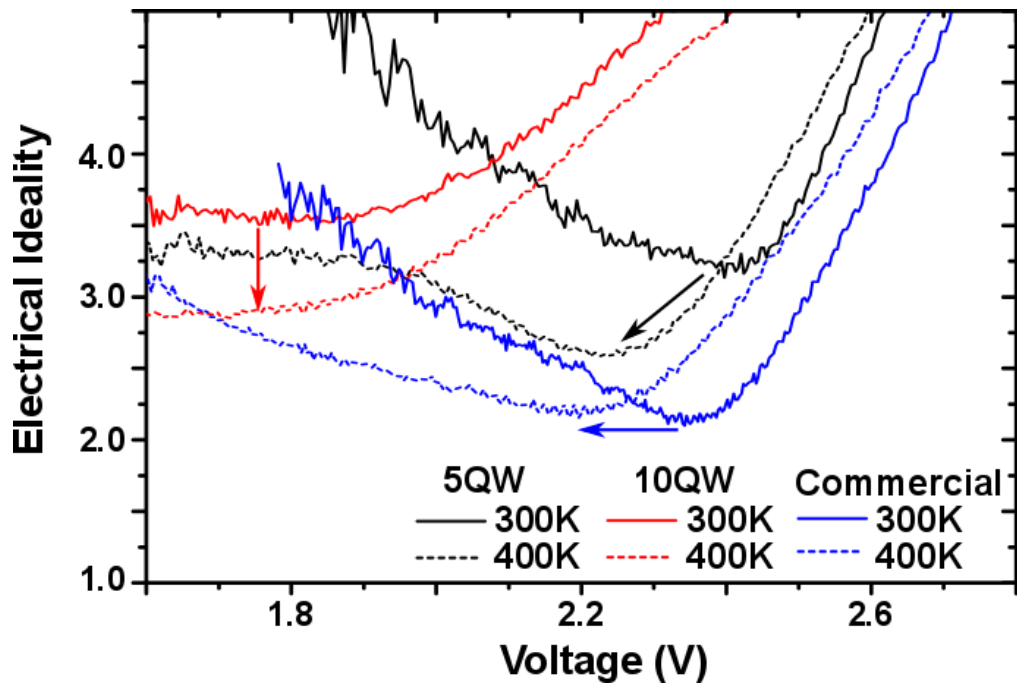


Figure 5.9: Electrical ideality factors against voltage using J-V measurements at 300 K (continuous line) and 400 K (dotted lines). The ideality factor for the 5QW and 10QW are temperature dependent.

When the temperature is increased to 400 K, the minimum ideality factor of the 5QW is reduced to ~ 2.5 while for the 10QW it is reduced to ~ 2.8 . The ideality factor of the commercial sample increases slightly from 2 and the voltage where the minimum occurs reduces by around 200 mV. A similar change happens with the 5QW and is due to the reduction of the bandgap with temperature [15]. This change is not measured for the 10QW, though identification of the position of the minimum ideality is not possible. The reduction in the ideality factor with temperature is related to the contribution to carrier transport from thermionic emission across the wells as the tunnelling should be independent of temperature.

It has been introduced in section 4.2 the ideality factor n_{light} and defined as the ideality factor for the radiative recombination current. As previously indicated, this ideality factor is extracted from the slope of the log L-V curve so measurement of partial output power from the LEDs is sufficient. Figure 5.10 presents the light output density (Luminescence/Area) versus voltage

characteristics of the LEDs on a semi-logarithmic scale. Despite the different number of QWs, similar levels of light are measured for both the 5QW and 10QW samples at a given voltage. As there is a larger current density driven through the 10QW sample at a given voltage (figure 5.3-a) this indicates that there is more non-radiative recombination in the 10QW device. The extracted values for n_{light} are plotted in the inset of figure 5.10 with minimum values of ≈ 1.5 , 1.8 and 1.1 for the 5QW, 10QW and the commercial sample, respectively. An n_{light} of 1.1 as measured on the commercial sample is expected for radiative recombination. The origin of the higher n_{light} for the 5QW and 10QW is due to non-radiative recombination in the QWs. The ideality of the 5QW increases at a lower voltage than the 10QW. As discussed in chapter 2, the 5QW and 10QW samples have no additional layers to prevent carriers being injected at lower bias. The higher light emission intensity at $V < 2.35$ V for the 5QW and 10QW samples as compared to the commercial sample could be useful in some applications despite its low efficiency.

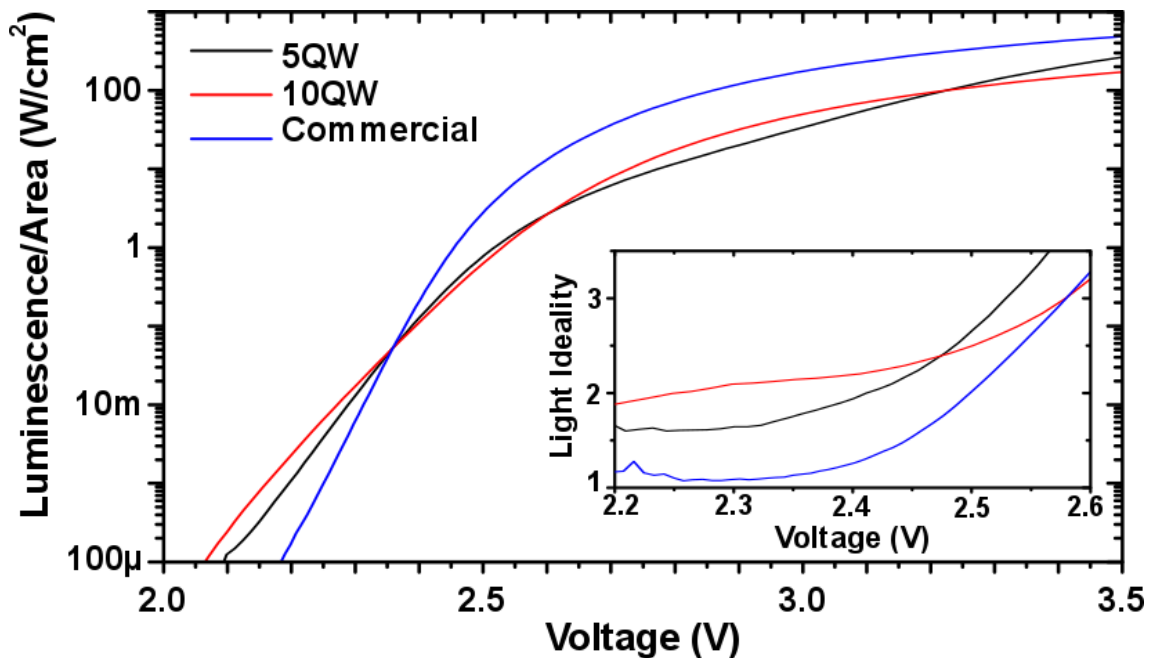


Figure 5.10: Semi log scale light output density – voltage (L - V) at room temperature of the 5QW, 10QW and commercial sample. The sharper rise of the commercial sample (blue line) corresponds to a lower ideality factor (see inset).

The resonant optical pumping set up described in chapter 4 is used now to measure the I-V characteristics from each sample from -4 V to +2.75 V under different illumination intensities. Figure 5.11 shows the characteristics where black lines indicate the measurement without any illumination (J_{dark}) and the coloured lines indicate the measurements with increasing laser output power from 33 to 200 W/cm² with a step of 8.3 W/cm². Several observations can be made from these plots; at -4 V the 5QW and 10QW samples reach a saturation in the current collected indicating that all the photo-generated carriers in the QWs are extracted. While no quantum well emission is detected at -4V, a weak yellow band emission is detected as discussed earlier. The measured photocurrent at reverse bias allows us to estimate the percentage of the light absorbed by these samples which is 5.6% for the 5QW sample and 12.5% for the 10QW sample. This corresponds to an absorption of 1.4% of the 405 nm light by each QW for the 5QW and 1.56% per QW for the 10QW sample. The effect of the partially reflective (60%) Pd contact, which allows a double pass of the light has to be taken in account and when this is done, the absorption becomes approximately 0.8-1% in each 1.5 nm thick QW per pass. For the commercial sample this analysis cannot be accurately performed due to additional absorption in the InGaN underlayer and the unknown number of wells.

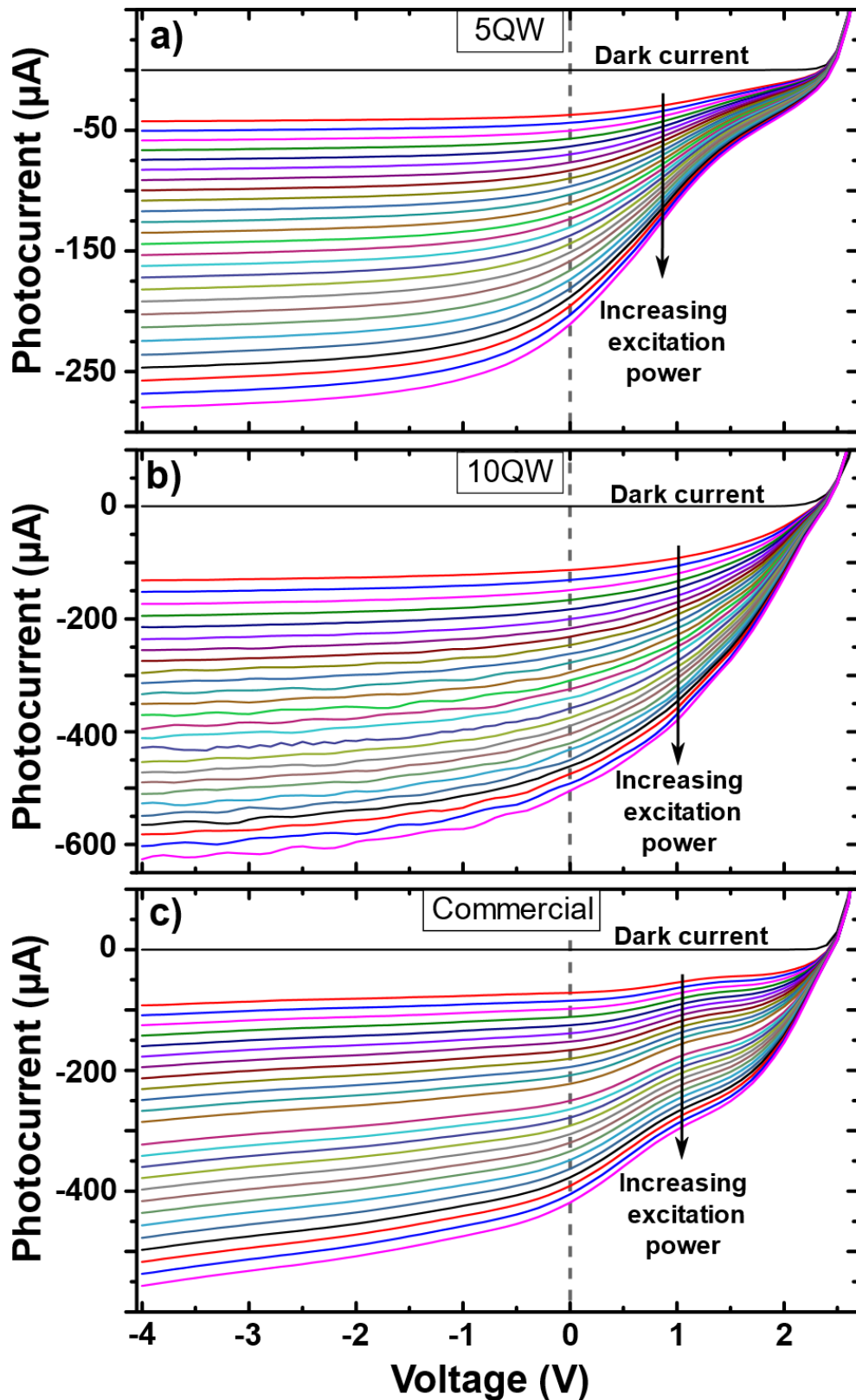


Figure 5.11: Photoresponse measurements for a) 5QW, b) 10QW and c) Commercial sample. Black lines correspond to measurements without illumination while the coloured lines show the response with an increase in the optical excitation from 33 W/cm^2 to 200 W/cm^2 .

These measurements show the effect of the thicker barriers of the 5QW sample as compared with the 10QW sample. At high reverse bias both samples have their QWs depleted with the ratio between their photocurrents being slightly higher than the factor of 2 that would be expected based on the double number of QWs. Between 0 V and 2 V where the photovoltaic effect dominates a strong voltage dependence in the extraction of the photogenerated carriers is measured. In comparison with the 10QW sample the 5QW photocurrent produced for $V > 0$ reduces significantly. This shows that the carriers are being more strongly trapped in the overall QW/QB region of the 5QW sample at a given forward voltage due to the thicker barriers resulting in deeper confinement [16]. The increase of the inbuilt field in the QWs by the photovoltage confines the carriers even more increasing the carrier dwell time and allowing recombination processes within the active region to dominate. The lower degree of confinement in the 10QW sample on the other hand permits better escape of the carriers at higher voltages. A similar dependence of carrier escape on barrier thickness was reported in [17]. The collected photocurrent in the commercial sample does not fully saturate even at -4 V. The reason for this could be strong carrier confinement in the QWs for this samples or, alternatively, it could be attributed to the depletion layer extending into the absorbing InGaN underlayer resulting in the collection of holes which produce the small additional photocurrent, enough to prevent saturation at that reverse bias. It should be noted that because the structure of this sample is unknown, other factors may be responsible for preventing the saturation of the photocurrent.

By measuring the luminescence from the samples as a function of voltage it is seen that the missing photocurrent is translated into a corresponding increase in light emission from the QWs. In figure 5.12 the peak intensity of the emission from the LED due to photo and electroluminescence as a function of the applied voltage is measured simultaneously with the photocurrent under three pump intensities of 66 W/cm^2 , 133 W/cm^2 and 200 W/cm^2 . The photocurrent reduces as the voltage goes from reverse to forward bias while the emission increases at similar rate. Only at voltages above 2 V does emission from the electroluminescence becomes significant. The photocurrent of the commercial

sample as with the 5QW sample shows a distinctive decrease around 1 V which is accompanied by a corresponding increase in photoluminescence. These measurements reveal differences in the properties of the diodes at voltages < 2 V which are associated with trapping of carriers in the QWs.

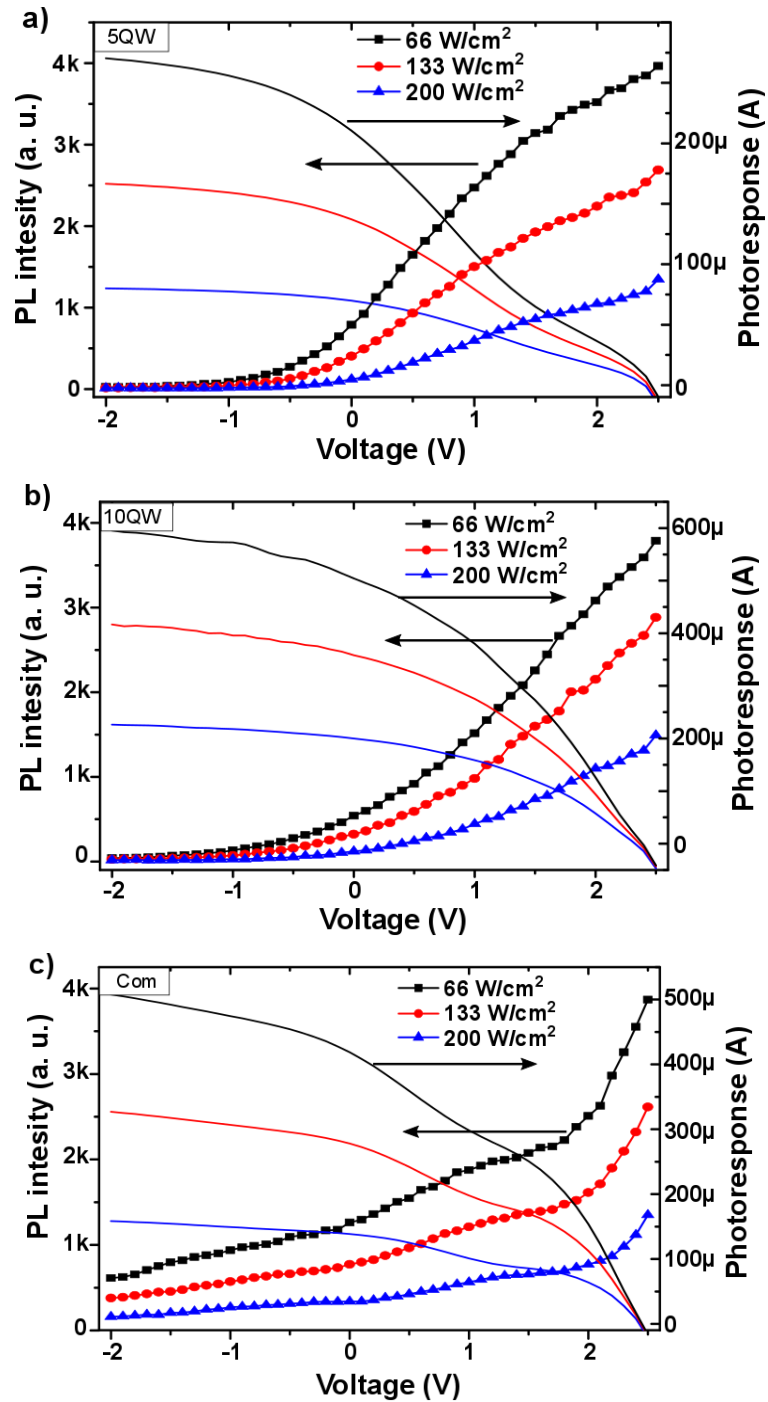


Figure 5.12: Measured photocurrent and peak intensity of the luminescence for the a) 5QW, b) 10QW and c) commercial sample as a function of pump power.

In the previous chapter the short circuit current density J_{sc} and the open circuit voltage V_{oc} have been introduced. Under resonant optical excitation, J_{sc} is the result of carriers escaping the QWs that can flow to the p - and n - contacts under SC conditions. V_{oc} is the voltage generated under resonant optical excitation by the same carriers that escape, that under the SC conditions would escape but under OC conditions concentrate in either p - or n -side. The relationship between them is given by:

$$J_{sc} = J_{sc0} \exp(qV_{oc}/n_{pv}kT) \quad (5.8) [18]$$

allowing a photovoltaic ideality factor n_{pv} to be extracted from the measured log I_{sc} - V_{oc} curve. Figure 5.13 shows that this approximation holds for all samples despite the poor fill factor and the complex dynamics between these end points. Recall also from figure 5.11 that there is incomplete carrier escape at $V = 0$ V. The n_{pv} values give information about the recombination and transport mechanisms that take place in the intrinsic region without external contribution from the p - or n -side of the junction. In figure 5.13, the 5QW sample shows an increase in n_{pv} with voltage from 2.1 to 2.9 indicating a transition between processes and an increased non-radiative recombination. For the 10QW sample, n_{pv} is 2.7 which is lower than n_{elec} but n_{pv} is measured at higher voltages. The commercial sample shows n_{pv} of 1 and less at higher voltages. This lower value could come from the absorbing n -type InGaN layer as a second photovoltaic source in series which acts to reduce the measured voltage and effectively reduce the extracted ideality. Auger recombination can lead to an electrical ideality of $2/3$ but that is not the case here due to the low carrier density.

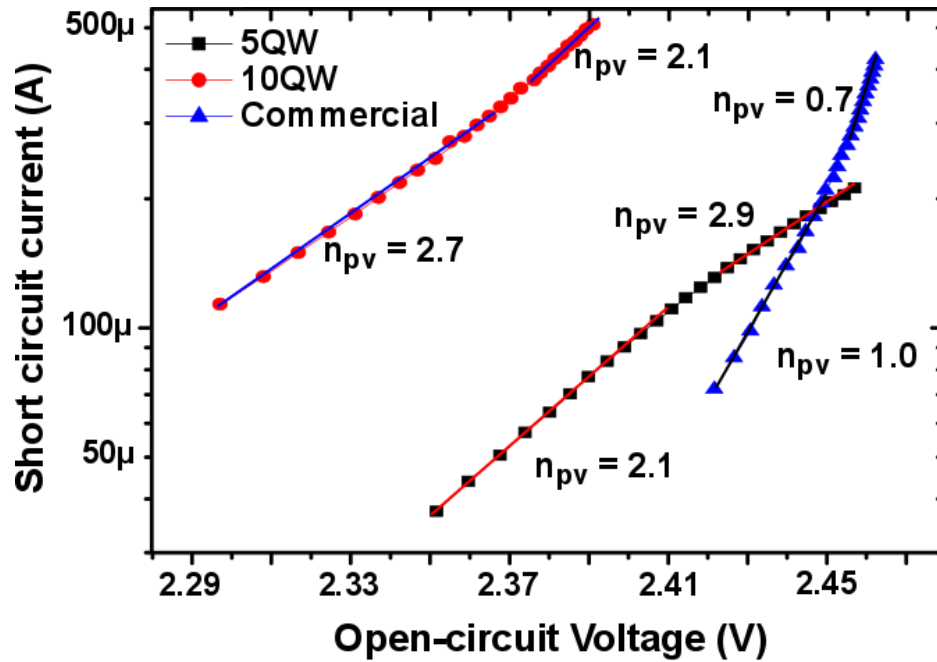


Figure 5.13: Semi-log plots of short circuit photocurrent versus open-circuit voltage for the three samples along with the extracted ideality factors.

The fourth method to extract a voltage ideality factor is to measure the photoluminescence intensity under resonant optical pumping while keeping the external current to be zero [19]. This should be a more accurate method to measure the recombination ideality as it does not rely on the radiation to be represented by J_{sc} which can be compromised by incomplete carrier extraction. With increased pump intensity, the PL increases exponentially with the generated V_{oc} . Figure 5.14 shows the measured data where the extracted ideality n_{pl} is indeed slightly lower than measured under the photovoltaic measurement. Again, the 5QW sample shows a change in the ideality around 2.4 V. The high values for n_{pl} show that non-radiative recombination in the quantum wells is a significant factor in the 5QW and 10QW samples. As with the PV measurement the commercial sample shows $n_{pl} < 1$ which comes from diffusing holes created in the n -type InGaN recombining with electrons created in the MQW region enhancing the light emission at a given V_{oc} .

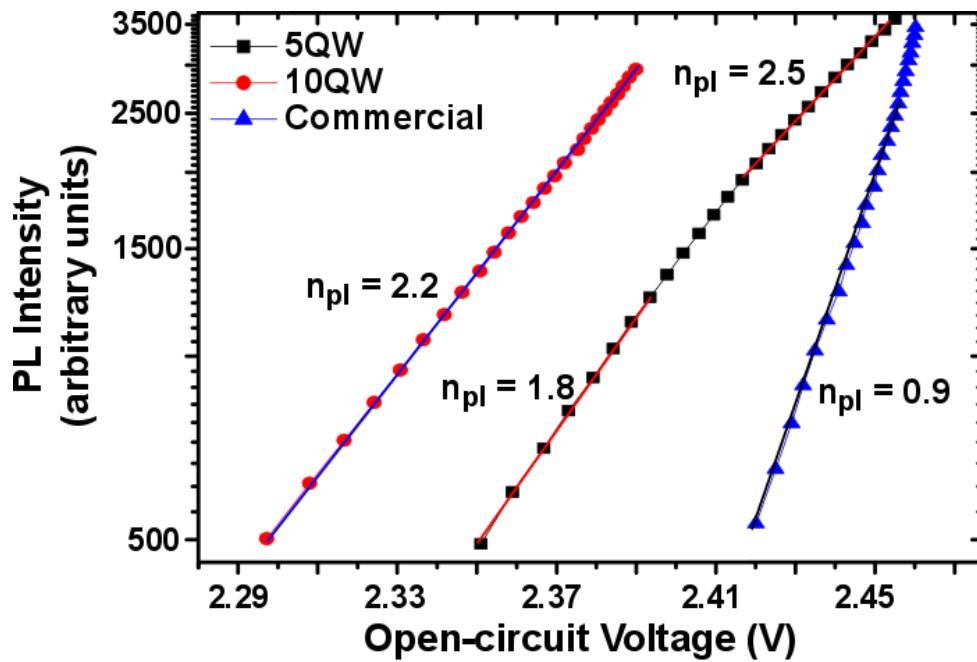


Figure 5.14: Semi-log plots of short circuit photoluminescence versus open-circuit voltage for the three samples.

At this point, the diode ideality factors extracted under different combinations of electrical and optical excitation, as summarized in table 5.1, can be used to explain the recombination and transport properties of the devices. The ideality extracted from the J-V measurements are consistently higher than those extracted from the optical measurements. This reflects the contribution of carrier transport outside the intrinsic region of the diode: in the electrical measurements the measured ideality factors include several contributions from additional voltage drops that hide the junction voltage which determines the carrier flow into the QW region. Drops at the metal to semiconductor contacts, or across the *p*-GaN and *n*-GaN layers do not affect carrier densities in the active region but set the applied voltage to a value higher than the junction voltage. The J-V measurement is also limited by the resistance of the small area diodes. The optical measurements involve carrier transport and redistribution in order to establish the forward voltage.

Table 5.1: Measured minimum ideality factors from electrical measurements at 300 K and 400 K, from radiative current measurements, from photovoltaic measurements and from photoluminescence measurements.

Sample	n_{elec} (300 K)	n_{elec} (400 K)	n_{light}	n_{pv}	n_{pl}
5QW	3.3	2.6	1.5	2.1 → 2.9	1.8 → 2.5
10QW	3.6	2.8	1.6	2.7	2.2
Commercial	2.1	2.2	1.1	1.0	0.9

The 5QW sample shows distinctive piezoelectric effects in the red-shifting of the EL with increased bias. It also shows a distinct break in its photovoltage characteristics around 2.4 V which is indicative of relatively reduced radiative recombination above this voltage. One possibility for this change is that the radiative recombination rate is being reduced due to increased field across the wells and a limitation on the radiative recombination through the band-tail states. A second possibility depicted in figure 5.15 is that part of the measured voltage in the 5QW sample is being dropped across either the finite p -/ n -doping or across each QW/QB pair which is termed QFL loss in reference [20]. This is larger for the hole QFL due to the lower hole mobility and is highest across the QWs on the p -side of the junction. While such a voltage drop should also be present in the 10QW sample, because strong piezoelectric properties were not measured in that sample, this could be due to a reduced interface charge on the QWs on the p -side of the junction associated with the accumulation of strain in that structure. In figure 5.15 the change of the QFL at 2.3 V (blue lines) and 2.6 V (green lines) for the 5QW and the 10QW are shown. For the 10QW sample, figure 5.15-b shows that both QFL drop in a similar way at both voltages. In the other case, the 5QW shows an increased drop of the QFL on each QW that can be attributed to the increased interface charge.

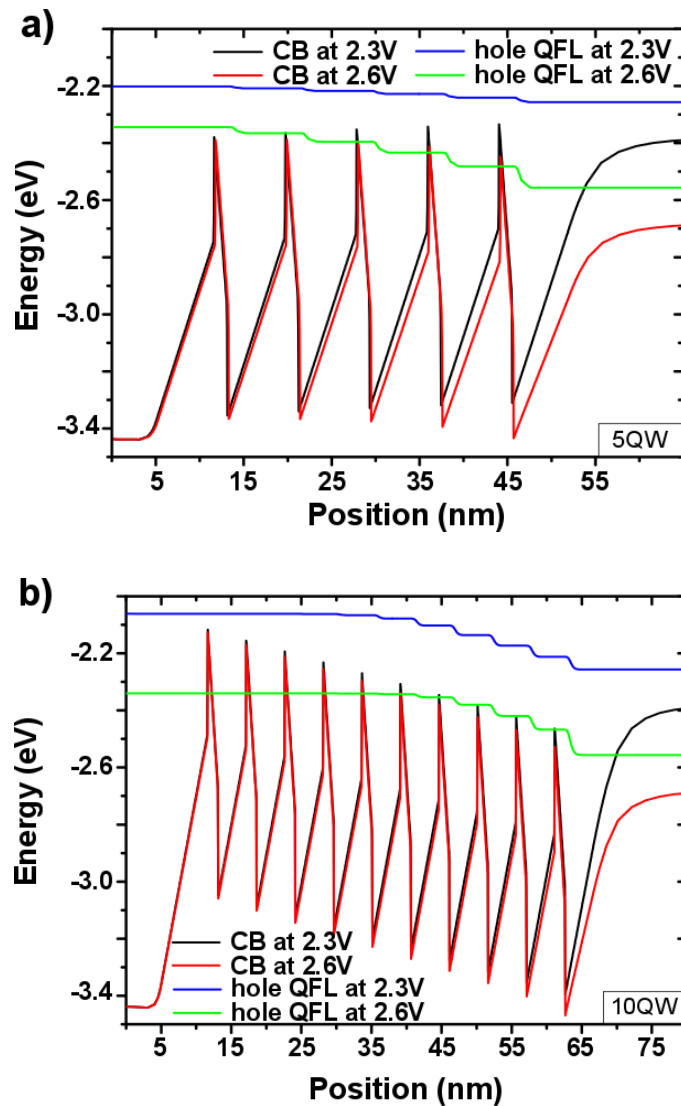


Figure 5.15: Valence bands and QFL of the a) 5QW and b) 10QW structures at 2.3 V and 2.6 V.

This section has shown that the use of combined resonant optical excitation and electrical excitation gives valuable insights into carrier dynamics in GaN LEDs using photovoltaic measurements. Ideality factors calculated in photovoltaic mode and from short circuit photoluminescence reveal details that are screened when only electrical excitation is used due to resistance effects. Future works can take advantage of these experiments as a way of getting more information of carrier dynamics in the active layer without contribution from the p - or n -side. Finally, the addition of an InGaN interlayer (or super-lattice) has a strong impact on these experiments and on the performance of the commercial sample. Further

investigations of current and future modifications to achieve highly efficient devices (interlayers, electron and hole blocking layers, doping of QBs, for example) will also benefit from this methodology because of the additional information that can be obtained regarding the effects of these additions not only under electrical excitation but also in photovoltaic mode.

5.4 Estimation of the doping profile from capacitance - voltage (C-V) measurements

C-V measurements were taken using a frequency of 100 kHz varying the voltage from 0 to -4V. Because we are using reverse bias, only the junction capacitance is taken in this case. Using equations (4.8) - (4.9) that take into account the effect of series resistance, it is possible to get an estimation of the doping profile for all the samples. In figure 5.16-a, -b and -c the results of the carrier concentration versus the width of the depletion layer are shown for the 5QW, 10QW and commercial sample, respectively.

The 5QW sample and 10QW show a smooth curve in the active area with low doping where the QWs should be. The impossibility to resolve individual QWs is related to the Debye length as explained in the previous chapter. Both samples show a value of around $2 \times 10^{18} \text{ cm}^{-3}$ which was the intended n-GaN doping target for these samples. The 10QW sample also shows the *n*-side starting 10 nm later than expected by the measurements. Because the thickness of the layers was checked by X-ray diffraction, it seems unlikely that the reported layers are incorrect. The commercial sample shows a small increase in the carrier concentration between 25 and 50nm which seems to be related with the QWs of these samples. Although the structure of this sample is unknown, from the photoresponse measurements it is expected that this sample has thin QBs that allow carriers to escape. The common width for QWs is usually around 2 - 2.5 nm so it seems possible that in this sample the QW + QB width is of the order of the Debye length. Between around 70 nm and 90 nm there are two peaks that can be seen in figure 5.16-c, these peaks correspond to the edges of the InGaN interlayer that was also measured by PL.

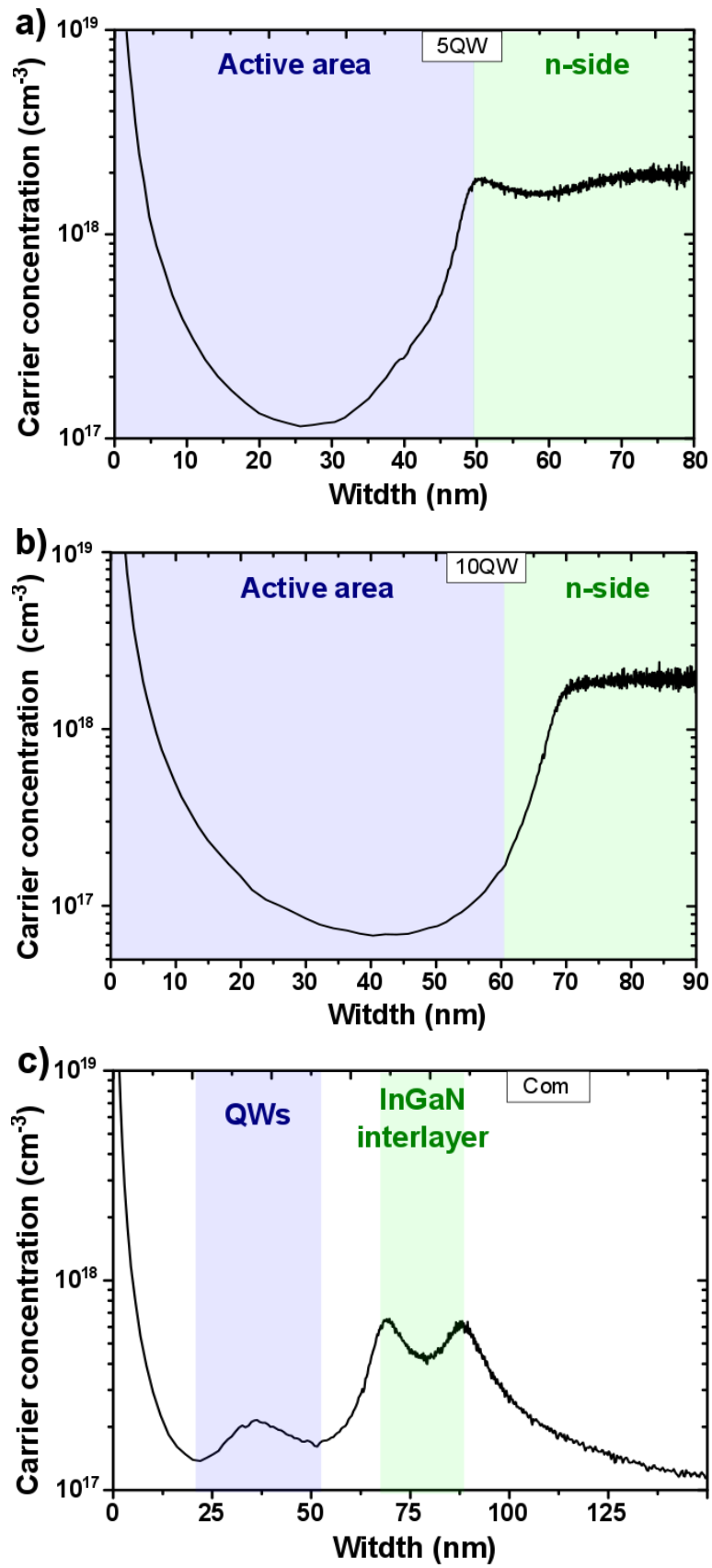


Figure 5.16: Doping profiles for the 5QW, 10QW and commercial samples.

The next measurement on these samples is the capacitance measurement under forward bias. Figure 5.17-a, -b and -c present the results for the 5QW, 10QW and commercial sample respectively. Measurements were done at a range of frequencies, varying from 50 kHz to 2 MHz. The 5QW sample always shows that the negative term starts to dominate around the turn on voltage (~ 2.2 V). Also at around 2.5 V there is a change in the shape of the curves at 50 and 100 kHz which can be related with the change in the resistance reported in sections 5.2 and 5.3. The origin of the negative capacitance seems to be related with carrier recombination in the active layer, so it makes sense to think that both effects can have the same origin, although further work is needed to confirm this. The 10QW sample shows a different behaviour where at low frequencies the capacitance increases monotonously. Again, the curves that show negative capacitance show that this feature appears after the LED turns on. In this case there is no bend at 2.5 V and only at voltages > 3 V it seems to be a change in the reduction of the capacitance which may be related with the effect of the contact resistance as in previous measurements. In addition, there is a strong effect of frequency for voltages > 2.3 V and an absence of a clear peak around 2.2 V. The commercial sample shows a more pronounced peak in the capacitance than the 5QW sample. This sample also shows a strong frequency dependence at voltages > 2.5 , similar to what is observed in the case of the 10QW sample.

Measurements show that the negative capacitance increases with the frequency except in the 5QW sample where there is no clear effect. This contrasts with the behaviour of decreasing negative capacitance with increasing frequency, reported for GaN LEDs by [21, 22]. The reason can be the use of lower frequencies (10 Hz - 100 kHz) in the reports by [21, 22]. This is a significant difference because at higher frequencies it is possible that not all the carriers are able to follow the speed of the signal. Because our current set up does not have the capability of driving the devices at lower frequencies, further work is required to come to a better understanding of the origin of the negative capacitance in our samples.

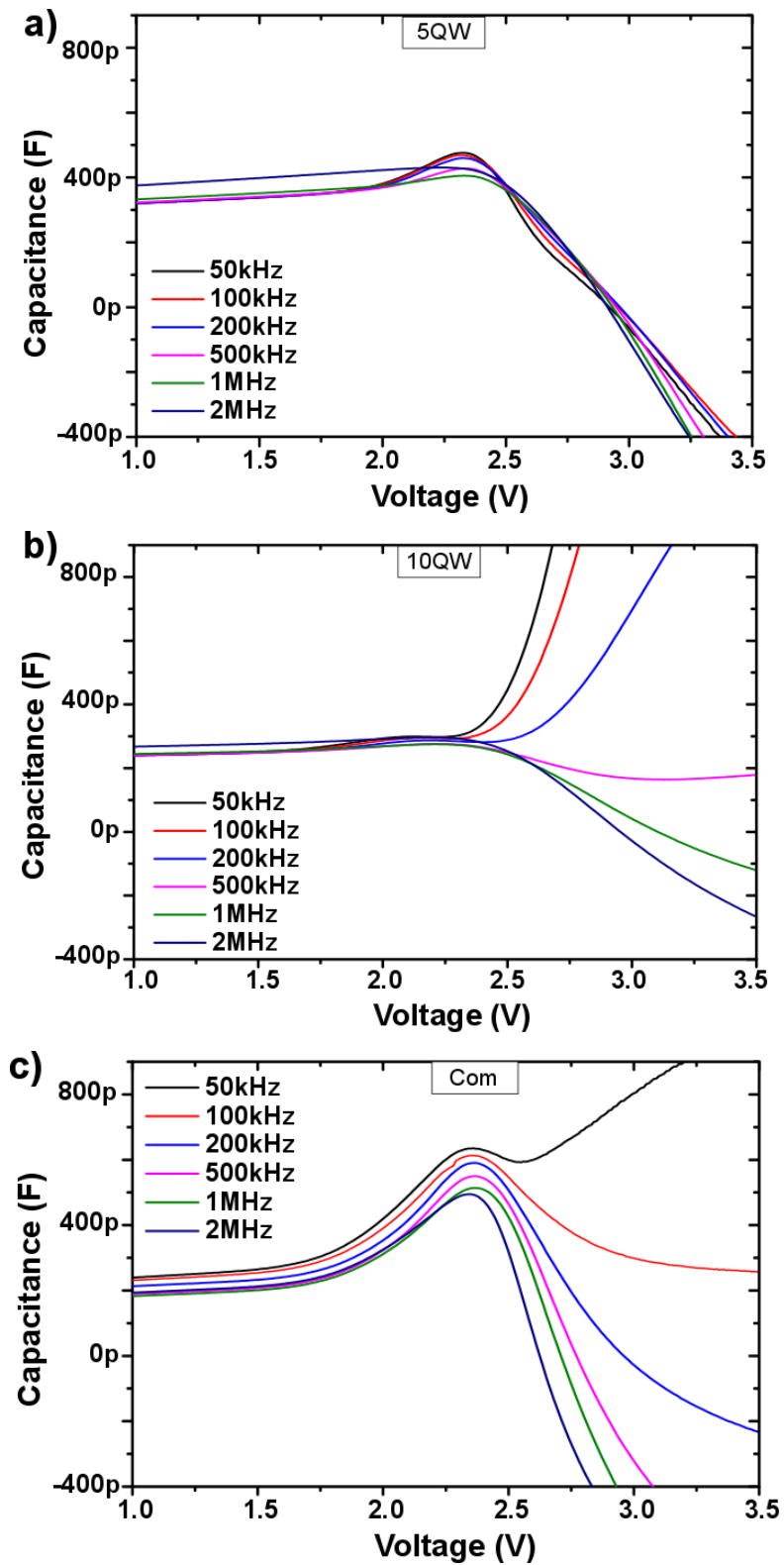


Figure 5.17: C-V measurements at forward bias varying the frequency for a) 5QW sample, b) 10QW sample and c) commercial sample. Negative capacitance is measured in all cases with strong dependency with the frequency.

5.5 – Estimation of the internal quantum efficiency of GaN LEDs using light-current-voltage measurements.

At this point in the thesis the electrical and optical characterization of the LEDs has been explained in detail, yet not much has been said about the internal and external quantum efficiencies of the investigated samples. The estimation of the internal quantum efficiency (IQE) is of special interest because it gives the maximum value for conversion efficiency from electrical current into optical power for a given wafer material, as well as the current density at which this maximum occurs. When current densities higher than 10-20 A/cm² are reached, GaN LEDs suffer a sub-linear increase in the output power. This is a well-known effect usually called ‘efficiency droop’ or just ‘droop’ and despite the literally thousands of publications about it, there is still no general explanation for it [23-25]. A natural explanation of the droop is device self-heating [26]; however, for GaN-based LEDs contributions to the droop from non-thermal mechanisms can be considerable. In fact, carrier overflow and non-radiative Auger recombination have been considered the main processes responsible for the droop [23]. Because the IQE is a key parameter, a quick and reliable method to measure the IQE is required to study this reduction in the efficiency. This chapter presents an analytical method to get an estimation of the IQE as well as the light extraction efficiency (EE) using LIV measurements. The theory is explained in the first part and this is followed by the application of the method and a discussion about the IQE estimation in the second part.

5.5.1 Theoretical background

The ratio between the number of photons generated in the QWs and the total amount of carriers injected into the device is called the IQE. On the other hand, the ratio between the number of photons that are emitted into free space from the sample and the number of electrons injected into the LED per second is called the external quantum efficiency (EQE). These efficiencies are related by the EE which is the ratio between the photons emitted into the free space and the total

amount of photons emitted from the active layer. So, the relationship between these two efficiencies is given by:

$$EQE = EE \times IQE \quad (5.9)$$

In other words, the relationship between the EQE and the IQE is just a scale factor if EE is constant under any injection level. Carrier recombination in GaN LEDs is modelled by the ABC model [23] which uses three basic mechanisms for the recombination of carriers [23, 24], all of them shown schematically in figure 5.18:

- Radiative recombination (blue lines): This is produced when an electron and a hole recombine and a photon is emitted with energy close to the bandgap.
- Non-radiative recombination: In this case the electron energy is transferred as a phonon (vibrational energy of lattice atoms). There are two main non-radiative recombination processes: Shockley-Read-Hall (SRH) recombination (red lines) and Auger recombination (green lines).

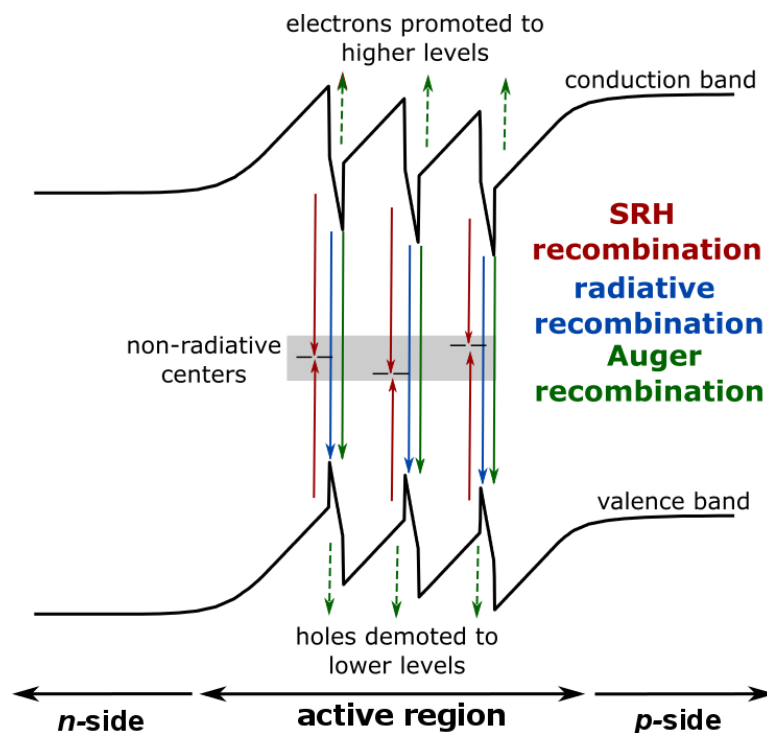


Figure 5.18: Simulated energy bands for a theoretical 3QW structure with the different recombination paths in the QWs highlighted. Red lines indicate SRH recombination, blue lines indicate radiative recombination and green lines indicate Auger recombination.

Radiative recombination requires an electron and a hole, so the recombination rate (R_{rad}) per unit time and per unit area has to be proportional to the concentration of electrons (n) and holes (p):

$$R_{rad} = Bnp \quad (5.10)$$

where the constant B is called the bimolecular recombination coefficient and this relationship is called the bimolecular rate equation. The first non-radiative mechanism is the recombination due to mainly defects in the crystal structure and is called SRH recombination. These defects usually create energy levels inside the forbidden gap of the semiconductor becoming efficient recombination centres as indicated in figure 5.17 by dashed lines in the forbidden gap. SRH is proportional to only the density of electrons or holes. Using the electron concentration, SRH recombination is given by:

$$R_{nrad} = An \quad (5.11)$$

where A is called the SRH recombination coefficient. The next non-radiative recombination mechanism that happens in GaN LEDs is Auger recombination. In this event, an electron and a hole recombine as usual but the energy liberated does not become a photon. Instead, the energy is transferred to another electron which is then excited to a higher energy level, or it goes to a hole which then moves to a higher hole-energy level. Auger recombination is proportional to the concentration of electrons or holes to the power of two, and also proportional to the concentration of the opposite carrier. Auger recombination only becomes important at high excitation levels and the recombination rate can be described in terms of carrier density (n_c) as:

$$R_{Auger} = Cn_c^3 \quad (5.12)$$

Where C is the Auger coefficient. Putting all together, the total recombination rate inside the QWs can be expressed as a function of the carrier density as:

$$R_{Total} = An_c + Bn_c^2 + Cn_c^3 \quad (5.13)$$

Previous definitions can be employed now to find an expression for the IQE using these three coefficients, and yields:

$$IQE = \frac{Bn_c^2}{An_c + Bn_c^2 + Cn_c^3} \quad (5.14)$$

This model is very useful to illustrate the impact of each contribution on the efficiency of LEDs. In a perfect LED where all the carriers recombine radiatively $R_{rad} = R_{TOT}$ and the IQE will be equal to 1 independently of the carrier concentration. This is not possible for a real LED as there will also be some non-radiative recombination due to defects on the crystal. Figure 5.19 shows the effect of different SRH coefficients while maintaining $B = 10^{-11} \text{cm}^3 \text{s}^{-1}$ [27]. Higher defect densities (higher values of constant A), result in a reduction of the IQE at low carrier densities. Once the current density is high enough the SRH recombination saturates, and efficiency approaches 100%.

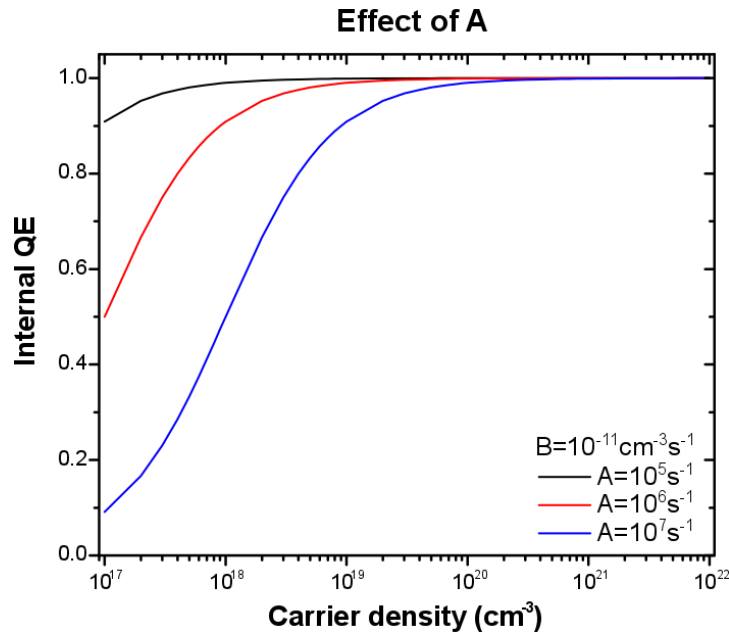


Figure 5.19: Calculated IQE for different values of the SRH recombination coefficient A, and fixed bimolecular recombination coefficient B of $10^{-11} \text{cm}^3 \text{s}^{-1}$ [27]. No Auger recombination is included.

The effect of adding increasing amounts of Auger recombination is shown in figure 5.20. The dependence of the IQE on the value of the Auger coefficient C is displayed, while A and B coefficients are set to common values obtained from the literature: $A = 10^7 \text{s}^{-1}$ [28] and $B = 10^{-11} \text{cm}^3 \text{s}^{-1}$ [27]. Large values of C lead to a

decrease in the maximum achievable IQE and these also reduce the range of carrier densities across which the LED performs optimally.

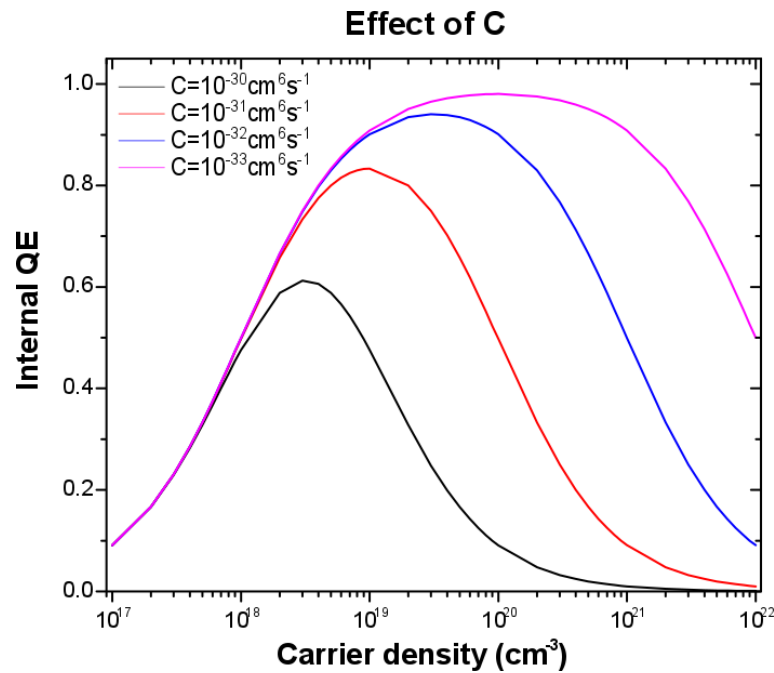


Figure 5.20: Calculated IQE values for different values of the Auger coefficient C . The A and B coefficients were held at $A = 10^7 s^{-1}$ [28] and $B = 10^{-11} cm^3 s^{-1}$ [27].

Auger recombination has been suggested as a likely candidate for the droop effect in GaN LEDs because it reduces the efficiency at high current densities. Yet for the moment, attempts to calculate the Auger coefficient from first principles usually have produced values for the Auger coefficient which are at least a couple of orders of magnitude lower ($C \approx 10^{-32}$ to $10^{-34} cm^6 s^{-1}$) than the value that is required to explain the droop effect ($C \approx 10^{-30} cm^6 s^{-1}$) [23]. Theories aiming to reconcile the smaller C coefficients associated with Auger processes in nitrides with the strong droop have been proposed [29]. One shared assumption is that the effective optically active volume is reduced in comparison with the nominal active volume. This results in increased carrier densities that can make Auger coefficients of the order of $C \approx 10^{-31} cm^6 s^{-1}$ suitable to produce a strong droop.

By measuring light output power as a function of bias current, the EQE can be easily calculated for any device if the wavelength of the emission is known as shown in the following equation (5.15).

$$EQE = \frac{L/h\nu}{I/q} \quad (5.15)$$

Despite its importance, the IQE cannot be measured directly, so it is required to use indirect methods to get an estimation. Because the EE is related to the geometry of the device, one possibility is to estimate the IQE is by studying the geometry of the device and get the percentage of photons than can reach free space. A second possibility explained below is to use the same L-I curve used for the EQE and make a third order polynomial fitting to obtain the maximum of the IQE. Assuming that the EE is constant across the bias current range, this factor can be found by just dividing the maximum of the EQE by the maximum of the IQE. The limitations of this approach will be explained later, yet it is easy to see that using this methodology the IQE can be easily calculated as opposed to using geometrical methods which can be difficult to implement in some cases.

To estimate the IQE then, first the maximum IQE value should be found by differentiating equation (5.14) to find the value of n_c where this maximum occurs, the result is:

$$IQE_{max} = \frac{1}{1 + \sqrt{\frac{4AC}{B^2}}} \quad (5.16)$$

Equation (5.14) relates the A,B and C constants and the carrier density, which is not measured in this case. It is required then to find the relationship between the measured light output power and the carrier density, which is described by:

$$L/(V_{act}h\nu) = EE \cdot Bn_c^2 \quad (5.17)$$

Where V_{act} is the volume of the active layer. This equation can also be re-written as:

$$n_c = \sqrt{\frac{L}{EE \cdot V_{act}h\nu \cdot B}} \quad (5.18)$$

The relationship between the A, B, and C constants and the current density injected into the device is:

$$J/qd_{act} = I/qV_{act} = An_c + Bn_c^2 + Cn_c^3 \quad (5.19)$$

Where d_{act} is the thickness of the active area. By substituting expression (5.18) in (5.19), an equation of the current (density) as a function of \sqrt{L} can be obtained:

$$J/qd_{well} = I/qV_{act} = A\sqrt{\frac{L}{EE \cdot V_{act} h\nu \cdot B}} + B\left(\sqrt{\frac{L}{EE \cdot V_{act} h\nu \cdot B}}\right)^2 + C\left(\sqrt{\frac{L}{EE \cdot V_{act} h\nu \cdot B}}\right)^3 \quad (5.20)$$

From (5.20), using the expression for the current I, three new coefficients A' , B' , C' can be defined as follows:

$$A' = A \frac{V_{act}}{\sqrt{EE \cdot V_{act} B}} \quad (5.21) \quad B' = \frac{1}{EE} \quad (5.22) \quad C' = C \frac{V_{act}}{(\sqrt{EE \cdot V_{act} B})^3} \quad (5.23)$$

These coefficients can be calculated by performing a third order polynomial fit to the $\sqrt{L/h\nu} - I/q$ curve. L and I are already measured to obtain the EQE and all parameters are known, therefore A' , B' and C' can be found by this fitting. It is straightforward to see that replacing A , B and C in equation (5.16) by A' , B' and C' using equation (5.21), (5.22) and (5.23) leads to the same equation in terms of the new coefficients. It is crucial that the fitting is done across the current-range where the device follows the ABC model, if this is not the case, discordances between the original and calculated curves will appear. Finally, while it is possible to extract IQE vs J , and EE , it is not possible to get values for the non-radiative, radiative and Auger recombination coefficients A , B , and C with this method alone, since it is not possible to distinguish between the contribution of B and the contribution on n^2 to the light output.

5.5.2 Estimation of quantum efficiency and extraction efficiency

One of the outcomes of all the data presented in chapter 5 is that the commercial sample has a strong resemblance with an ideal diode. Although the contact resistance hides the expected value close to 1 for the n_{elect} , measured n_{ph} , n_{pv} and n_{pl} indicate that this is indeed a good sample dominated by radiative recombination and therefore a reasonably high efficiency can be expected. On the other hand, the 5QW and the 10QW samples have significant non-radiative recombination and we may therefore expect a lower efficiency for these samples than for the commercial sample.

The aim of this section then is to use the method presented in this chapter to estimate the IQE of these samples and to check the correlation with the previous measurements. Figure 5.21 shows the results after direct application of the method using a program written in Python and included in the Appendix A of this thesis. Continuous lines in figure 5.21 indicate the IQE calculated using the measured EQE divided by the calculated EE. So the shape of these curves is completely determined by the L-I measurements. Dotted lines indicate the IQE calculated using the fitted parameters A' , B' and C' . As said before, a small range of points is sufficient to replicate the entire curve, which gives a fitting criterion: if a range of points that replicates the EQE/EE - I curve as in the case of the commercial sample (blue lines in figure 6.4) can be found, the fitting can be trusted. On the other hand, if no range can be found that meets this criterion, then it is not possible to perform the estimation of the IQE on such a sample.

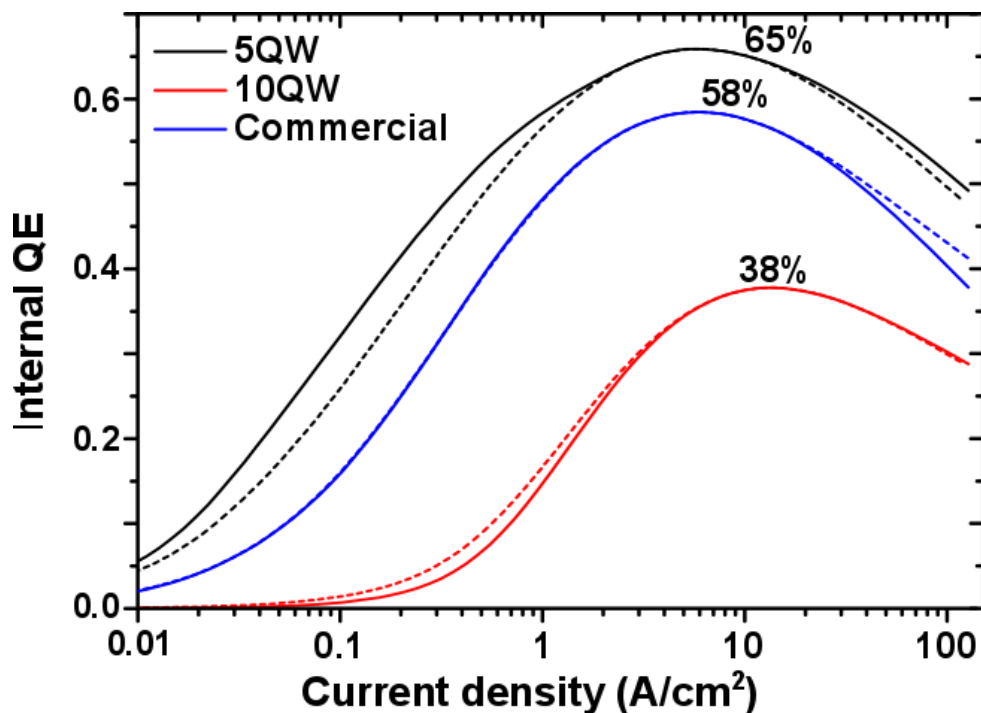


Figure 5.21: IQE as a function of current density for the 5QW, 10QW and commercial samples. Continuous lines: measured EQE values, divided by the EE value obtained from 6.13. Dotted lines: IQE values calculated from fitted A' , B' , and C' parameters.

The calculated IQE curves in figure 5.21 do not correlate well with all our previous measurements where there is not a single indication that the 5QW sample could be more efficient than the commercial sample. Nor the amount of light emitted nor the transport mechanisms discussed in chapter 5 indicate that this result is plausible. These discrepancies come from the deviation of the 5QW and 10QW samples from an ideal diode: for the commercial sample, blue lines in figure 6.4 shows almost no discrepancy between both curves, in other words, fitted coefficients are able to replicate the measured EQE (continuous line) except at current densities $> 30 \text{ A/cm}^2$, which will be analysed later. This is not the case for the other two samples because both show significant differences between the measured EQE vs. j shape and the calculated one, using the fitted A' , B' and C' values, indicating that the A' - B' - C' model does not describe the processes within these samples very accurately. This is an important result that follows on from one of the conclusions from chapter 5: uniform and efficient devices resemble ideal diodes, therefore the ABC model is here a helpful tool to estimate the IQE. On the other hand, for non-optimized samples, this is not only incorrect but also could lead to misleading results. This is why it is important to select a range where the sample can be well described by the ABC model, that is, when it resembles closely an ideal diode. This is not always possible for non-ideal samples such as our 5QW and 10QW samples.

To check the reliability of the method, the IQE of the commercial sample was measured by an independent group in OSRAM OS using a similar ABC fitting methodology. The reported values of the IQE-maximum for the sample varied between 60 to 65%. These values are slightly bigger than the 58% obtained here and the reason could be that this estimation was done using a different set of contacts in the same sample.

Once the method is validated for the commercial sample, there is still interest in getting an estimate of the IQE_{max} values for the other two samples. The result from the commercial sample gives the possibility to obtain this because all three samples had the same contact geometry and were also evaluated with the same measurement set-up under the same conditions. Therefore, the experimental procedure employed allows us to assume that all three samples have the same

light extraction efficiency. Figure 5.22 shows the result when all three measured EQE vs. J curves have been corrected with the same EE factor of 2.4%. This EE factor comes from the A'-B'-C' fit to the curve of the commercial sample and was calculated using equation (5.22). Estimated maximum IQE values are 43%, 24% and 58% for the 5QW, 10QW and commercial samples, respectively. The ranking of these samples is now in agreement with our previous analysis.

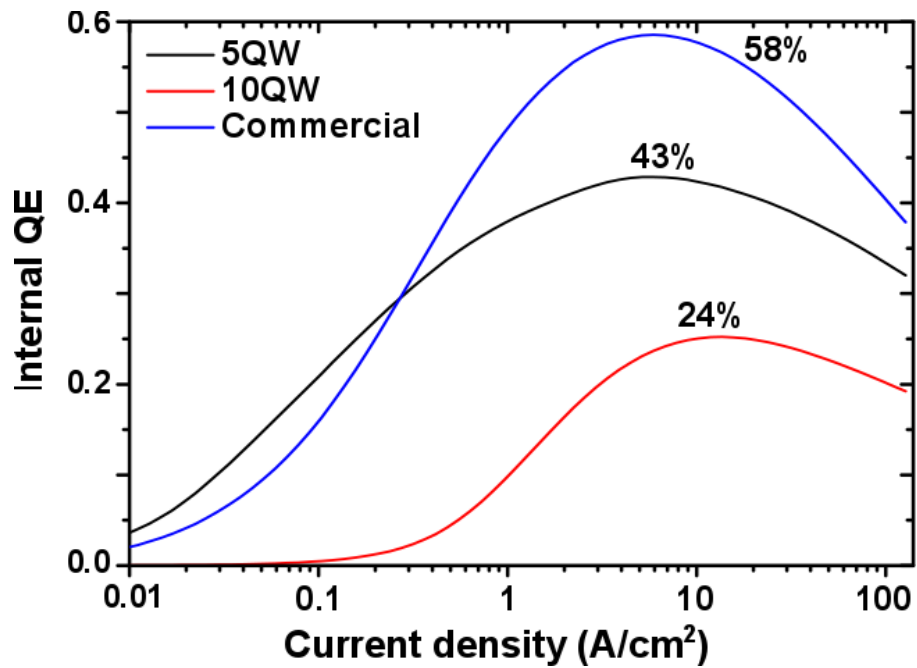


Figure 5.22: Calculated IQE curves for the 5QW, 10QW and commercial samples using measured EQE curves and a fixed EE factor, determined by A'-B'-C' fitting to the commercial sample (EE=2.4%) due to geometrical considerations.

As previously indicated, it is not possible to distinguish between the contribution of B and n_c , therefore there is no way of finding the actual A, B and C values. However, the value of B has been reported extensively in the literature (for example in [23] and [27]) as to be close of $B = 10^{-11} \text{ cm}^3\text{s}^{-1}$. It is possible to use this value to obtain A value and C for all samples. Table 5.2 below shows the calculated values for all the samples:

Table 5.2: Calculated values of A and C for all the samples using $B = 10^{-11} \text{ cm}^3\text{s}^{-1}$

Sample	$A \text{ (s}^{-1}\text{)}$	$C \text{ (cm}^6\text{s}^{-1}\text{)}$
5QW	$3.6 \cdot 10^6$	$1.1 \cdot 10^{-29}$
10QW	$9.1 \cdot 10^6$	$2.4 \cdot 10^{-29}$
Commercial	$2.2 \cdot 10^6$	$5.7 \cdot 10^{-30}$

Values from table 5.1 show that non-radiative recombination is lower on the commercial sample, which could be expected due to its higher efficiency. The 10QW has a value of A more than 2.5 times the same value in the 5QW sample, which is in agreement with previous results that indicate higher non-radiative recombination. Values obtained for the Auger constant are quite high for all samples, and specially for the 5QW and 10QW samples. Different reasons could lead to this:

1. An additional unknown physical mechanism has a strong effect when current density is increased and the ABC model just assumes that is Auger recombination.
2. As introduced before, the optical active volume is smaller than the assumed active volume. Therefore current densities are expected to be larger than the ones in figure 6.5 and C values required for the droop given by the EQE curve are smaller.
3. The assigned value of B from literature is not correct for our samples and the real value is lower. In this case non-radiative recombination at high current density does not need to be as high as the one given by our calculation to produce the same amount of droop.

Finally, a comment about the discrepancy between measured and calculated IQE curve shapes in figure 5.21 has to be made now to understand why the estimation of the IQE using this method requires careful examination: additional physical mechanisms not taken into account in our model have an impact on the shape of the EQE curve. In figure 5.21, at values higher than 10 A/cm^2 there is a discrepancy between experiment and A-B-C theory for all curves. The reason is that beyond a certain current density there is an additional mechanism that is not

covered by the A-B-C model. This discrepancy at high current densities has been widely observed and investigated although so far there is not a widely accepted theory that describes the device behaviour in this regime [23-25]. To estimate the IQE with the method described above, points measured at high current densities have to be excluded for the fitting to be valid.

Also, the assumption made here that the EE at low current densities is the same for all the samples is reasonable for the samples used in this work but may not be true for all cases: the degree of surface roughness on the back surface, and the emission profile from the QWs are not necessarily the same for two different samples and the emission profile may also be stress dependant. If samples do not have the same emission profile, then is not possible to assume that they share the same EE value and the analysis done here may be incorrect.

5.6 – Summary of all presented results

This chapter began with the introduction of two different observations for the 5QW and 10QW samples without a satisfactory explanation: the first one was the low turn on voltage of around 2.2 V (shown in figure 5.10) and the second one the yellow band emission from both of these samples (shown in a fluorescence image in figure 5.1 and by the spectrum in figure 5.8). After the study of these samples with a combination of electrical and optical excitation, results indicate that both results have a common origin: the yellow emission comes from the MQW region and is associated with traps in the QBs. Under optical excitation with 405 nm light, there is absorption in these defects across a wide range of energies and reemission is dependent only on the optical power. This reemission also shows a wide range of energies producing the wide YB.

Under electrical excitation some of these defects will play a role as well providing light at low voltages: defects deep in the bandgap (related to the longer wavelengths of the YB under optical excitation) will not be affected by the change in bias, yet defects that are closer to the valence/conduction band would promote hole and electron tunnelling. Enhanced tunnelling explains both the high ideality

of these samples and the emission of light at low voltages. This is because movement of carriers through the MQW region due to tunnelling has two different outcomes: carriers may reach the opposite side (p-region for electrons and n-region for holes) producing current or carriers may be trapped in a QW and recombine, emitting a photon.

The 5QW and 10QW samples do not have additional layers that prevent injection of carriers at low current densities as in the case of the commercial sample. Because of this, carriers will start to flow to the MQW region at lower voltages than in the case of the commercial sample. In general, carriers will end trapped in the closest QW from the region where they are majority carriers. Because these QWs are also the farthest for the opposite charged carriers, only one type of carrier can be found in these QWs and no radiative recombination is expected. However, as the bias is increased, the enhanced tunnelling will allow some carriers to populate further QWs and even reach the opposite side. From figure 5.3 it can be seen that both samples show current even at voltages around 1.3 V, which means that carriers are able to travel through the entire active region. Because in the case of the 10QW sample QWs are thinner than the 5QW, increased tunnelling is expected, the result is more current flowing at low voltages and QWs more populated with both kind of carriers allowing some radiative recombination.

Figure 5.10 shows the emission of light at low voltages, which indicates that some carriers have been trapped inside the MQW region and start to recombine. In this case, although the 10QW has increased tunnelling current, the difference is small due to several factors: first of all, SRH recombination is bigger for this sample (as seen by the YB and with the IQE estimation) and the fastest one so an important part of the carriers will recombine non-radiatively. Second, the higher number of QWs also makes it more difficult for carriers to get trapped in QWs that are also populated with opposite carriers.

Fluorescence microscopy has proven to be a very useful resource for quick characterization of unprocessed and fully processed GaN LEDs. Because of the photovoltaic effects that happen inside these LEDs, a quick imaging of the

metallized contacts can help to discern between good and bad contacts without the need to perform an electrical characterization of the individual contacts. This comes from the generation of the photovoltage V_P under optical illumination. Because this V_P is shared under the metal surface, under the presence of defects or shunting paths under the metal contact, this voltage will be reduced and the emission under fluorescence of the contact as well. So a mapping of the metallized LEDs under fluorescence will show in some cases dimmer metal contacts that correspond to worse electrical behaviour. If this process is applied to full wafers, a high quality wafer will then show a high yield and uniform emission from almost all contacts. On the other hand, a lower quality LED wafer will show high disparity between the emission from contacts. This methodology can also be applied to identify defects and problems during manufacturing processes. In this work it has allowed us to identify the best contacts specially in the 5QW and 10QW samples. Therefore this assures that selected contacts where experiments were performed are good representatives of the sample and do not show additional effects.

Further experiments with resonant optical excitation allowed the study of the differences between the internal piezoelectric fields between the 5QW and 10QW samples. These differences again come from thicker barriers in the case of the 5QW which leads to larger piezoelectric fields across the QWs and a lower field across the barrier when compared to the 10QW sample. The weaker field in the QB of the 5QW together with the greater barrier thickness results in an increased confinement of carriers due to the combination of the confinement potential of QWs and QBs. The study of the spectra under electrical excitation indicates an equilibrium between the change of polarization field and the increase of carrier density in the 5QW because no wavelength shifts are seen. This is in contrast with the 10QW sample that shows a blue shift with increasing voltage. Under combined optical and electrical excitation the 5QW does show a suppression of the longer wavelengths due to changes of the piezoelectric field at the bottom of the QW while the 10QW does not show any effect regarding the piezoelectric field from the QW and just shows a decrease of the emission intensity with the reduction of the bias due to decreasing carrier density.

Ideality factors studied in section 5.4 and summarized in table 5.1 provide information about the carrier transport outside the intrinsic region of the diodes. The 5QW and 10QW samples show a greater reduction between the electrical ideality factors and the ones from photovoltaic measurements or by radiative current than the commercial sample. This indicates that both of them have several contributions from additional voltage drops that hide the junction voltage. Because dominant recombination mechanisms are different, these values are different, however, the reduction of the ideality factor seems to be quite similar. This is probably due to the fact that the material surrounding the active area should be very similar for both samples, although it should not be forgotten that the p-side is thinner in the case of the 10QW sample and it can be expected that the quality may differ after the growth of the additional MQW structure.

When ideality factors from 5QW and 10QW samples are compared, the minimum values always belong to the 5QW and can be related to the higher efficiency. This has been a constant result from all the experiments and was also confirmed by the IQE estimation. At low current densities when Auger recombination does not have to be taken in account, radiative recombination is the mechanism that is related to the lower ideality factor of 1. Highly efficient samples as the commercial sample studied here are expected to mainly show this type of recombination, therefore when current transport outside the intrinsic region is avoided (as in photovoltaic measurements) the ideality factor is always close to 1. In the case of the 5QW and 10QW samples there are additional mechanisms that increase the value of the ideality factor. Despite the fact that the value of 2 for the ideality factor is usually identified as SRH recombination; in this case it seems like this assumption could be incorrect even in the case of the 5QW sample where ideality factors from photovoltaic measurements are close to 2. In fact, the IQE estimation in section 5.5 does not indicate a strong difference between this sample and the commercial sample regarding the SRH coefficient A . The ideality factor close to 2 could also be the result of the tunnelling current that also exists in this sample that has been identified as the origin of emission at low voltages and to the YB in this sample. This is not to say that SRH recombination does not

have an important role in this sample, but to point out that this may not be the dominant mechanism while tunnelling plays a more important role as other measurements indicate.

Furthermore, the 5QW sample shows a distinct break in its photovoltage characteristics which indicates a change in the radiative recombination rate. SRH recombination comes from defects so it is highly unlikely to be related with this effect. This shows yet another difference between internal mechanism between these two samples: while the 10QW seems to have a single dominant mechanism for the range of voltages shown, the 5QW has a transition where two different mechanism are dominant below and above 2.4 V.

In addition, the multiple competing mechanisms in these LEDs makes the application of the presented methodology using a combination of resonant optical and electrical excitation very important to get a full picture of all the processes involved. The studied commercial sample resembles an ideal diode but this is not true for the 5QW and 10QW samples. This implies that the application of electrical excitation alone cannot reveal all the differences in the recombination processes: for example, high electrical ideality factor is often related to a product of increased tunnelling due to the reduction of the QB thickness. However, this will be only partially true because it is thought to be the combination of enhanced tunnelling, lower carrier confinement and higher nonradiative recombination that makes the 10QW sample less efficient than the other samples. As indicated by photoresponse measurements, in the 10QW sample carriers can leave the QWs more efficiently than in the 5QW sample, so the sample generates more current but does not emit more light. This is because the 5QW sample has increased confinement, which means longer carrier lifetime to stay in the QWs and recombine emitting a photon. Adding to this that the YB is stronger in this sample, which has been related to the number of defects: these are the main reasons for the lower efficiency of the 10QW sample.

All the experiments listed in this thesis and done to characterize these samples show one of the most interesting findings in this thesis. The 5QW and 10QW samples are quite similar regarding dopants and growth conditions with the

main differences being the number of QWs and the thickness of the barriers. These seemingly small changes however result in a completely different performance, not only from the electrical point of view but also in the optical characteristics of the emission under different excitation modes.

Finally, although it may seem logical to establish a classification of the samples based on their efficiency or quality. Without knowing the final application this could lead to the false assumption that some of the samples are less suitable due to a lower efficiency. As will be shown now, the LEDs studied here have shown a wide array of different properties which makes each one of them suitable candidates for very different applications. For example, for general lighting applications where the maximum light output is the main parameter to be taken in account, all the information gathered in this thesis shows clearly that the commercial sample is the better candidate due to its higher efficiency. It is then followed by the 5QW and by the 10QW sample which has the lowest efficiency of all samples.

However, it is possible to imagine an application where the output wavelength should be as constant as possible. In this situation, the 5QW sample will be the best candidate due to the compensation between the effect of the piezoelectric field in the QW and the modification of the carrier density inside the QW when changing applying bias. As seen in figure 5.7, the change in wavelength for this samples is within 4 nm while the other two samples had a stronger blue shift.

Finally, the 10QW sample has a possible application as well. From the L-V characteristics presented in figure 5.10 this sample is more appropriate than the other two for low light and low power applications where the requirements are to have light at the lowest possible bias voltage. Despite its lower efficiency at higher voltages, this sample emits more light for voltages up to 2.35V, caused by the easy flow of carriers to more remote QWs due to enhanced tunnelling through its thinner barriers.

Chapter 6 - Conclusions and recommendations for future work

This thesis has presented a comprehensive study of the emission spectra and electrical characteristics of InGaN/GaN LEDs. A range of characterization methodologies have been introduced to unravel the different mechanisms for the recombination of carriers in GaN LEDs. To make this possible, experimental set ups that now can be used more widely to analyse LED wafer materials and devices had to be designed and built.

A main point in this work is that the addition of resonant optical excitation to electrical excitation to the samples has proven to be a useful technique to study different effects in GaN LEDs: differences in piezoelectric fields in the samples, carrier escape with the associated photovoltaic effect under open and short circuit conditions, and different voltage ideality factors have been extracted and compared. Also, fluorescence microscopy has been shown to be a valuable imaging technique to reveal spatially dependent characteristics of InGaN based LED materials and devices. One important fact proven in this thesis is that the effect of carrier escape should not be neglected when interpreting photoluminescence measurements: under open-circuit (OC) conditions carrier escape causes the generation of a local photovoltage, which forward biases the p-n junction; under short-circuit (SC) conditions the luminescence is strongly reduced due to effective carrier escape. The strong lateral variations in the emission due to non-uniform materials growth (and materials processing) mean that 1-dimensional analyses of carrier transport need to be treated with caution. The fluorescence microscopy technique has proven to be a very useful and quick evaluation method for unprocessed LED materials and it allows the evaluation of fabrication steps such as etching through light emitting layers without the need of probing the sample.

In chapter 5, the investigation of the effect of a change in the thickness of the quantum barrier (QB) from 6.6 nm to 4 nm (while simultaneously increasing the number of quantum wells from 5 to 10) in the active region of InGaN/GaN LEDs was presented and discussed. This seemingly small change has led to significant

differences in the carrier transport and light emission characteristics of the two epitaxial designs. These differences were compared with a reference LED material which showed a different behaviour again. The 10QW sample draws more current at low voltage which we ascribe to trap-assisted tunnelling of holes associated with the low-temperature grown barriers and the fact that the barriers themselves are thinner. These traps assist in carriers entering the quantum well at low voltages resulting in the ideality >1 for light emission and consistently being the highest among the three samples measured. The thin barriers also assist in the extraction of carriers in the photovoltaic mode. The spectral properties are dominated by band filling as opposed to piezoelectric effects suggesting the piezoelectric interface charge is less than for the 5QW sample. The 5QW sample with the thicker barriers shows features in the emission spectra that are associated with a strong piezoelectric field in the quantum well suggesting that the interface charge is large in this case. Partial trapping of carriers is measured in forward bias with carriers entering (current injection) and leaving (photovoltaic mode) the QW region. The light-related idealities for the 5QW and 10QW samples are > 1 suggesting non-radiative recombination in the QWs and especially for the 10QW sample. The commercial sample has values for n_{light} , n_{pv} and n_{pl} , each being close to one suggesting minimal non-radiative recombination. The higher (apparent) electrical ideality factor seems to be due to carrier transport external to the QW region at low voltages and due to resistive effects at higher voltages. An InGaN underlayer is shown to affect the optically pumped measurements of the ideality (n_{pv} , n_{pl}) due to the generation of additional carriers. This seems to be the possible explanation for the resulting extracted idealities being lower than 1.

All the techniques along with the methodology explained in this thesis will help in the optical and electrical characterization of new GaN-based materials and devices. The following are suggestions for further work:

- Research on semi-polar and non-polar GaN samples: first steps in the measurement of the photocurrent and the increase of the peak of the emission under resonant excitation have already shown surprising results. In semi-polar samples carriers seem to get trapped in an additional

confinement state that happens around 1.5 V. The origin and characteristics of this effect are unknown at the moment although they seem to confirm the reduction or suppression of electric fields in these samples. Despite the fact that still more work has to be done to complete the characterization of these samples, this serves as an example of the usefulness of the methodology presented here.

- Systemic optimization of new epitaxial LED structures, this usually involves one or more of the following: the addition of new layers, change in layer thicknesses or change in growth methodology. Changes can be subtle and may have a strong impact on device performance.

The study of samples using resonant optical and electrical excitation would not be complete without further studies of the capacitance of these devices. In this work only a brief study of the depletion capacitance has been presented, yet several possibilities come to mind for follow-on experiments:

- Investigation of the C-V characteristics under resonant illumination: previous publications claim that non-uniform accumulation of carriers by the additional laser excitation can be observed. It would be of great interest to study this in c-plane, semi-polar and non-polar GaN samples.
- Strong interest has the analysis of the negative capacitance, especially for non-optimized samples. There is no current explanation for the results presented in this work and that alone is reason enough for further work. A detailed investigation of the diffusion capacitance should lead to a deeper insight into internal carrier dynamics. This could lead to further knowledge of the basic principles that rule GaN LEDs.

In conclusion, this thesis presents another step towards a better understanding of GaN-based LEDs. The importance of this work is that it provides additional experimental tools to gain further insight of carrier dynamics in GaN LEDs, which in turn is required to maximize the performance of these devices.

Bibliography

Chapter 1 - Introduction

- [1] H. J. Round, "A note on carborundum", *Electrical World*, 49, 309 (1907)
- [2] E. Fred Schubert, "Light Emitting Diodes", Sec. Ed. Cambridge University Press (2006)
- [3] O.W. Lossew, "Wireless Telegraphy and Telephony", *Telegrafia i Telefonija bez provodor*, 18, 61 (1923)
- [4] G. Destriau, "Scintillations of zinc sulfides with alpha-rays", *J. Chimie Physique* 33, 587 (1936)
- [5] J. Bardeen and W. H. Brattain, "The transistor, a semi-conductor triode", *Phys. Rev.* 74, 230 (1948)
- [6] E.E. Violin, A.A. Kalnin, V.V. Pasyukov, Y.M. Tairov, and D.A. Yaskov, "Silicon Carbide - 1968", *Materials Research Bulletin*, 231 (1969)
- [7] R. M. Potter, J. M. Blank, and A. Addamiano, "Silicon carbide light-emitting diodes", *J. Appl. Phys.* 40, 2253 (1969)
- [8] H. Welker, "On new semiconducting compounds", *Zeitschrift für Naturforschung* 8a, 248 (1953)
- [9] M.I. Nathan, W.P. Dumke, G. Burns, F.J. Dill, and G.J. Lasher, "Stimulated emission of radiation from GaAs *p-n* junctions", *Appl. Phys. Lett.* 1, 62 (1962)
- [10] N. Holonyak Jr., and S.F. Bevacqua, "Coherent (visible) light emission from Ga(As_{1-x}P_x) junctions", *Appl. Phys. Lett.* 1, 82 (1962)
- [11] J.A. Edmond, H.S. King, and C.H. Carter, "Blue LEDs, UV photodiodes and high-temperature rectifiers in 6H-SiC", *Physica B: Cond. Matt.*, 185, 453 (1993)
- [12] N. C. Chen, W. C. Lien, Y. K. Yang, C. Shen, Y. S. Wang, and J. F. Chen, "Spectral shape and broadening of emission for AlGaInP light-emitting diodes", *J. Appl. Phys.* 106, 074514 (2014)
- [13] N. K. Dhar, R. Dat and A. K. Sood, "Advances in Infrared Detector Array Technology, Optoelectronics - Advanced Materials and Devices", Prof. Sergei Pyshkin (Ed.), InTech, Chapter 7 (2013)
- [14] R. Juza and H. Hahn, "On the crystal structure of Cu₃N and InN", *Zeitschrift fuer anorganische und allgemeine Chemie* 239, 282 (1938)

- [15] H. P. Maruska and J. J. Tietjen, "The preparation and properties of vapour-deposited single-crystalline GaN", *Appl. Phys. Lett.* 15, 327 (1969)
- [16] J. I. Pankove, E. A. Miller and J. E. Berkeysheiser, "GaN electroluminescent diodes", *RCA Review* 32, 383 (1971)
- [17] H. Amano and I. Akasaki, "Fabrication and properties of GaN *p-n* junction LED", *Mater. Res. Soc. Extended Abstract*, 165 (1990)
- [18] S. Nakamura, M. Senoh, and T. Mukai, "Highly *p*-type Mg doped GaN films grown with GaN buffer layers", *Jpn. J. Appl. Phys.*, 30, L1708 (1991)
- [19] S. Nakamura, M. Senoh, and T. Mukai, "*p*-GaN/*n*-InGaN/*n*-GaN double-heterostructure blue light-emitting diode", *Jpn. J. Appl. Phys.*, 32, L8 (1993)
- [20] S. Nakamura, M. Senoh, and T. Mukai, "*p*-GaN/*n*-InGaN/*n*-GaN double-heterostructure violet light-emitting diode", *Appl. Phys. Lett.*, 62, 2390 (1993)
- [21] S. Nakamura, M. Senoh, N. Iwasa, S. Nagahama, T. Yamada, and T. Mukai, "Superbright green InGaN single-quantum-well-structure light-emitting diodes", *Jap. J. Appl. Phys.* 34 (2), 10B (1995)
- [22] Nobel prize website (2014 physics laureates:
https://www.nobelprize.org/nobel_prizes/physics/laureates/2014/
- [23] M. R. Krames, O. B. Shchekin, R. Mueller-Mach, G. O. Mueller, L. Zhou, G. Harbers, and M. G. Cradford, "Status and future of high power light emitting diodes for solid state lighting", *J. Display Tech.*, 3 (2), (2007)
- [24] T. Mukai, M. Yamada, and S. Nakamura, "Characteristics of InGaN UV/Blue/Green/Amber/Red light-emitting diodes", *Jpn. J. Appl. Phys.*, 38, 3976 (1999)
- [25] S. Pleasants, "Overcoming the 'green gap'", *Nat. Phot.*, 7, 585 (2013)
- [26] E. Zanoni, M. Meneghini, N. Trivellin, M. Dal Lago and G. Meneghesso, "GaN-based LEDs: state of the art and reliability-limiting mechanisms", 15th International conference on Thermal, Mechanical and Multi-Physics simulation and experiments in Microelectronics and Microsystems, EuroSimE 2014
- [27] J. Piprek, "Efficiency droop in nitride-based light-emitting diodes", 207 *Phys. Stat. Solidi*, (10), 2217, (2010)
- [28] J. Cho, E. F. Schubert, and J. K. Kim, "Efficiency droop in light-emitting diodes: challenges and countermeasure", *Laser Phot. Rev.*, 7 (3), 408 (2013)

[29] A. David, and N. F. Gardner, "Droop in III-nitrides: comparison of bulk and injection contributions", *Appl. Phys. Lett.*, 97, 193508 (2010)

Chapter 2 – Introduction to the Gallium Nitride system

[1] V. Y. Davydov, A. A. Klochikhin, R. P. Seisyan, V. V. Emtsev, S. V. Ivanov, F. Bechstedt, J. Furthmüller, H. Harima, A. V. Mudryi, J. Aderhold, O. Semchinova, and J. Graul, "Absorption and emission of hexagonal InN. Evidence of narrow fundamental band gap", *Phys. Stat. Sol. (b)* 229 (3), R1 (2002)

[2] Y. Narukawa, M. Ichikawa, M. Sano, and T. Mukai, "White light emitting diodes with super-high luminous efficacy", *J. of Phys. D: Appl. Phys.*, 43, 354002 (2010)

[3] L. J. Lin, Z. J. Li, W. G. Xu, M. C. Lan, X. L. Quan, D. Jie, Q. Z. Jue, W. X. Lan, P. Shuan, Z. C. Da, W. X. Ming, F. W. Qing, and J. F. Yi, "Status of GaN-based light emitting diodes", *Chin. Phys. B* 24 (6), 067804 (2015)

[4] H. K. Cho, J. Y. Lee, J. H. Song, P. W. Yu, G. M. Yang and C. S. Kim, "Influence of strain-induced indium clustering on characteristics of InGaN/GaN multiple quantum wells with high indium composition", *J. Appl. Phys.*, 91, 1104 (2002)

[5] Y. Zhao, Q. Yan, C. Y. Huang, S. C. Huang, P. S. Hsu, S. Tanaka, C. C. Pan, Y. Kawauchi, K. Fujito, C. G. Van de Walle, J. C. Speck, S. P. DenBaars, S. Nakamura, and D. Feezell, "Indium incorporation and emission properties of nonpolar and semipolar InGaN quantum wells", *Appl. Phys. Lett.* 100, 201108 (2012)

[6] V. Fiorentini, and F. Bernardini, "Effects of macroscopic polarization in III-V nitride multiple quantum wells", *Phys. Rev. B* 60 (12), 8849 (1999)

[7] Y. C. Shen, G. O. Mueller, S. Watanabe, N. F. Gardner, A. Munkholm, and M. R. Krames, "Auger recombination in InGaN measured by photoluminescence", *Appl. Phys. Lett.* 91, 141101 (2007)

[8] M. H. Kim, M. F. Schubert, Q. Dai, J. K. Kim, E. F. Schubert, J. Piprek, and Y. Park, "Origin of efficiency droop in GaN-based light-emitting diodes", *Appl. Phys. Lett.* 91, 183507 (2007)

[9] J. Piprek, "Efficiency droop in nitride-based light-emitting diodes", *Phys. Status Solidi A* 207 (10), 2217 (2010)

[10] P. Waltereit, O. Brandt, A. Trampert, H. T. Grahn, J. Menniger, M. Ramsteiner, M. Reiche, and K. H. Ploog, "Nitride semiconductors free of

electrostatic fields for efficient white light-emitting diodes”, *Nature* 406, 865 (2000)

[11] G. Kozlowsky, B. Corbett and S. Schulz, “Color stability, wave function overlap and leakage currents in InGaN-based LED structures: the role of the substrate orientation”, *Sem. Sci. and Tech.*, 30, 055014 (2015)

[12] H. P. Maruska and J. J. Tietjen, “The preparation and properties of vapor-deposited single-crystalline GaN”, *Appl. Phys. Lett.* 15, 367 (1969)

[13] B. C. Chung, and M. Gershenson, “The influence of oxygen on the electrical and optical properties of GaN crystals grown by metalorganic vapor phase epitaxy”, *J. Appl. Phys. Lett.* 72, 651 (1992)

[14] J. D. Guo, C. I. Lin, M. S. Feng, F. M. Pan, G. C. Chi, and C. T. Lee, “A bilayer Ti/Ag ohmic contact for highly doped *n*-type GaN films”, *Appl. Phys. Lett.* 68, 235 (1996)

[15] H. Amano, I. Akasaki, K. Hiramatsu, N. Koide, N. Sawaki, “Effects of the buffer layer in metalorganic vapour phase epitaxy of GaN on sapphire substrate”, *Thin solid films*, 163, 415 (1988)

[16] D. Kapolnek, X. H. Wu, B. Heying, S. Keller, B. P. Keller, U. K. Mishra, S. P. DenBaars and J. S. Speck, “Structural evolution in epitaxial metalorganic chemical vapor deposition grown, GaN films on sapphire”, *Appl. Phys. Lett.* 67, 1541 (1995)

[17] S. D. Lester, F. A. Ponce, M. G. Craford, and D. A. Steigerwald, “High dislocation densities in high efficiency GaN-based light-emitting diodes”, *Appl. Phys. Lett.* 66, 1249 (1995)

[18] R. W. Hutchinson, and P. S. Dobson, “Defect structure of degraded GaAlAs/GaAs double heterojunction lasers”, *Philos. Mag.* 32, 745 (1975)

[19] D. V. Lang, and C. H. Henry, “Nonradiative recombination at deep levels in GaAs and GaP by lattice-relaxation multiphonon emission”, *Phys. Rev. Lett.* 35, 1525 (1975)

[20] S. Tomiya, E. Morita, M. Ukita, H. Okuyama, S. Itoh, K. Nakano, and A. Ishibashi, “Structural study of defects induced during current injection to II-VI blue light emitter”, *Appl. Phys. Lett.* 66, 1208 (1995)

[21] X. A. Cao, P. M. Sandvik, S. F. LeBeouf, and S. D. Arthur, “Defect generation in InGaN/GaN light-emitting diodes under forward and reverse electrical

- stresses”, *Microelectron. Reliab.* 43 (12), 1987 (2003)
- [22] A. Uddin, A. C. Wei, and T. G. Andersson, “Study of degradation mechanism of blue light emitting diodes”, *Thin Solid Films*, 483 (1/2), 378 (2005)
- [23] T. Hino, S. Tomiya, T. Miyajima, K. Yanashima, S. Hashimoto, and M. Ikeda, “Characterization of threading dislocations in GaN epitaxial layers”, *Appl. Phys. Lett.* 76, 3421 (2000)
- [24] M. Fleuster, C. Buchal, E. Snoeks and A. Polman, “Optical and structural properties of MeV erbium-implanted LiNbO₃”, *J. Appl. Phys.* 75, 173 (1994)
- [25] P. Capper, M. Mauk and H. J. Scheel, “Liquid phase epitaxy of electronic, optical and optoelectronic materials” (2007)
- [26] J. Jayapalan, B. J. Skromme, R. P. Vaudo, and V. M. Phanse, “Optical spectroscopy of Si-related donor and acceptor levels in Si-doped GaN grown by hydride vapor phase epitaxy”, *Appl. Phys. Lett.* 73, 1188 (1998)
- [27] H. M. Manasevit, F. M. Erdmann, and W. I. Simpson, “The use of metalorganics in the preparation of semiconductor materials IV- The nitrides of aluminium and gallium”, *J. Electrochem. Soc.* 118, 1864 (1971)
- [28] S. Yoshida, S. Misawa, and S. Gonda, “Epitaxial growth of GaN/AlN heterostructures”, *J. Vac. Sci. Technol. B.* 1 (2), 250 (1983)
- [29] S. Nakamura, “GaN growth using GaN buffer layer”, *Jpn. Appl. Phys.* 30, 10A (1991)
- [30] M. J. Wallace, P. R. Edwards, M. J. Kappers, M. A. Hopkins, F. Oehler, S. Sivaraya, R. A. Oliver, C. J. Humphreys, D. W. E. Allsopp, and R. W. Martin, “Effect of the barrier growth mode on the luminescence and conductivity micron scale uniformity of InGaN light emitting diodes” *J. Appl. Phys.* 117, 115705 (2015).

Chapter 3 – Structure and fabrication of LED devices

- [1] C. Huh, K. S. Lee, E. J. Kang, and S. J. Park, “Improved light-output and electrical performance of InGaN-Based light-emitting diode by micro-roughening of the *p*-GaN surface”, *J. Appl. Phys.*, 93 (9), 385 (2003)
- [2] J. J. Wierer, A. David, and M. M. Megens, “III-nitride photonic-crystal light-emitting diodes with high extraction efficiency”, *Nat. Photon.*, 3, 163 (2009)
- [3] X. H. Li, R. Song, Y. K. Ee, P. Kumnorkaew, J. F. Gilchrist, and N. Tansu, “Light

- extraction efficiency and radiation patterns of III-nitride light-emitting diodes with colloidal microlens arrays with various aspect ratios”, *IEEE Photon. J.*, 3 (3), 489 (2011)
- [4] Y. K. Ee, P. Kumnorkaew, R. A. Arif, H. Tong, J. F. Gilchrist, and N. Tansu, “Light extraction efficiency enhancement of InGaN quantum wells light-emitting diodes with polydimethylsiloxane concave microstructures”, *Opt. Exp.*, 17, 13747 (2009)
- [5] C. H. Chiu, C. C. Lin, H. V. Han, C. Y. Liu, Y. H. Chen, Y. P. Lan, P. Yu, H. C. Kuo, T. C. Lu, S. C. Wang, and C. Y. Chang, “High efficiency GaN-based light-emitting with embedded air voids/SiO₂ nanomasks”, *Nanotechnology*, 23, 045303 (2012)
- [6] T. H. Hsueh, J. K. Sheu, H. W. Huang, J. Y. Chu, C. C. Kao, H. C. Kuo, and S. C. Wang, “Enhancement in light output of InGaN-based microhole array light-emitting diodes” *IEEE Photon. Technol. Lett.* 17 (6), 1163 (2005)
- [7] H. M. Kim, Y. H. Cho, H. Lee, S. I. Kim, S. R. Ryu, D. Y. Kim, T. W. Kang, and K. S. Chung, “High-brightness light emitting diodes using dislocation-free Indium Gallium Nitride/Gallium Nitride multiquantum-well nanorod arrays”, *Nano Lett.* 4, 1059 (2004)
- [8] J. K. Huang, C. Y. Liu, T. P. Chen, H. W. Huang, F. I. Lai, P. T. Lee, C. H. Lin, C. Y. Chang, T. S. Kao, and H. C. Kuo, “Enhanced light extraction efficiency of GaN-based hybrid nanorods light-emitting diodes”, *IEEE J. Selec. Top. Quant. Elec.* 21 (4), 6000107 (2015)
- [9] J. Aguilar, “Ohmic *n*-contacts to gallium nitride light-emitting diodes”, 2007 REU Research Accomplishments (2007)
- [10] J.-O Song, D.-S. Leem, and T.-Y. Seong, “Formation of low resistance and transparent ohmic contacts to *p*-type GaN using Ni-Mg solid solution”, *Appl. Phys. Lett.* 83, 3513 (2003)
- [11] J. Hölz, and F. K. Schulte, “Work Functions of Metals”, in “Solid Surface Physics”, Springer-Vorlag, (1979)
- [12] J. Chen, and W. D. Brewer, “Ohmic contacts on *p*-GaN”, *Adv. Elec. Mat.* 1, 1500113, (2015)
- [13] J.-K. Ho, C.-S. Jong, C. C. Chiu, C.-N. Huang, C.-Y. Chen, K.-K. Shih, “Low-resistance ohmic contacts to *p*-type GaN” *Appl. Phys. Lett.* 74, 1275 (1999)
- [14] G. S. Marlow, M. B. Das, “The effects of contact size and non-zero metal

resistance on the determination of specific contact resistance”, Sol. Sta. Elec. 25, 91 (1982)

[15] T. Minami, “Substitution of transparent conducting oxide thin films for indium tin oxide transparent electrode applications”, Thin Solid Films, 516, 11314 (2008)

[16] M.-Y. Tsai, O. Bierwagen and J. S. Speck, “Epitaxial Sb-doped SnO₂ and Sn-doped In₂O₃ transparent conducting oxide contacts on GaN-based light emitting diodes”, Thin Solid Films, 605, 186 (2016)

[17] G.K. Reeves, “Specific contact resistance using a circular transmission line model”, Solid-State Electron. 23, 487 (1980)

[18] L. Lewis, P. P. Maaskant, and B. Corbett, “On the specific contact resistance of metal contacts to p-type GaN”, Semicond. Sci. Technol. 21, 1738 (2006)

Chapter 4 – Electro-optical methods for the characterization of GaN-based LEDs

[1] W. Shockley, “The theory of *p-n* junctions in semiconductors and *p-n* junction transistors” (1949)

[2] D. A. B. Miller, D. S Chemia, T. C. Damen, A. C. Gossard, W. Wiegmann, T. H. Wood, and C. A. Burrus, “Band-edge electroabsorption in quantum well structures: the quantum-confined Stark effect”, Phys. Rev. Lett., 53, 2173 (1984)

[3] S. M. Sze, M. K. Lee, “Semiconductor Devices: Physics and Technology” International Student Version, 3rd Edition, Wiley (2012)

[4] B. Kang, and S. B. Kim, “Temperature dependence of the component currents and internal quantum efficiency in blue light-emitting diodes”, IEEE Trans. Elec. Dev., 60 (3), 1060 (2013)

[5] D. H. Navon, “Electronic Materials and Devices”, Houghton Mifflin, (1975)

[6] K. Fujiwara, H. Jimi, and K. Kaneda, “Temperature-dependent droop of electroluminescence efficiency in blue (In,Ga)N quantum-well diodes”, Phys. Stat. Sol. (C), 6 (S2), S814 (2009)

[7] S. Chhajed, J. Cho, E. F. Schubert, J. K. Kim, D. D. Koleske, and M. H. Crawford, “Temperature-dependent light-output characteristics of GaInN light-emitting diodes with different dislocation densities”, Phys. Stat. Sol. (A), 208, 947 (2011)

- [8] C. L. Reynolds, and A. Patel, "Tunneling entity in different injection regimes of InGaN light emitting diodes", J. Appl. Phys., 103, 086102 (2008)
- [9] J. D. Wiley and G. L. Miller, "Series resistance effects in semiconductor CV profiling", IEEE Trans. On Elec. Dev. 22, 255 (1975)
- [10] S. E. Laux, and K. Hess, "Revisiting the analytic theory of p - n junction impedance: improvements guided by computer simulation leading to a new equivalent circuit", IEEE Trans. Elec. Dev. 46, 396 (1999)
- [11] L. F. Feng, Y. Li, C. Y. Zhu, H. X. Cong, and C. D. Wang, "Negative terminal capacitance of light emitting diodes at alternating current (AC) biases", IEEE J. Quant. Elec. 46, 1072 (2010)
- [12] M. A. Reshchikov, and H. Morkoc, "Luminescence properties of defects in GaN", J. Appl. Phys. 97, 061301 (2005)
- [13] Schubert, M.F., Xu, J., Dai, Q., et al.: 'On resonant optical excitation and carrier escape in GaInN/GaN quantum wells', Appl. Phys. Lett. 94, 081114 (2009)
- [14] S. Presa, P. P. Maaskant, M. J. Kappers, B. Corbett, "Fluorescence microscopy investigation of InGaN-based light-emitting diodes", IET Optoelectronics, 10, 39 (2016)
- [15] Kozłowski, G., Schulz, S., Corbett, B.: 'Polarization matching design of InGaN-based semi-polar quantum wells—A case study of (11-22) orientation', Appl. Phys. Lett., 2014, 104, 051128 (2014)

Chapter 5 – Combined electrical and resonant optical excitation characterization of multi-quantum well GaN-based light-emitting diodes

- [1] M. J. Wallace, P. R. Edwards, M. J. Kappers, M. A. Hopkins, F. Oehler, S. Sivaraya, R. A. Oliver, C. J. Humphreys, D. W. E. Allsopp, and R. W. Martin, "Effect of the barrier growth mode on the luminescence and conductivity micro scale uniformity of InGaN light emitting diodes", J. Appl. Phys. 117, 115705 (2015)
- [2] M. F. Schubert, Q. Dai, J. Xu, J. K. Kim, and E. F. Schubert, "Electroluminescence induced by photoluminescence excitation in GaInN/GaN light-emitting diodes", Appl. Phys. Lett. 95, 191105 (2009)
- [3] G. B. Lin, D. Y. Kim, Q. Shan, J. Cho, E. F. Schubert, H. Shim, C. Sone, and J. K.

- Kim, "Effect of quantum barrier thickness in the multiple-quantum-well active region of GaInN/GaN light-emitting diodes", IEEE Photonics Journal 5, 1600207 (2013)
- [4] T. E. Sale, J. Woodhead, G. J. Rees, R. Grey, J. P. R. David, A. S. Pabla, P. J. Rodriguez-Gironés, P. N. Robson, R. A. Hogg and M. S. Skolnick, "Carrier screening effects in piezoelectric strained InGaAs/GaAs quantum wells grown on the [111]B axis", J. Appl. Phys. 76, 5447 (1994)
- [5] M. Leroux, N. Grandjean, J. Massies, B. Gil, P. Lefebvre, and P. Bigenwald, "Barrier-width dependence of group-III nitrides quantum-well transition energies", Phys. Rev. B 60, 1496 (1999)
- [6] T. Akasaka, H. Gotoh, T. Saito, and T. Makimoto, "High luminescent efficiency of InGaN multiple quantum wells grown on InGaN underlying layers", Appl. Phys. Lett. 85, 3089 (2004)
- [7] M. A. Reshnikov and H. Morkoç, "Luminescence properties of defects in GaN" J. Appl. Phys. 97, 061301 (2005)
- [8] M. A. Reshchikov, D. O. Demchenko, A. Usikov, H. Helava, and Yu. Makarov, "Carbon defects as sources of the green and yellow luminescence bands in undoped GaN", Phys. Rev. B 90, 235203 (2014)
- [9] D. Zhu, J. Xu, A.N. Noemaun, J.K. Kim, E.F. Schubert, M.H. Crawford, and D.D. Koleske, "The origin of the high diode-ideality factors in GaInN/GaN multiple quantum well light-emitting diodes", Appl. Phys. Lett. 94, 081113 (2009)
- [10] M.A. der Maur, B. Galler, I. Pietzonka M. Strassburg, H. Lugauer, and A. Di Carlo, "Trap-assisted tunnelling in InGaN/GaN single-quantum-well light-emitting diodes", Appl. Phys. Lett. 105, 133504 (2014)
- [11] C. L. Reynolds Jr., and A. Patel, "Tunneling entity in different injection regimes of InGaN light emitting diodes", J. Appl. Phys. 103, 086102 (2008)
- [12] X. A. Cao, E. B. Stokes, P. M. Sandvik, S. F. LeBoeuf, J. Kretchmer, and D. Walker, " Diffusion and tunnelling currents in GaN/InGaN multiple quantum wells" IEEE Elec. Dev. Lett. 23, 535 (2002)
- [13] Z. Hu, K. Nomoto, B. Song, M. Zhu, M. Qi, M. Pan, X. Gao, V. Protasenko, D. Jena, and H. G. Xing, "Near unity ideality factor and Shockley-Read-Hall lifetime in GaN-on-GaN *p-n* diodes with avalanche breakdown", Appl. Phys. Lett. 107, 243501 (2015)

- [14] M. Binder, B. Galler, M. Furitsch, J. Off, J. Wagner, R. Zeisel, and S. Katz, "Investigations on correlation between I-V characteristics and internal quantum efficiency of blue (AlGaIn)N light-emitting diodes", *Appl. Phys. Lett.* 103, 221110 (2013)
- [15] D. S. Meyaard, J. Cho, E. F. Schubert, S. H. Han, M. H. Kim, and C. Sone, "Analysis of the temperature dependence of the forward voltage characteristics of GaInN light-emitting diodes", *Appl. Phys. Lett.* 103, 121103 (2013)
- [16] J. J. Wierer Jr., D. D. Koleske and S. R. Lee, "Influence of barrier thickness on the performance of InGaN/GaN multiple quantum well solar cells", *Appl. Phys. Lett.* 100, 111119 (2012)
- [17] J. R. Lang, N. G. Young, R. M. Farrell, Y.-R. Wu, and J. S. Speck, "Carrier escape mechanism dependence on barrier thickness and temperature in InGaN quantum well solar cells", *Appl. Phys. Lett.* 101, 181105 (2012)
- [18] H. J. Kim, G. H. Ryu, W. B. Yang, and H. Y. Ryu, "Ideality factor of GaN-based light-emitting diodes determined by the measurement of photovoltaic characteristics", *J. Kor. Phys. Soc.* 65, 1639 (2014)
- [19] H. Masui, S. Nakamura and S. P. DenBaars, "Technique to evaluate the diode ideality factor of light-emitting diodes", *Appl. Phys. Lett.* 96, 073509 (2010)
- [20] P. Kivisaari, J. Oksanen, and J. Tulkki, "Effects of lateral current injection in GaN multi-quantum well light-emitting diodes", *J. Appl. Phys.* 111, 103120 (2012)
- [21] Y. Li, C. D. Wang, L. F. Feng, C. Y. Zhu, H. X. Cong, D. Li, and G. Y. Zhang, "Elucidating negative capacitance in light-emitting diodes using an advanced semiconductor device theory", *J. Appl. Phys.* 109, 124506 (2011)
- [22] V. D. Tong, C. T. Anh, N. D. Cuong, P. H. Binh, C. T. Truong, A. T. Pham, "Frequency dependence of negative capacitance in light emitting devices", 4th International Conference on Communications and Electronics (2012)
- [23] J. Piprek, "Efficiency droop in nitride-based light-emitting diodes", *Phys. Stat. Solidi (a)*, 207 (10), 2217, (2010)
- [24] J. Cho, E. F. Schubert, and J. K. Kim, "Efficiency droop in light-emitting diodes: challenges and countermeasures", *Laser Phot. Rev.*, 7 (3), 408 (2013)
- [25] A. David, and N. F. Gardner, "Droop in III-nitrides: comparison of bulk and injection contributions", *Appl. Phys. Lett.*, 97, 193508 (2010)

- [26] T. P. Chen, C. L. Yao, C. Y. Wu, J. H. Yeh, C. W. Wang, and M. H. Hsieh, "Recent developments in high brightness LEDs." Proc. SPIE 6910, 691005 (2008)
- [27] Y. C. Shen, G. O. Mueller, S. Watanabe, N. F. Gardner, A. Munkholm, and M. R. Krames, "Auger recombination in InGaN measured by photoluminescence", Appl. Phys. Lett. 91, 141101 (2007)
- [28] M. Zhang, P. Bhattacharya, J. Singh, and J. Hinckley, "Direct measurement of Auger recombination in $\text{In}_{0.1}\text{Ga}_{0.9}\text{N}/\text{GaN}$ quantum wells and its impact on the efficiency of $\text{In}_{0.1}\text{Ga}_{0.9}\text{N}/\text{GaN}$ multiple quantum well light emitting diodes", Appl. Phys. Lett., 95, 201108 (2009)
- [29] G. Verzellesi, D. Saguatti, M. Meneghini, f. Bertazzi, M. Goano, G. Meneghesso, and E. Zanoni, "Efficiency droop in InGaN/GaN blue light-emitting diodes: Physical mechanisms and remedies", J. Appl. Phys., 114, 071101 (2013)

Appendix A: Python code for the estimation of internal quantum efficiencies

The following code was developed to perform the estimation of the internal quantum efficiency using python programming language. The code contains multiple comments so a similar one can be developed for others programming languages as for example MATLAB.

```
##### Start of the program

##### Import required python libraries
import numpy as np # package for scientific computing
import openpyxl # package to handle excel files
from scipy.optimize import curve_fit # package for fitting

##### This program uses an excel file as a source for the data, following lines
declare the file excel and workbook to be used. The name of the workbook is the
name of the sample.
sample='sample_name'
wb = openpyxl.load_workbook('samples.xlsx')
sheet_1 = wb.get_sheet_by_name(sample)

##### Declare variables
# Declare required variables using the dimensions from the excel workbook
vol = np.zeros(sheet_1.max_row-1) #Vector for voltage (V)
cur = np.zeros(len(vol)) #Vector for current (I)
curd = np.zeros(len(vol)) #Vector for current density (J)
curbyq = np.zeros(len(vol)) #Vector for I/q
lum = np.zeros(len(vol)) #Vector for light emission (L)
fitlum = np.zeros(len(vol)) #Vector for sqrt(L/hv)
EQE = np.zeros(len(vol)) #Vector for EQE
n = np.zeros(len(vol)) #Vector for carrier density (n) - optional
IQE1 = np.zeros(len(vol)) #Vector for IQE (1)
IQE2 = np.zeros(len(vol)) #Vector for IQE (2)

# Declare required constants
h=6.624e-34 # Planck's constant (m^2 kg /s)
c=3e8 # speed of light (m /s^2)
q=1.60217E-19 # electron charge (C)
LtoW=0.26278 # responsivity of the detector at selected wavelength
(A/W)
wavelength = 430e-9 # wavelength (m)
pi = 3.141592
radius = 50e-4 # contact radius (cm)
thickness = 65e-7 # thickness of the active area (cm)
Vact = pi*radius*radius*thickness

##### Define function for IQE fitting An+Bn^2+C^3
def fit_IQE(x,a,b,c):
    return a*x+b*x*x+c*x*x*x
```

```

##### Gather all the data and calculate required vectors
# Collect LIV data from the excel file
for i in range(1,sheet_1.max_row):
    vol[i-1]=sheet_1.cell(row=i+1, column=2).value #optional loop to get voltage
values
    cur[i-1]=sheet_1.cell(row=i+1, column=1).value #collect current values
    curd[i-1]=cur[i-1]/(pi*radius*radius) #calculate current density
    lum[i-1]=(sheet_1.cell(row=i+1, column=3).value)/1000 #collect light values

# Calculate required values for fitting
for i in range(0,len(vol)):
    fitlum[i]=np.sqrt((lum[i]/LtoW)/((h*c)/wavelength)) #calculate sqrt(L/hv)
    curbyq[i]=cur[i]/q #calculate I/q
    EQE[i]=(fitlum[i]*fitlum[i])/curbyq[i] #calculate EQE with LI values

#Find and print the index of the maximum of the EQE in the vector
maxEQE=np.amax(EQE)
index = EQE.argmax()
print index

##### Fitting routine
# 1. Use third order polynomial for first estimation
z = np.polyfit(fitlum, curbyq,3)
p0 = [z[2],z[1],z[0]]

# 2. Use defined expression with the first estimation calculated in previous step
popt, pcov = curve_fit(fit_IQE, fitlum[index_1:index_2], curbyq[index_1:index_2],p0)
# index_1 and index_2 have to be selected to get a range where the EQE curve
follows the ABC model to get a good fitting

# 3. Extract values, calculate maximum of the IQE and EEs
A = popt[0] #Extract value of A'
B = popt[1] #Extract value of B'
EE1 = 1/B #Calculate first extraction efficiency
C = popt[2] #Extract value of C'
maxIQE = B/(B+2*np.sqrt(A*C)) #Calculate maximum of IQE
EE2 = maxEQE/maxIQE #Calculate the second extraction efficiency

##### Optional steps
# Optional: print extraction efficiencies
print EE1
print EE2
# Previous values should be the same. This can be used to get an idea of how good
is the fitting

# Optional: use an estimation of B to find 'real' A and C constants
estB = 1e-11
estA = (A*np.sqrt(EE2*Vact*estB))/Vact
estC =
(C*np.sqrt(EE2*Vact*estB)*np.sqrt(EE2*Vact*estB)*np.sqrt(EE2*Vact*estB))/Vact

##### Calculate IQE curves
for i in range(0,len(vol)):
    IQE1[i]=EQE[i]/EE2

IQE2[i]=(B*fitlum[i]*fitlum[i])/(A*fitlum[i]+B*fitlum[i]*fitlum[i]+C*fitlum[i]*fitlum[i]*fitlum[i])

```

```

)
# optional: calculate carrier density using an estimation of B
n[i]= np.sqrt((lum[i]/LtoW)/(EE2*Vact*((h*c)/wavelength)*estB))

##### Save results in a separate excel file
wb2 = openpyxl.Workbook()
sheet = wb2.active

#Write labels in excel file
sheet.cell(row=1,column=1).value="I (A)"
sheet.cell(row=1,column=2).value="V (V)"
sheet.cell(row=1,column=3).value="L (W)"
sheet.cell(row=1,column=4).value="J (A/cm2)"
sheet.cell(row=1,column=5).value="EQE"
sheet.cell(row=1,column=6).value="IQE (using measured EQE)"
sheet.cell(row=1,column=7).value="IQE (using calculated A',B',C')"
sheet.cell(row=2,column=10).value="Extraction efficiencies"
sheet.cell(row=3,column=10).value="EE (1/B)"
sheet.cell(row=4,column=10).value="EE (EQE/IQE)"
sheet.cell(row=6,column=10).value="maximum efficiencies"
sheet.cell(row=7,column=10).value="max EQE"
sheet.cell(row=8,column=10).value="max IQE"
sheet.cell(row=10,column=10).value="Calculated values"
sheet.cell(row=11,column=10).value="A"
sheet.cell(row=12,column=10).value="B"
sheet.cell(row=13,column=10).value="C"
sheet.cell(row=15,column=10).value="Estimated values"
sheet.cell(row=16,column=10).value="A"
sheet.cell(row=17,column=10).value="B"
sheet.cell(row=18,column=10).value="C"

#Write values in excel file
sheet.cell(row=3,column=11).value=EE1
sheet.cell(row=4,column=11).value=EE2
sheet.cell(row=7,column=11).value=maxEQE
sheet.cell(row=8,column=11).value=maxIQE
sheet.cell(row=11,column=11).value=A
sheet.cell(row=12,column=11).value=B
sheet.cell(row=13,column=11).value=C
sheet.cell(row=16,column=11).value=estA
sheet.cell(row=17,column=11).value=estB
sheet.cell(row=18,column=11).value=estC

for i in range(0,len(vol)):
    sheet.cell(row=i+2, column=1).value=cur[i]
    sheet.cell(row=i+2, column=2).value=vol[i]
    sheet.cell(row=i+2, column=3).value=lum[i]
    sheet.cell(row=i+2, column=4).value=curd[i]
    sheet.cell(row=i+2, column=5).value=EQE[i]
    sheet.cell(row=i+2, column=6).value=IQE1[i]
    sheet.cell(row=i+2, column=7).value=IQE2[i]

label_save_file = 'results_IQE.xlsx'
wb2.save(label_save_file)

##### End of the program

```